MASTER THESIS

SIMULTANEOUS ACTUATION AND LOCALISATION OF BIOCOMPATIBLE UNTETHERED MAGNETIC ROBOTS INSIDE EX VIVO ARTERIAL SYSTEMS

CONFIDENTIAL

Ewout Ligtenberg

FACULTY OF ENGINEERING TECHNOLOGY
DEPARTMENT OF BIOMECHANICAL ENGINEERING

EXAMINATION COMMITTEE
dr. Islam S. M. Khalil
prof. dr. ing. Jutta Arens
dr. Giulio Dagnino

UNIVERSITY OF TWENTE.

14/03/2024

Thesis submitted by Leendert-Jan Wouter (Ewout) Ligtenberg
under the supervision of dr. Islam S. M. Khalil, prof. dr. Jutta Arens and dr. Giulio Dagnino
as part of the Master in Robotics at the University of Twente.
Defended on March 14 2024

Chapter 2 of this work has been accepted at the International Conference on Robotics and Automation (ICRA 2024): L.-J. W. Ligtenberg, N. C. A. Rabou, S. Peters, T. Vengetela, V. Schut, H. R. Liefers, M. Warlé, and I. S. M. Khalil, "Remote Control of Untethered Magnetic Robots within a Lumen using X-Ray-Guided Robotic Platform"

Chapter 3 of this work has been submitted to the International Conference on Intelligent Robots and Systems (IROS 2024): L.-J. W. Ligtenberg, M. C. J. de Boer, I. Mulder, R. Lomme, D. Wasserberg, E. A. .M. Klein Rot, D. Ben Ami, U. Sadeh, H. R. Liefers, O. Shoseyov, P. Jonkheijm, M. Warlé, and I. S. M. Khalil, "X-Ray-Guided Magnetic Fields for Wireless Control of Untethered Magnetic Robots in Cerebral Vascular Phantoms"

Chapter 4 of this work has been accepted in principle by Nature Communications Engineering: L.-J. W. Ligtenberg, N. C. A. Rabou, C. Goulas, W. C. Duinmeijer, F. R. Halfwerk, J. Arens, R. Lomme, V. Magdanz, A. Klingner, E. A. M. Klein Rot, C. H. E. Nijland, D. Wasserberg, H. R. Liefers, P. Jonkheijm, A. Susarrey-Arce, M. Warlé, and I. S. M. Khalil, "*Ex Vivo* Validation of Magnetically Actuated Intravascular Untethered Robots in a Clinical Setting"

Chapter 5 of this work has been submitted to the International Conference on Biomedical Robotics and Biomechatronics (BioRob 2024): L.-J. W. Ligtenberg, L. de Jongh, H. R. Liefers, D. Wasserberg, E. A. M. Klein Rot, D. Ben Ami, U. Sadeh, R. Lomme, G. G. M. Tuijthof, O. Shoseyov, P. Jonkheijm, M. Warlé, and I. S. M. Khalil, "X-Ray-Guided Robotic Platform for Remote Control of Untethered Magnetic Robots Targeting Blood Clots in the Iliac Artery"

Chapter 6 of this work is planned to be submitted to Applied Physics Letters: L.-J. W. Ligtenberg, L. Hafferl, L. de Jongh, A. Paul, C. Goulas, S. Mohanty, and I. S. M. Khalil, "Non-Buoyant Microrobots Swimming with Near-Zero Angle of Attack"

Chapter 7 of this work has been submitted to the International Conference on Biomedical Robotics and Biomechatronics (BioRob 2024): J. K. van der Mijle Meijer, I. Mulder, L.-J. W. Ligtenberg, H. R. Liefers, V. Magdanz, I. S. M. Khalil, "Controlled Locomotion of IRON-Sperm Clusters: Evaluating Maneuverability with X-Ray-Guided Magnetic Fields"

Chapter 8 of this work is part of a study that is planned to be submitted to Nature Communications Engineering: V. Magdanz, Y. Pervez, M. LaBrash-White, L.-J. W. Ligtenberg, I. Mulder, J. K. van der Mijle Meijer, S. Mohsenkani, M. Gorbet, N. Bouzari, H. Shahsavan, L. Weber, H. R. Liefers, M. Warlé, and I. S. M. Khalil, "Sperm Cell Empowerment: X-Ray-Guided Magnetic Fields for Enhanced Actuation and Localization of Cytocompatible Biohybrid Microrobots"

Abstract

Recent advancements in minimally invasive medicine have spurred a growing focus on non-invasive techniques, highlighting limitations inherent to catheter-based interventions such as size and flexibility. To address these limitations, untethered magnetic robots (UMRs), propelled by magnetic torque and field gradients, for navigating fluid-filled lumens like blood vessels, offer potential as treatment modalities or drug carriers. However, to realize *in vivo* applications significant challenges need to be overcome, including imaging for control and performance assessment, robust actuation methods capable of withstanding physiological environments, and ensuring biocompatibility. In this study, we present an X-ray-guided teleoperation system suitable for visualizing hemocompatible UMRs, specifically screw-type variants with affixed permanent magnets, scalable for *in vivo* applications. Actuation of these UMRs is achieved via a magnetic torque generated using a single rotating permanent magnet (RPM), enabling effective propulsion against blood flow up to 67 mL/min and facilitating a grinding action for thrombus reduction, measuring 3.6 mm^3 reduction in 30 minutes. The designed teleoperated control scheme enhances the success rate from 56% to 76% during *in vitro* experiments, which is further validated in *ex vivo* settings navigating from abdominal to renal arteries. Furthermore, we introduce a gravity compensation method utilizing the RPM's magnetic force, enabling precise three-dimensional motion control exemplified in an *in vitro* carotid artery model, yielding a success rate of 89%, in navigating between the common carotid artery and into the distal end of the internal carotid artery. This compensation method is extended to support microscale soft-magnetic UMRs, demonstrating swimming with near-zero angle of attack of $0.8^\circ \pm 0.6^\circ$. Additionally, we demonstrate the adaptability of our system, by applying it to rolling motion biohybrid UMRs, which are navigated successfully through X-ray-guided magnetic fields into both the fallopian tubes of an *in vitro* human reproductive tract model and into each branch of a trifurcation model. These advancements mark significant progress towards the use of UMRs for *in vivo* trials, showcasing the potential of UMRs in revolutionizing minimally invasive medical interventions.

Contents

1 Introduction

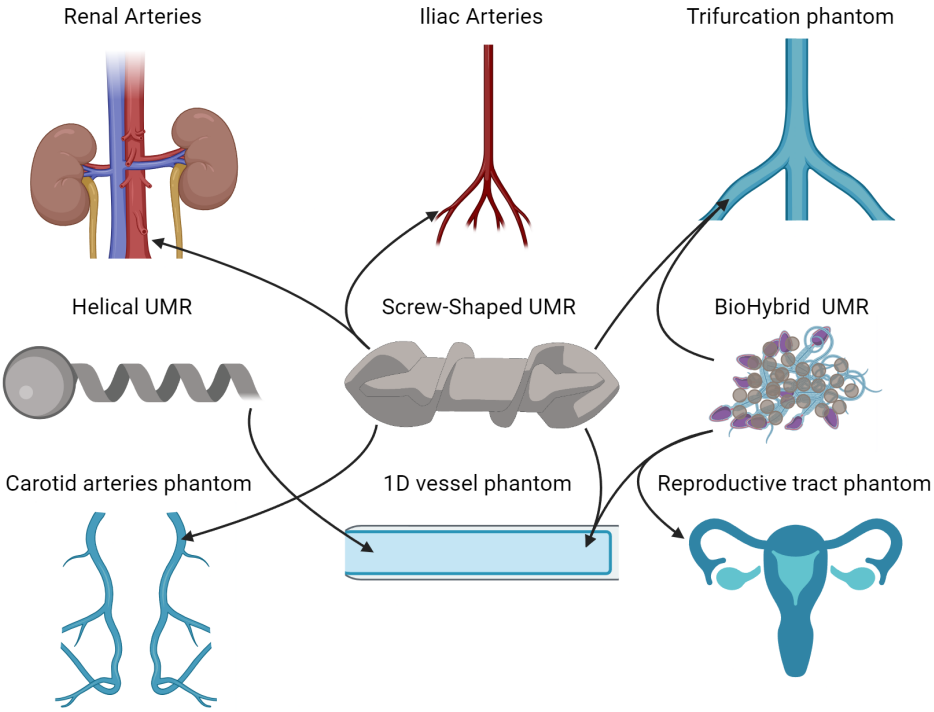

Fig. 1: *Illustration of the different types of untethered magnetic robots (UMRs) used in this study; the arrows indicate in which model each UMR type has been actuated and controlled.*

In recent years, untethered magnetic robots (UMRs) have emerged as promising tools for surgical and medical applications, with notable potential in drug delivery, material removal, and targeted therapy. Most commonly, UMRs feature a chiral structure (e.g., screw-shaped or helical body) crafted from or containing magnetic materials, exploiting an external rotating magnetic field for propulsion. Alternatively, some UMR designs facilitate rolling motion along surfaces, often employing spherical geometries, although other configurations have been explored, as illustrated in Fig. 1. These robots navigate through bodily fluids and soft tissue, such as the intricate network of blood vessels [1] or the complex pathways of the nervous system [2], to reach their intended targets. Despite significant advancements in UMR technology through *in vitro* experimentation, where critical physical interactions are investigated, the translation of these innovations into real-world applications remains a challenge. Recent breakthroughs in the field of UMRs, including the development of biocompatible robots [3], imaging techniques [4], manipulation setups [5], and control methodologies [6], have propelled our understanding and showcased the potential of these robotic systems. However, it is important to acknowledge that while *in vitro* studies provide valuable insights, they do not fully capture the complexity of living organisms. Moreover, transitioning from *in vitro* experimentation to *in vivo* applications necessitates confronting the challenges associated with operating within larger, more dynamic environment. Consequently, the possibilities afforded by UMRs in clinical settings remains unknown.

Prior to translating UMRs into *in vivo* experimentation, it is important to address several key challenges, including ensuring biocompatibility, robust three-dimensional (3D) motion control of UMRs, sufficient UMR actuation strength, and precise localization of both the UMR and its target. Consider a scenario where a UMR is tasked with navigating within the human body to reach a thrombus within the intricate network of blood vessels, as depicted in Fig. 2. Once the thrombus is successfully degraded, the UMR must navigate back to its point of insertion for

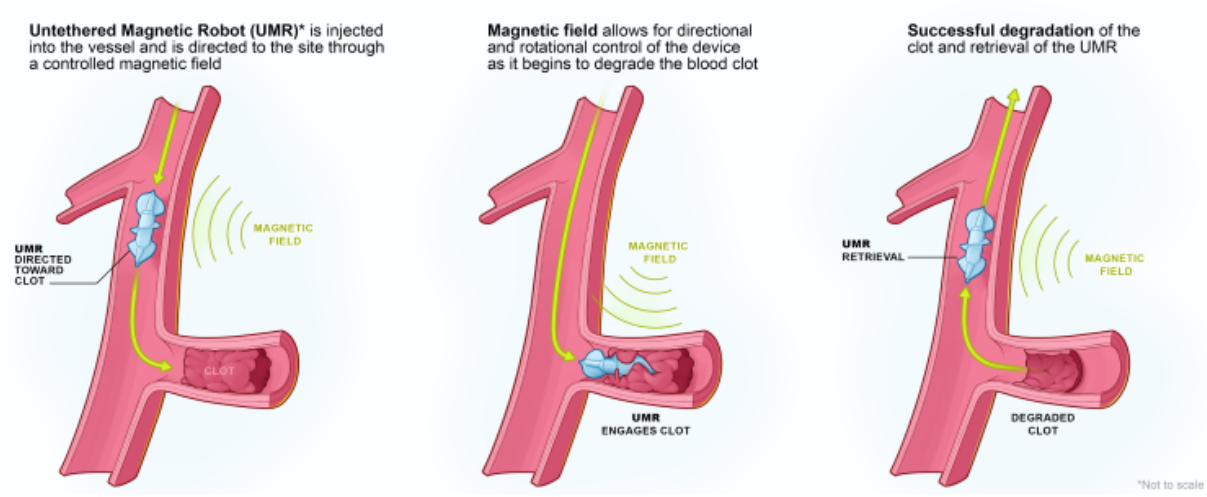

Fig. 2: *Schematic representation of an untethered mangetic robot being guided towards a thrombus, interacting with the thrombus and showing successful degradation of the thrombus.*

retrieval. During this entire process, the UMR is exposed to blood for an extended duration, underscoring the critical necessity for hemocompatibility. Moreover, the UMR must possess the capability to navigate precisely through the correct vessels to reach its target, and in the depicted scenario, during the UMR's return to its initial insertion point it encounters significant blood flow, necessitating robust propulsive thrust. Additionally, localization methods are indispensable for monitoring the vessel network, UMR position and orientation, and the target site to facilitate effective control over the UMR.

The most common method of controlling UMRs involves the application of rotating magnetic fields, which induce magnetic torque on the UMR, resulting in UMR propulsion. Mahoney *et al.* demonstrated the use of a rotating magnetic field to roll a spherical UMR towards its target [7], while Abbot *et al.* achieved helical propulsion by employing a rotating magnetic field to rotate a helical body [8]. Despite these advancements, a significant portion of research relies on electromagnetic coils for control, presenting challenges in scalability to human dimensions. In response, Fountain *et al.* proposed an innovative approach utilizing a rotating permanent magnet (RPM) for UMR modeling and actuation [2]. Building upon this work, Ligtenberg *et al.* expanded the scope by demonstrating open-loop bounded responses for this actuation method [9]. Moreover, they showcased the RPM's ability to counteract gravitational forces experienced by the UMR, enabling a near-zero angle of attack during UMR swimming motion [10]. However, it is crucial to note that these advancements primarily rely on open-loop control with simple or undefined trajectories.

Precise localization is crucial in the development of closed-loop systems for UMRs. Niedert *et al.* demonstrated the feasibility of utilizing ultrasound imaging to visualize a tumbling drug-loaded UMR within a live mouse's colon, highlighting the potential for this non-invasive imaging method [11]. However, ultrasound imaging is limited in terms of field-of-view and ease of use, restricting its application primarily to smaller animals. In contrast, Vonthrom *et al.* employed magnetic resonance imaging (MRI) systems for UMR localization and control, utilizing the magnetic field gradients to enable simultaneous actuation and localization [12]. While MRI offers advantages in imaging larger anatomical structures, it poses challenges for torque-driven UMRs due to its limited compatibility with magnetic actuation methods. Tiryaki *et al.* expanded UMR control capabilities with MRI by integrating high-intensity focused ultrasound for controlled drug release [13]. However, it is important to note that MRI scanners may not be optimal for torque-driven UMRs due to potential interference from the strong magnetic fields generated with MRI.

To address the challenge of magnetic field interference with wireless actuation during imag-

ing procedures, Bakenecker *et al.* developed a localization method utilizing a magnetic particle imaging (MPI) scanner, facilitating untethered aneurysm coiling without the need for iodine-based contrast agents or ionizing radiation [14]. By coating the UMR with magnetic particles, the MPI scanner can precisely locate the UMR. However, MPI's inherent limitations lie in its inability to provide environmental visualization, as it is primarily designed to detect the distribution of superparamagnetic iron-oxide nanoparticles. As an alternative approach, Huaroto *et al.* employed optical visualization methods, utilizing two-photon microscopy to observe UMRs beneath fixed tissue [15]. Nevertheless, this technique is constrained by its limited penetration depth. To overcome these challenges, X-ray imaging offers a promising solution for visualizing both the vessel network and UMR location simultaneously [16]. Moreover, X-ray scanners equipped with cone-beam computed tomography (CBCT) or 3D rotational angiography capabilities can generate comprehensive 3D reconstructions of the vessel network, enabling 3D path planning and 2D localisation with a large field of view, with a single imaging tool. Kim *et al.* leveraged this non-invasive imaging method to develop a teleoperated robotic system for magnetic manipulation of a guidewire, facilitating navigation within an *in vivo* porcine brachial artery [17]. Such a teleoperated setup mitigates the need for precise *in vivo modeling*, offering advantages in clinical scenarios.

The performance of the UMR control system can be validated by conducting *ex vivo* trials, which combines hurdles such as; inconsistent vessel diameter, unknown UMR environment, and also adds the simulation of blood flow. To address the risk of UMR loss within bodily fluids, Son *et al.* devised a magnetic field trap capable of guiding a UMR through the intricate network of blood vessels [18]. Validation of this actuation method on rat brain tissue, coupled with X-ray feedback, demonstrated promising prospects for employing UMRs in challenging-to-control areas. In contrast, Yang *et al.* designed a different actuation strategy, leveraging frictional forces between the blood vessel walls and the UMR [19]. Successfully navigating the rabbit aorta at high flow speeds, this approach relies heavily on the magnetic attraction forces of their actuator; insufficient attraction may result in UMR control loss. To mitigate this risk, Wang *et al.* engineered a stent-like UMR designed to self-lock in the absence of actuation, ensuring UMR stability within the vessel [20]. Validated in porcine arteries under high-flow conditions, this design underscores the potential of UMRs in scenarios demanding robust control mechanisms. While these *ex vivo* trials demonstrate the promise of UMRs for drug delivery applications, they may not be optimal for material removal of large obstructions. Consequently, there is a need to extend such trials to include screw-shaped UMRs, which can capitalize their unique propulsion mechanisms for effective material removal, as illustrated in Fig. 2.

In this study, we design screw-shaped milliscale UMRs and introduce a control framework, suitable for *in vivo* applications. First, we extend the setup as described by Ligtenberg *et al.* [9, 10], to support complex 2D trajectories. After investigating the feasibility of localizing milliscale UMRs and their environment using a CBCT scanner and we introduce a teleoperation strategy, where the operator stays in the loop to directly control the speed of the UMR, as described in Chapter 2. With this teleoperated control method the UMR's turning position for entry of a side branch can be controlled, resulting in a measurable increase of successful entry and exit of the targeted side branches. Secondly, we advance our approach to design a 3D motion control system, leveraging magnetic torque for yaw adjustments and exploiting magnetic field gradient pulling for vertical movement, as described in Chapter 3. Here we show that the combination of both these actuation methods using a single RPM allows us to counteract gravity and successfully navigate into each branch of a 3D carotid artery phantom. Third, we validate the designed control system in an *ex vivo* porcine abdominal aorta model, as discussed in Chapter 4. Here we investigate UMR performance parameters including hemocompatibility, frequency response, and blood flow response. Furthermore, we demonstrated the control of such screw-shaped UMR in *ex vivo* tissue in a clinical setting. Targeting the left renal artery (LRA) of a porcine aorta

model, we enter and exit the LRA all while continuously being exposed to blood flow. Fourth, we expand this control method in Chapter 5, where we target a branch with an obstruction. Once at the obstruction, the UMR executes a grinding action, slowly degrading the thrombus. Using CBCT reconstructions we determine the mechanical thrombus removal rate of a UMR. We find an average decrease of 16% after 0.5 hour of drilling, while the control measurement showed no measurable decrease in size. Lastly, we explore the applicability of our control method across different UMR designs, as depicted in Figure 1, and evaluate their performance. Specifically, we investigate the control of microscale helical UMRs, characterized by their ferromagnetic properties, and biohybrid UMRs capable of rolling motion, shedding light on the adaptability and versatility of our approach across various UMR configurations.

Microscale helical untethered magnetic robots

To expand the use of UMRs to operate in even smaller environments, microscale UMRs have shown great promise. Typically composed of a single coated structure or crafted from magnetic materials [3, 21, 22], microscale UMRs are predominantly ferromagnetic due to their small size. Consequently, actuation of such UMRs becomes a greater challenge [5]. Drawing inspiration from natural biological structures, many microscale UMRs feature helical bodies or flagella-like configurations to achieve propulsion. For instance, Jeon *et al.* employed such UMRs to navigate deep inside the blood vessel system of a rat brain for stem cell delivery, demonstrating the potential of microscale UMRs [23]. Most of the previous research regarding microscale UMRs use electromagnetic coils for their actuation and control, limiting their workspace. Addressing this constraint, Yang *et al.* introduced a mobile coil system to broaden the operational range [24]. However, this solution necessitates a complex setup. In Chapter 6, we explore an alternative approach by investigating the feasibility of employing a single RPM for controllable navigation of microscale helical UMRs. Leveraging on magnetic force gradient pulling to counteract gravitational forces and magnetic torques for propulsion, we adapt the gravity compensation model proposed by Ligtenberg *et al.* [10] to support ferromagnetic materials and apply it to microscale UMRs. Our findings suggest promising actuation direction for enhancing the adaptability and maneuverability of microscale UMRs, increasing their potential for integration into biomedical applications.

Biohybrid untethered magnetic robots

To evaluate the performance of the designed control system on ferromagnetic UMRs, we explore the feasibility of controlling biohybrid UMRs. Typically comprised of magnetically or drug-loaded cells, biohybrid UMRs commonly utilize cell types such as *E. coli*, sperm cells, and magnetotactic bacteria (MTB) [25]. Magdanz *et al.* demonstrated the controllable actuation of a single biohybrid UMR, called IRONSperm, employing a magnetically loaded sperm cell [26]. Furthermore, they showed collective actuation of these sperm cells in clusters, enabling rolling motion within confinements detectable via ultrasound imaging. In Chapter 7, we investigate the feasibility of using X-ray fluoroscopy images to visualise the IRONSperm clusters, alongside pioneering 2D control experiments conducted within a trifurcation phantom, both horizontally and vertically. Additionally, illustrate the possible clinical applications of using such IRONSperm clusters, we show in Chapter 8 that we are able to control them in 3D inside a physiologically accurate reproductive tract phantom, using X-ray fluoroscopy for imaging. In this work we also investigate other key parameters important for *ex vivo* use. We find low cytotoxicity and adequate detectability of IRONSperm clusters through both ultrasound and X-ray fluoroscopy imaging modalities. These findings lay a foundation for exploring clinical possibilities and advancing the utility of biohybrid UMRs in biomedical applications.

2 Remote Control of Untethered Magnetic Robots within a Lumen using X-Ray-Guided Robotic Platform

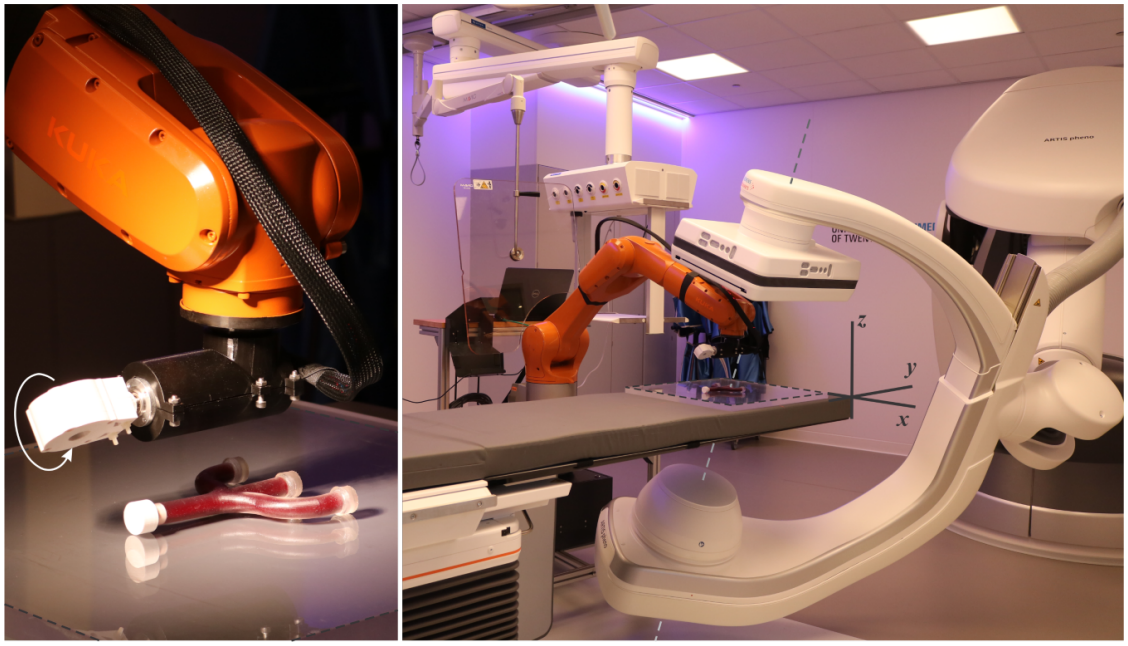

Fig. 3: *The robotic platform consists of two key components: a robotic C-ARM imaging system and a wireless manipulation system. These components work in tandem to achieve precise localization and wireless actuation. The untethered magnetic robot is contained within a fluid-filled lumen and guided using rotating magnetic fields.*

Achieving efficient manipulation of UMRs within bodily fluids and tissues has been successfully accomplished by utilizing external stimuli, primarily magnetic fields [1, 2]. These external stimuli provide the essential power required for locomotion and precise directional control over a distance, thus enabling innovative diagnostic and therapeutic procedures that were previously unattainable. As more locations within the human body become accessible, this approach unlocks unprecedented possibilities. However, navigating controllably within these natural pathways demands feedback control to guide the UMR along the intended trajectory.

Implementing this feedback control through teleoperation offers convenience by giving clinicians complete control over the UMR during potential interventions, and this requirement is driven by two fundamental reasons. First, accurately modeling the motion dynamics of the UMR for calculating model-based control inputs (physical-model-based approach) might prove challenging. Second, it is inherently safer for the user to conduct the intervention without decreasing the clinician's authority over control. Satisfying this requirement mandates the integration of an imaging system and a wireless manipulation system. These components empower clinicians to base their inputs on real-time medical images, delivering comprehensive insights into the UMR's position and orientation, physical surroundings, and intended path [3]. This integration has facilitated the implementation of wireless actuation and motion control experiments under conditions similar to those encountered *in vivo*, or even the achievement of wireless control directly within *in vivo* environments [4, 5]. In these methods, opting for teleoperation of the UMR without the need for a physical model might offers greater advantage. By coupling the UMR with external stimuli through a teleoperation system, operators can effectively guide its movement along the intended trajectory. In this case, the physical model of the UMR would be used offline to create a useful mapping between its inputs and motion dynamics. Once equipped with this mapping, the control inputs can be predicted based on the physical conditions of the surroundings and the UMR (e.g., vessel diameter, blood flow, viscosity, and step-out).

In this chapter, we develop an interventional X-ray-guided robotic platform for the direct teleoperation of UMRs (screw-type, Fig. 1). The control inputs, including actuation frequency, field strength, and the rotation axis of the rotating field, are determined based on the intended trajectory and anticipated response of the UMR. These inputs serve as the foundation for a 2-degree-of-freedom (DOF) control system. This system operates by calculating the joint-space coordinates of the wireless manipulation system from X-ray Fluoroscopy images of the environment collected offline. Then, we dynamically modulate the swimming speed of the UMR by adjusting the actuation frequency via teleoperation, which is guided by real-time positional data visualized through X-ray Fluoroscopy images. This process ensures precise alignment between the actuator magnet and the UMR. The rest of this chapter is structured as follows: Section 2.1 offers insights into the robotic platform (Fig. 3) and technical integration details of its core components, namely the C-Arm imaging system and wireless manipulation system. Our teleoperation control strategy is outlined in Section 2.2, where we focus on the motion dynamics of the UMR within a confinement and the development of a 2-DOF control configuration. The validation of our teleoperation strategy and robotic platform is presented in Section 2.3, using scenarios involving curved and bifurcated fluid-filled lumens. Finally, Section 2.4 provides conclusions and outlines directions for future research.

2.1 Interventional X-ray-guided robotic platform

The X-Ray-Guided robotic platform is illustrated in Fig. 3. The X-ray source and detector (Siemens Healthineers Artis Pheno, Erlangen, Germany) possess three rotational degrees of freedom and one translational DOF. While these three degrees of freedom would enable us to reconstruct any environment, we constrain the configuration to achieve real-time feedback essential for teleoperation at appropriate frame rates. The X-ray source-detector axis (dashed gray line) is fixed at an angle of 20° relative to the $\boldsymbol{z}$-axis (in the frame of reference in Fig. 3). This configuration enables us to reconstruct the environment of any curved or bifurcated lumen, and the translational DOF can be utilized to minimize geometric blur. Acceptable signal-to-noise ratio is obtained using clinical radiation level with a fluoroscopy dose rate of 0.13 $\mathrm{mGy.cm^2 s^{-1}}$, as shown in Fig. 4. Additionally, with this oblique configuration, we create a relatively large workspace, granting the end-effector of a robotic manipulator greater access over the lumen.

The robotic manipulator (KUKA KR-10 1100-2, KUKA, Augsburg, Germany) is employed to control the positioning of a RPM actuator [6], generating a magnetic field of about 5 mT at a gap of 7 cm that undergoes rotation within the operational area of the lumen. With 6-DOF, the robotic manipulator adeptly manages the RPM's rotation axis, thereby achieving precise control over the magnetic field's orientation exactly at the UMR's location within the lumen. When considering a UMR endowed with a magnetic moment perpendicular to its longitudinal axis, introducing a rotating magnetic field revolving around the $\boldsymbol{y}$-axis enables propulsion along the lumen, as demonstrated in Fig. 4. To accomplish forward and backward straight movements within the lumen, the robotic manipulation of the RPM's rotation axis aligned with the $\boldsymbol{y}$-axis is essential. Moreover, if desired, the manipulation of the RPM's rotation axis about the $\boldsymbol{z}$-axis facilitates the exertion of in-plane torque to steer the UMR. Similarly, the RPM's rotation axis can be controlled about the $\boldsymbol{x}$-axis to steer the UMR out-of-plane with a non-zero pitch angle.

The operator has the capability to manipulate the RPM-actuator's position from a protected area behind a radiation shield during experimental sessions. The C-Arm's oblique setup delivers real-time X-ray Fluoroscopy images encompassing the RPM-actuator, the UMRs, and the contours of the curved lumen. As depicted in Fig. 4, the radiopaque objects stand out distinctly, facilitating the straightforward identification of both the RPM's and UMR's rotation axes. The RPM is composed of a cylindrical permanent magnet (with magnetic moment $\mathbf{M}$) rigidly affixed to a DC motor. Notably, the magnetic moment of this permanent magnet aligns perpendicularly to the rotation axis $\boldsymbol{\Omega}_{\mathrm{act}}$. This orientation allows for the alignment of the RPM's rotation axis with the curved lumen's centerline based on the X-ray Fluoroscopy images. Similarly, the UMR

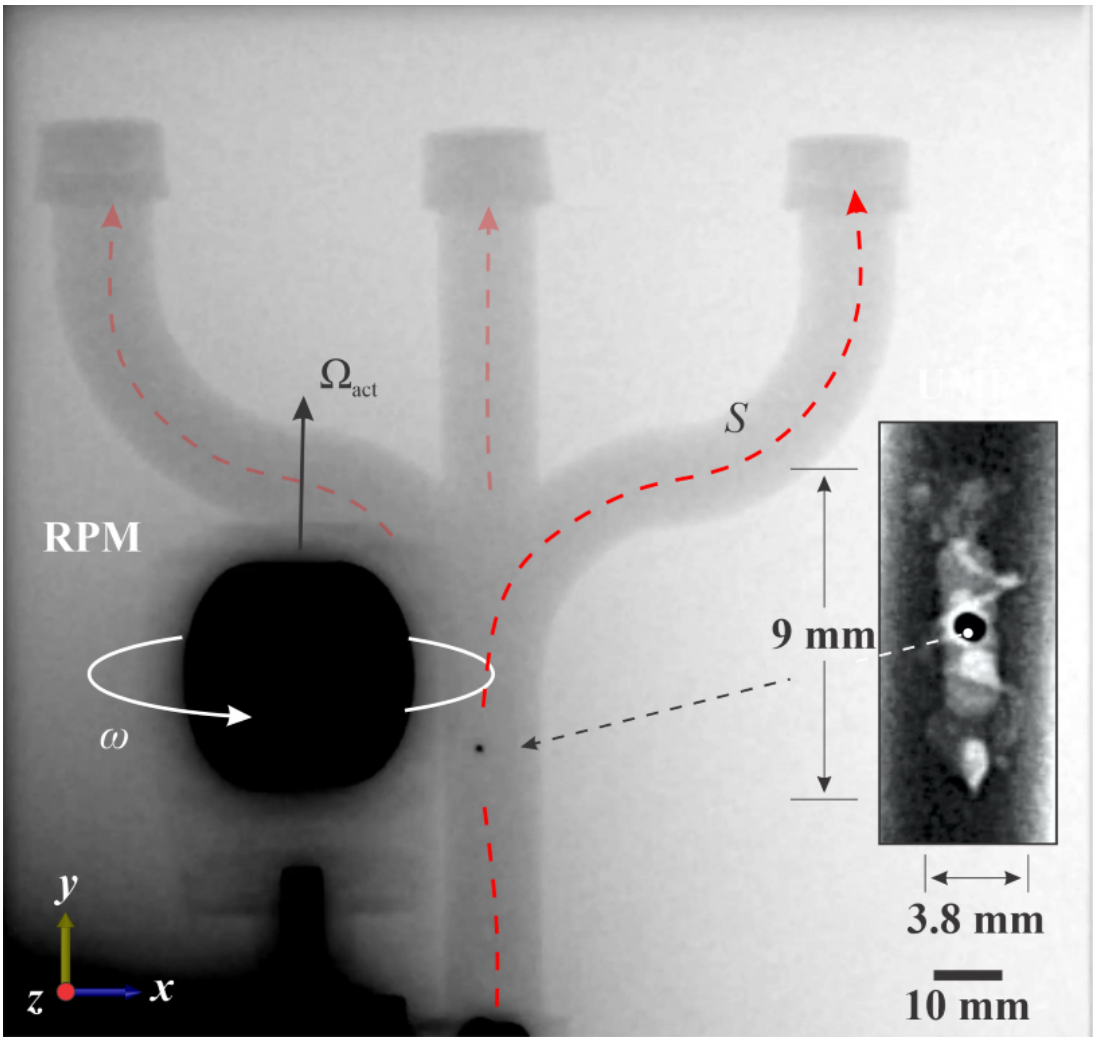

Fig. 4: *An X-ray Fluoroscopy image captures a untethered magnetic robot (UMR) navigating within a curved lumen. The curvature of the lumen is defined by the tangent angle ($\psi(S)$) relative to the arc length S. The UMR's movement involves a dual action: rotation of the rotating permanent magnet (RPM) around the rotation axis $\mathbf{\Omega}_{\text{act}}$ and controlled steering facilitated by in-plane torque applied about the $\boldsymbol{z}$-axis. The inset shows the UMR visualized through the utilization of a radiocontrast agent.*

features a non-magnetic screw-shaped body housing a 1 mm cylindrical permanent magnet. This magnet intercepts radiation, precluding the passage of X-rays. Consequently, it is feasible to determine the position of the permanent magnet while the UMR's geometric details remain undisclosed through X-ray imaging.

2.2 Teleoperation control strategy

Our UMR is a screw-type, featuring a non-magnetic screw-shaped body complemented by a rigidly attached permanent magnet. This configuration incorporates a helical wave pattern onto a cylinder. The magnet enables versatile motion capabilities, including rotation along the longitudinal axis for propulsion, as well as in-plane and out-of-plane rotations essential for executing yawing and pitching maneuvers, respectively. This level of control is accomplished by a rotating magnetic field generated by position-controlled RPM-actuator. This control system is composed of two parts: The first involves a predictive feedforward control input, $\mathcal{F}$. Computed based on the contours of the surrounding blood vessels, regardless of their diverse morphologies, this input enables the UMR to autonomously adjust its orientation to the ever-changing vessel geometries. The second is the X-Ray-Guided control input $\mathcal{C}$, an operator intervention. This

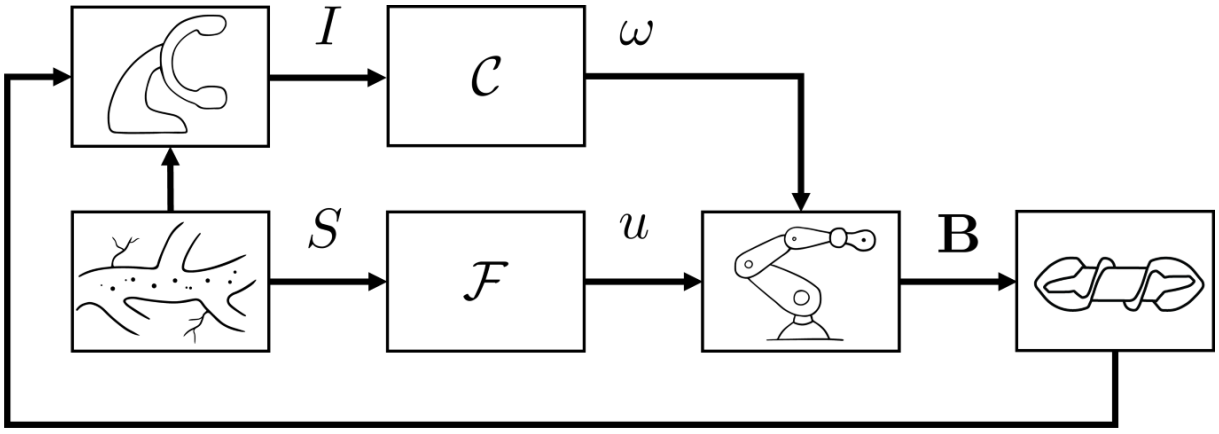

Fig. 5: *The 2-degree-of-freedom control configuration for an untethered magnetic robot (UMR) within a vascular model utilizes predefined confinement geometry and real-time UMR positioning through X-ray imaging. The control system $\mathcal{F}$ determines the joint-space coordinates u of the robotic manipulators over time based on the centerline of the curved lumen and expected UMR translational velocity, while the control system $\mathcal{C}$ is calculated based on the position of the UMR with respect to the rotating permanent magnet.*

input takes into account the hard-to-model dynamics, giving the operator real-time control rooted in X-ray feedback, I. Combining these two inputs allows for the simultaneous control of the RPM's rotation axis and its rotational speed, ω. This integration is what generates the targeted rotating magnetic field, $\mathbf{B}$, and the intended torque on the UMR (Fig. 5).

2.2.1 Predictive feedforward control input $\mathcal{F}$

Considering a curved lumen with an arbitrary shape, it is possible to approximate any small segment of its boundary using a continuous curve function. Once this continuous function is derived from the known digital points within the field of view (Fig. 4), we can accurately ascertain both the tangent angle and curvature at any point of interest along the curve. If the curve is described by the parametric equation $\{x(S), y(S)\}$, where S is the arc length, then the slope of the tangent line, $m(S)$, at any point is given by

$$m(S) = \frac{\mathrm{d}y/\mathrm{d}S}{\mathrm{d}x/\mathrm{d}S}, \quad \text{and} \quad \psi(S) = \tan^{-1} m(S), \tag{1}$$

where $\psi(S)$ represents the tangent angle at a specific point. Through the derivative of $\psi(S)$ with respect to the arc length, we acquire the instantaneous rate of change, curvature. This curvature can be expressed as follows:

$$\mathcal{K}(S) = \frac{\mathrm{d}\psi(S)}{\mathrm{d}S}. \tag{2}$$

Utilizing the local tangent, we can determine the intended rotation axis of the RPM, $\mathbf{\Omega}_{\text{act}}$. Concurrently, the curvature will provide insight into the geometric attributes at the designated point of interest. If the rotation axis and position of the RPM are constrained in a manner where the field rotation axis in the vicinity of the UMR aligns parallel to the local tangent, it becomes feasible to calculate the desired joint-space variables of the 6-DOF robotic manipulator.

The configuration-to-pose kinematics of the robotic manipulator, denoted as $\{\mathbf{p}_{\text{act}}, \mathbf{R}\} = \mathcal{L}(\boldsymbol{q})$, enables precise control over the RPM-actuator's pose. Therefore, for a given desired field rotation axis we can determine the joint-space coordinates, $\boldsymbol{q}$ using the position of the UMR within the curved lumen. We use the following velocity-level kinematics to compute the

joint-space variables [6]:

$$\begin{pmatrix} \dot{\mathbf{p}}_{\text{act}} \\ \dot{\mathbb{M}} \end{pmatrix} = \begin{pmatrix} \mathbb{I} & 0 \\ 0 & \text{SK}(\mathbb{M})^{\text{T}} \end{pmatrix} \mathbf{J}_{\text{m}}(\boldsymbol{q})\dot{\boldsymbol{q}} = \mathbf{J}_{\text{A}}(\boldsymbol{q})\dot{\boldsymbol{q}}, \tag{3}$$

where $\text{SK}(\cdot)$ is the skew-symmetric operator of the cross product, $\mathbf{J}_{\text{m}}$ is the geometric Jacobian, and $\mathbf{J}_{\text{A}}$ is the RPM-actuator Jacobian. Taking into account the swimming speed of the UMR and the gradient of the tangent line at the UMR's location, Equation (3) can be applied to compute the joint-space variables, $\boldsymbol{q}$.

2.2.2 X-ray-guided control input $\mathcal{C}$

The open-loop nature of control system, $\mathcal{F}$, depends on the UMR's ability to maintain the magnetic coupling with the RPM by moving along at the same speed. In real-world scenarios, the swimming speed of the UMR will be influenced by various factors, including the wall effect, blood flow dynamics, and other hard-to-model behaviors. Therefore, feedback control, $\mathcal{C}$, is provided by the operator to compensate for any undesirable response during actuation.

Our feedback control is constrained to modifying the swimming speed solely by manipulating the actuation frequency of the RPM. For instance, if the UMR's movement deviates from the RPM actuator's predictions according to physical-models, the operator can directly fine-tune the actuation frequency to uphold the intended magnetic coupling. This adjustment is performed directly using the collected X-ray Fluoroscopy images. The speed of the UMR scales linearly with the actuation frequency for a given fluid and geometry. This linear correlation remains valid below a step-out frequency, determined by the magnetic and drag torque applied to the UMR. Note that the control law $\mathcal{F}$ is fully capable of maneuvering the UMR within any curved lumen. Nevertheless, the feedback input, $\mathcal{C}$, provided by the operator is expected to enhance control accuracy by improving the magnetic coupling between the UMR and the RPM actuator, and by controlling the UMR's swimming speed at the bifurcation. This hypothesis could be confirmed through a comparative experimental study, assessing the success rate of UMR movement within blood-filled curved lumens.

2.3 Experimental validation

2.3.1 Experimental setup

We conduct motion control experiments with the UMR inside a 3D-printed vessel phantom. The UMR has a length of 9 mm and outer diameter 3.8 mm with an affixed NdBFe Grade-N45 permanent magnet, 1 mm in diameter and height. The resulting step-out frequency of such UMR in blood is 28 Hz with a velocity of 34 mm/s, the UMR is coated with LipoCoat 4AC coating technology to ensure hemocompatibility. The phantom exhibits a pitchfork configuration, facilitating the evaluation of control characteristics within three distinct pathways. Each pathway has an inner diameter of 9.5 mm. The phantom is filled with heparinized porcine blood, and the long axis of the straight pathway aligns with the $\boldsymbol{y}$-axis in the frame of reference illustrated in Fig. 3. In each control trial, the UMR is precisely controlled, with an actuation frequency of 9 Hz, to swim from the proximal end of the phantom to the distal end of one of the pathways and then return. The success of each trial is determined by the control system's ability to maneuver the UMR controllably along the intended pathway and bring it back to the starting point. The mean absolute position error (MAE) is determined in each trial by assessing the deviation of the UMR from the centerline of the intended pathway. Two control configurations are evaluated: the first utilizes the predictive feedforward input $\mathcal{F}$, while the second is the 2-DOF control configuration $\mathcal{F} + \mathcal{C}$. In control system $\mathcal{F}$, both the UMR and the wireless manipulation system operate autonomously, with no direct operator involvement. In control system $\mathcal{F} + \mathcal{C}$, the operator offers limited corrections to the swimming speed, while the motion of the robotic arm is automatically determined based on the configuration of each pathway.

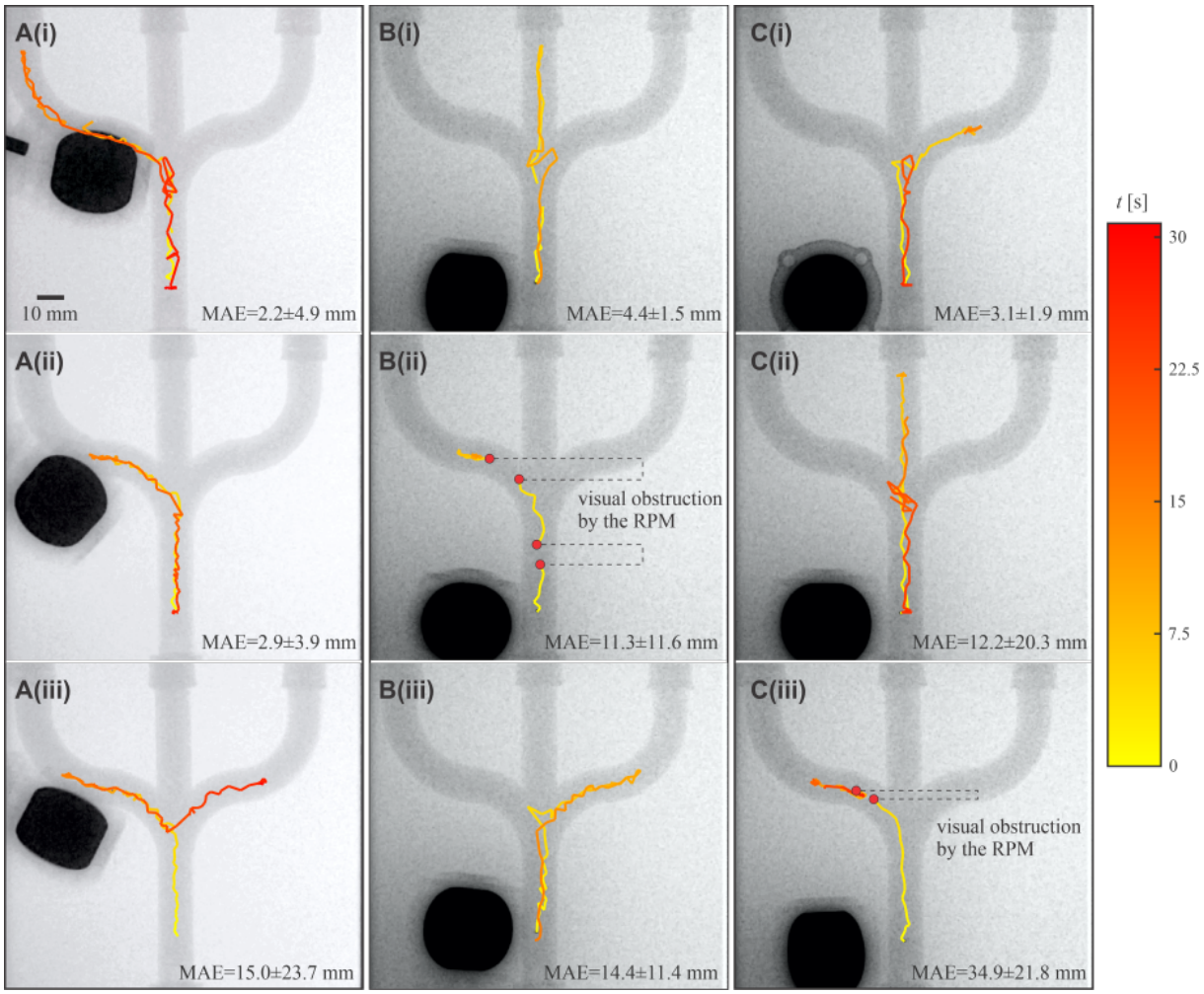

Fig. 6: *Control of the untethered magnetic robot (UMR) is implemented through the control system $\mathcal{F}$, which relies on the geometry of the desired path and the UMR speed. The success rate is assessed by conducting 10 trials along the left, straight, and right lumens. The UMR is controlled to move forward toward the distal end of any of the paths and subsequently return to the starting point. The mean absolute position error (MAE) is calculated using 10 trials. (A) The UMR achieves a success rate of* 90% *in the left lumen. (B) In the straight lumen, the success rate is* 60%. *(C)) The UMR's success rate in the right lumen is* 20%.

2.3.2 Controlled actuation with the $\mathcal{F}$ controller

Fig. 6 illustrates motion control trials of the UMR using control system $\mathcal{F}$. For each pathway, we conduct 10 control trials, each comprising two consecutive runs: one from the proximal end of the phantom to the distal end of the path, and the other returning to the starting point. When the UMR is controlled along the left curved lumen (Fig. 6A), we achieve a success rate of 90%. Figs. 6A(i) and A(ii) provide two successful trials with MAE of 2.2 ± 4.9 and 2.9 ± 3.9 mm, respectively. Notably, in this pathway, backward motion proves to be more challenging due to the UMR's rotational direction, which induces a sideway drift opposing the in-plane torque used for steering. Consequently, as demonstrated in the trial in Fig. 6A(iii), the UMR incorrectly enters the unintended path into the right curved lumen.

When the UMR is assigned the task of moving along the straight path, the success rate of the control system drops to 60%, as shown in Fig. 6B. A successful trial of the UMR along the straight pathway is achieved with a MAE of 4.4 ± 1.5 mm (Fig. 6B(i)). It is worth noting that the UMR's path inside the left curved lumen is obscured temporarily by the RPM itself, resulting in a disconnected appearance in the X-ray Fluoroscopy image (Fig. 6B(ii)). In the trial

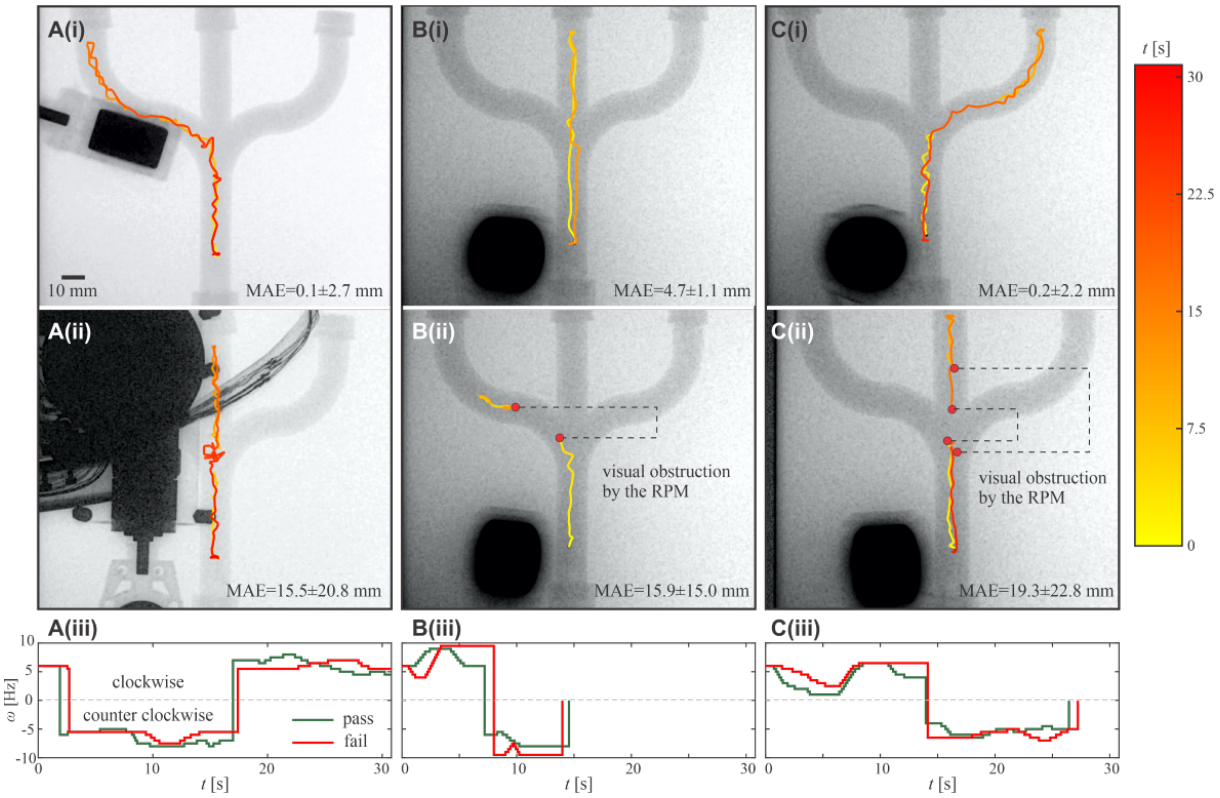

Fig. 7: *Control of the untethered magnetic robot (UMR) is implemented through the $\mathcal{F}+\mathcal{C}$ control system, which relies on the geometry of the desired path and the UMR speed. The success rate is assessed by conducting 10 trials along the left and right lumens, as well as the straight lumen. In each trial, the UMR is controlled to move forward toward the distal end of any of the paths and subsequently return to the starting point. (A) The UMR achieves a success rate of* 90% *in the left lumen. (B) In the straight lumen, the success rate is* 60%. *(C) The UMR's success rate in the right lumen is* 80%.

depicted in Fig. Fig. 6B(iii), the UMR enters another unintended pathway, specifically the right curved lumen.

Finally, when the control system $\mathcal{F}$ is adjusted to guide the UMR along the right curved lumen, the success rate decreases to 20%. Fig. 6C illustrates three distinct trials in which the UMR is directed to swim along the right curved lumen. Some trials successfully follow the intended path (Fig. 6C(i)). However, executing in-plane rotations by rotating the RPM's rotation axis clockwise has presented challenges. When the UMR is actuated to rotate about its long axis while moving forward, it tends to drift sideways (Figs. 6C(ii) and 6C(iii)), influenced by the direction of rotation. This behavior becomes particularly evident when the UMR is actuated far from any solid boundary. In such cases, it is expected that the UMR will follow a curved trajectory as it moves forward [1]. Hence, executing a turning maneuver (clockwise rotation about the z-axis) proved to be more challenging for the UMR, primarily due to the sideways drift induced by the screwing motion, which counteracted the in-plane torque required for steering. In such situations, the operator can offer additional input to enhance steering.

2.3.3 Controlled actuation with the $\mathcal{F}+\mathcal{C}$ controller

The previous control maneuvers are replicated using the control system $\mathcal{F}+\mathcal{C}$, allowing the operator to regulate the UMR's swimming speed based on its position in the X-ray Fluoroscopy images (Fig. 7). In the left curved lumen, the success rate of the $\mathcal{F}+\mathcal{C}$ configuration remains at 90% (Fig. 7A). Regardless of the control configuration, the UMR can easily access this path because the sideway drift caused by screwing and the in-plane steering torque (counterclockwise about the z-axis) act in the same direction (Fig. 7A(i)). Note that the difference between

the control inputs provided by the operators in the successful and failed trials is quite similar. Fig. 7A(ii) displays the UMR's response when the operators adjusted its angular velocity based on visual feedback. Despite the similarities in the control inputs shown in Fig. 7A(iii), the UMR's responses vary significantly. Therefore, it is crucial to enhance the steering torque at the location of the bifurcation.

Similar to the $\mathcal{F}$ controller, when the $\mathcal{F}+\mathcal{C}$ controller is employed to guide the UMR along the straight lumen, the success rate is measured at 60% (e.g., Fig. 7B(i)). Notably, in all unsuccessful trials (e.g., Fig. 7B(ii)), the UMR entered the left curved lumen. Fig. 7B(iii) illustrates the two inputs associated with both successful and failed trials, underscoring the significance of the control action at the bifurcation point, where the UMR could potentially enter an unintended pathway. A significant improvement in the success rate is observed for the right lumen, where a success rate of 80% is measured (Fig. 7C). Here the UMR's actuation frequency was decreased to ensure strong magnetic steering torque throughout the turn into the right lumen. This demonstrates the significance of the operator's input through the control system $\mathcal{C}$.

The integration of real-time X-ray Fluoroscopy imaging with RPM control allows operators to visually guide the UMR through complex vascular pathways, making it a promising technique for medical applications where precise navigation is crucial. We observe the importance of operator involvement in UMR control, especially in challenging scenarios. The operator's ability to adjust the UMR's movements based on the visual feedback from X-ray Fluoroscopy significantly improved success rates. This finding suggests that while automation is valuable, operator input remains critical, particularly in intricate tasks.

This chapter also uncovers challenges in executing in-plane rotations. Sideways drift induced by the UMR's screwing motion posed difficulties in these maneuvers. This observation informs future research directions, encouraging the development of more robust control strategies to address such challenges. Nevertheless, our work showcases the potential of combining real-time imaging with UMR control for medical applications. It emphasizes the complementary role of operators in controlling UMRs and highlights challenges that can guide future research in this field.

2.4 Conclusions

This chapter highlights the effectiveness of a predictive feedforward control system ($\mathcal{F}$) and a 2-DOF control system ($\mathcal{F}+\mathcal{C}$) in guiding a UMR through complex vascular pathways using an X-ray-guided robotic platform. Control system $\mathcal{F}$ demonstrated successful tracking in the left curved lumen but faced challenges in the straight lumen and the right curved lumen. The addition of operator control in $\mathcal{C}$ significantly improved success rates, especially in the right curved lumen. However, this chapter revealed challenges in executing in-plane rotations, particularly clockwise rotations about the z-axis, due to the counteracting effects of the UMR's screwing motion-induced sideways drift. This underscores the importance of operator involvement in controlling screw-type UMRs in complex environments and suggests future research directions to refine control algorithms, increase autonomy, and explore different UMR designs and actuation methods to overcome these challenges while improving navigation.

References

[1] N. D. Nelson, J. Delacenserie and J. J. Abbott, "An empirical study of the role of magnetic, geometric, and tissue properties on the turning radius of magnetically driven screws," in *Proceedings of the IEEE International Conference on Robotics and Automation (ICRA)*, Karlsruhe, Germany, pp. 5372-5377, 2013.

[2] J. Leclerc, H. Zhao, D. Bao, and A. T. Becker, "In Vitro design investigation of a rotating helical magnetic swimmer for combined 3-D navigation and blood clot removal," *IEEE Trans. Robot.*, vol. 36, no. 3, pp.975-982, 2020.

[3] A. Aziz, S. Pane, V. Iacovacci, N. Koukourakis, J. Czarske, A. Menciassi, M. M. Sánchez, and O. G. Schmidt, "Medical imaging of microrobots: Toward in vivo applications," *ACS Nano*, vol. 14, no. 9, pp. 10865-10893, Sep. 2020.

[4] A. Servant, F. Qiu, M. Mazza, K. Kostarelos, B. J. Nelson, "Controlled in vivo swimming of a swarm of bacteria-like microrobotic flagella," *Advanced Materials*, vol. 27, no. 19, pp. 2981-2988, Apr. 2015.

[5] E. E. Niedert, C. Bi, G. Adam, E. Lambert, L. Solorio, C. J. Goergen, and D. J. Cappelleri, "A tumbling magnetic microrobot system for biomedical applications," *Micromachines*, vol. 11, no. 9, Sep. 2020.

[6] T. W. R. Fountain, Prem V. Kailat, and J. J. Abbott, "Wireless control of magnetic helical microrobots using a rotating-permanent-magnet manipulator," in *Proc. IEEE Int. Conf. Robot. Autom.*, 2011, pp. 576–581.

3 X-Ray-Guided Magnetic Fields for Wireless Control of Untethered Magnetic Robots in Cerebral Vascular Phantoms

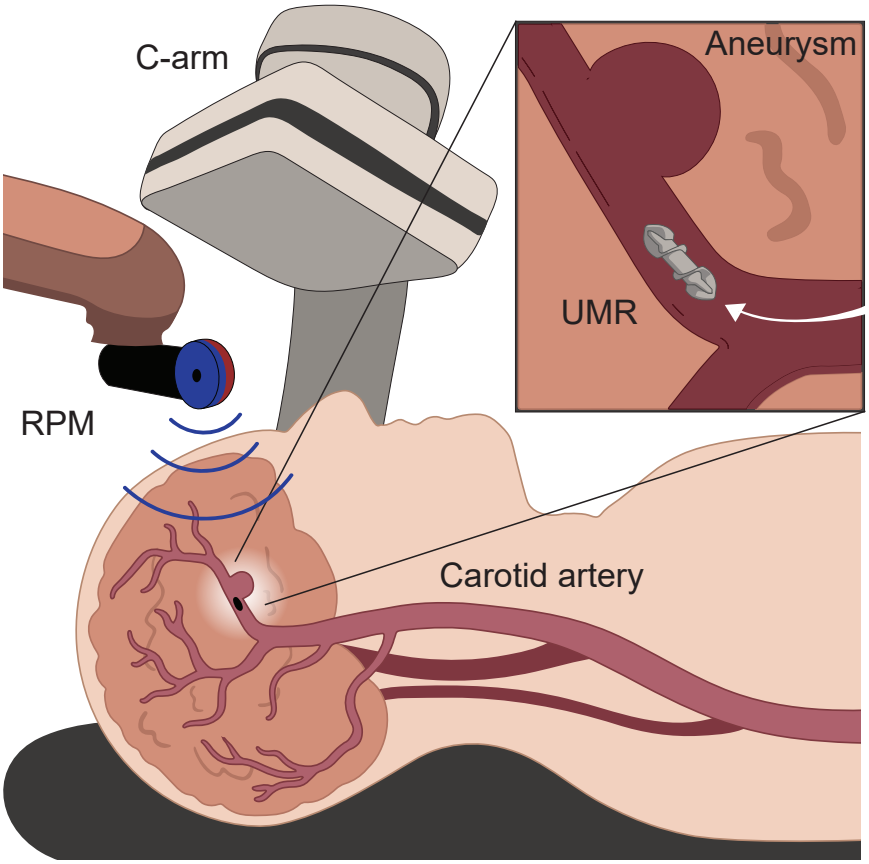

Fig. 8: *Untethered magnetic robots (UMRs) offer a novel approach for navigating bodily fluids, enabling access to hard-to-reach regions within the human body. This technology presents an alternative minimally invasive solution for addressing strokes and brain aneurysms, enhancing the precision and safety of neurosurgical interventions. UMRs can be controllably moved toward the desired target using X-ray-guided magnetic fields. A robotic C-arm is utilized for precise localization and mapping of the vascular network's tomography, while a rotating magnetic field enables wireless actuation along any desired vascular route.*

In the realm of neurosurgery, strokes and brain aneurysms present significant challenges due to the intricate nature of the cerebral vasculature. Traditional surgical approaches may involve invasive procedures with inherent risks and the success of current catheter and guidewire-based methods in peripheral intervention is limited by the competing requirements and tradeoffs between stiffness, diameter, and controllability. Therefore, there is a growing interest in developing innovative techniques that enhance precision and minimize patient trauma [1]-[5]. One promising avenue is the use of UMRs guided by X-ray Fluoroscopy imaging, which holds potential for revolutionizing neurosurgical interventions. This chapter explores the application of wireless control of UMRs within cerebral vascular phantoms, leveraging X-ray-guided magnetic fields to navigate through complex vascular structures with enhanced accuracy and safety.

Strokes and brain aneurysms are among the most critical neurological conditions, often resulting in severe disabilities or fatalities. Strokes occur when blood flow to the brain is disrupted, leading to tissue damage, while brain aneurysms involve the weakening and ballooning of blood vessel walls, posing a risk of rupture and hemorrhage (Fig. 8). Both conditions necessitate precise and minimally invasive treatment strategies to mitigate their devastating effects and improve patient outcomes.

UMRs controlled by X-ray-guided magnetic fields represent a cutting-edge technology in the

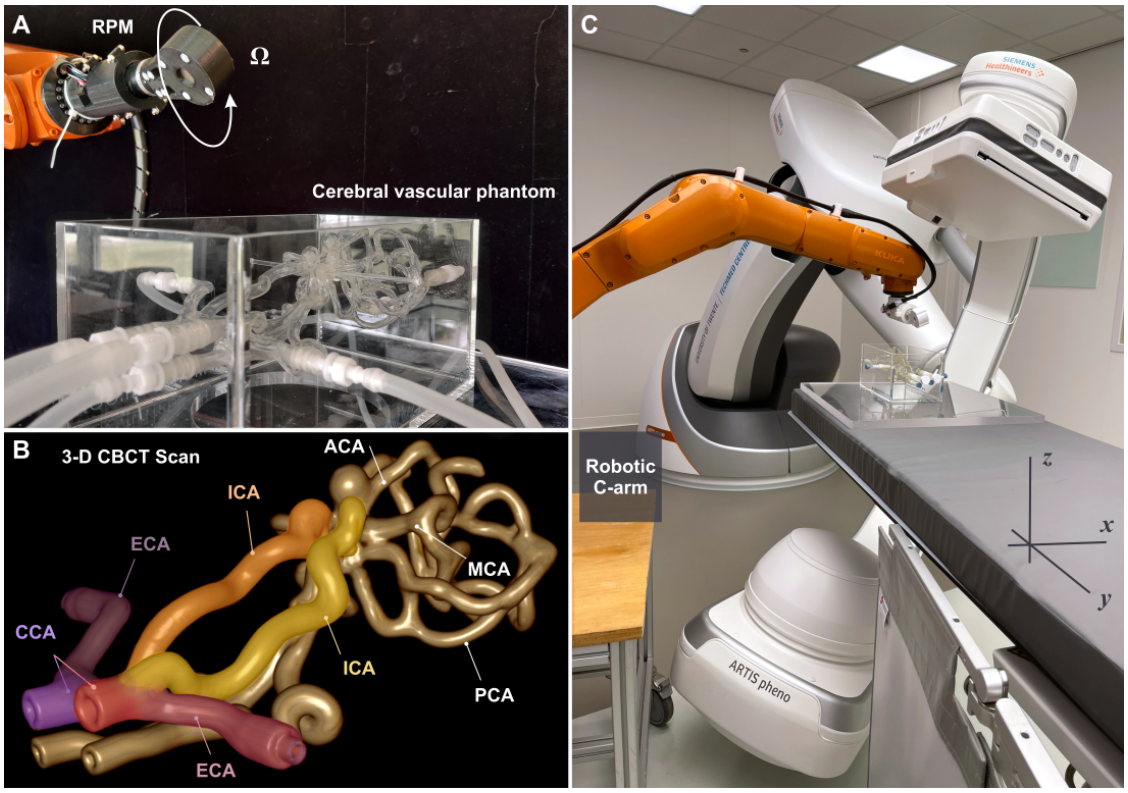

Fig. 9: *Navigating within a cerebral vascular phantom, untethered magnetic robots (UMRs) measuring 9 mm in length and 3 mm in diameter are controlled using X-ray-guided magnetic fields. Demonstrating agility, (A) the rotation axis of the magnetic field aligns parallel with the centerline of the vessel. (B) The vascular model is reconstructed using cone-beam computed tomography (CBCT) scans. A 4-mm-diameter UMR can navigate from the common carotid artery (CCA) toward the external carotid artery (ECA) and the internal carotid artery (ICA). The posterior cerebral artery (PCA), anterior cerebral artery (ACA), and middle cerebral artery (MCA) are not accessible to the UMR. (C) X-ray Fluoroscopy images and CBCT scans are obtained using a robotic C-arm for wireless control and to determine the tomography of the environment, respectively.*

field of minimally invasive surgery, offering the potential for precise and targeted interventions within delicate anatomical structures [6]. These robots can navigate through the body using external magnetic fields (Fig. 8), enabling minimally invasive procedures with reduced tissue damage and shorter recovery times [7, 8]. The integration of X-ray guidance further enhances navigation accuracy and real-time visualization of UMRs, facilitating intricate maneuvers in challenging anatomical regions such as the cerebral vasculature. This approach holds promise for improving the treatment of strokes and brain aneurysms, two critical neurological conditions with significant morbidity and mortality rates. By combining UMRs with X-ray imaging, neurosurgeons can achieve unprecedented levels of precision and safety in their interventions, ultimately leading to better patient outcomes and enhanced quality of care.

The remainder of this chapter is organized as follows: Section 3.1 provides descriptions pertaining to the UMRs, the robotic C-arm, the wireless manipulation system, and the vascular model. Section 3.2 presents the frequency response experimental results of the UMR inside a confinement and provides experimental results of the UMR inside the cerebral vascular phantom. Finally, Section 3.3 concludes the chapter and provides directions for our future work.

3.1 X-ray-guided untethered magnetic robots

When a magnetically actuated screw-shaped body is contained within a 3D confinement and is subjected to a rotating magnetic field with a rotation axis parallel to the centerline of the

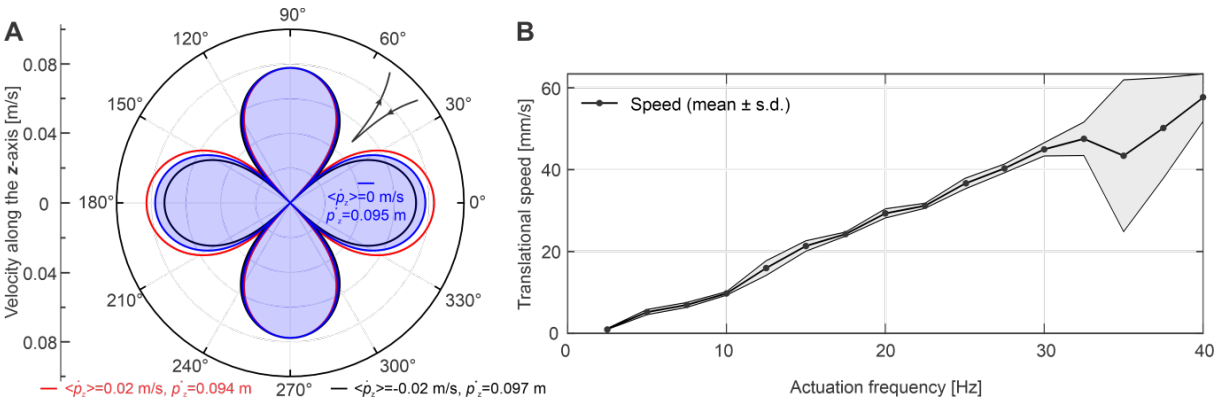

Fig. 10: *Characterization of the active suspension of the untethered magnetic robot (UMR) and frequency response. (A) Active suspension is achieved by synchronously rotating the UMR and the rotating permanent magnet (RPM) actuator, with the RPM-UMR gap controlled at 0.095 m. The rose curves are calculated using Equation 4 for* $m = 6.2 \times 10^{-4}$ $A.m^2$, $M = 19.9$ $A.m^2$, *and* $\rho = 997$ kg/m^3. *The angle bracket denotes averaging over one rotation period. (B) Translational speeds at varying actuation frequencies up to the maximum frequency are depicted. The* in vitro *experiment was conducted in water with a stationary RPM positioned 15 cm from the tube, which had a diameter of 9.525 mm. A linear relationship between the frequency and translational speed is evident.*

confinement, it will move forward or backward based on the direction of the field. The rotation axis of the magnetic field can be controlled by robotically controlling the pose of a RPM [9], as shown in Fig. 9(A). Translating the RPM with respect to the UMR enables it to rotate in sync along an intended path inside a vascular system (Fig. 9(B)). Additionally, the RPM-UMR gap can be controlled simultaneously such that the weight of the UMR is compensated by the field-gradient pulling under X-ray guidance (Fig. 9(C)).

3.1.1 Characterization of untethered magnetic robots

The UMRs are manufactured using additive techniques, allowing for the precise construction of screw-shaped bodies, Chapter 2. Additionally, they are coated with a biocompatible material to enhance their compatibility within biological systems, refer to Section 4.2. These bodies are designed to accommodate small permanent magnets, placed to provide the necessary propulsion and maneuverability within the vascular routes. This fabrication approach ensures the creation of UMRs with consistent dimensions and magnetic properties. When submerged in a viscous fluid with density ρ, the UMR's vertical displacement with respect to the RPM actuator, p_z, is governed by $\frac{1}{2}\rho\dot{p}_z^2 c_\mathrm{d} A = -F_\mathrm{m} - F_\mathrm{g}$. The left-hand side represents a drag component, arising from the resistance to translating the UMR along the $\boldsymbol{z}$-axis. This resistance is balanced by the field gradient pulling, F_m, and the gravitational force, F_g, and yields

$$\dot{p}_z^2 = \frac{2}{\rho c_\mathrm{d} A}\left(\frac{1}{2}\frac{3\mu_0 M m}{2\pi p_z^4} - \Delta\rho g V\right), \tag{4}$$

where c_d and A represent the lateral drag coefficient of the UMR and the cross-sectional area, respectively. Additionally, μ_0 denotes the permeability of free-space, while M and m denote the magnetic moment of the RPM actuator and the UMR, respectively. Further, $\Delta\rho$ is the density difference for the UMR and the surrounding fluid, g is the gravitational constant, and V the volume of the UMR.

Equation (4) is valuable for determining an optimal RPM-UMR gap that achieves a balance between magnetic and gravitational forces. If the RPM-UMR gap decreases below this optimal value, the field-gradient pulling will attract the UMR toward the RPM actuator. Conversely, if the RPM-UMR gap increases beyond this optimal value, the UMR will fall under the influence of its own weight. Fig. 10(A) displays three rose curves for three RPM-UMR gaps. The solution of

Table 1: *The untethered magnetic robot is controlled to swim along the left and right common carotid artery (CCA) toward the left and right external carotid artery (ECA) and internal carotid artery (ICA). The average path velocity (VAP) is used to characterize the motion along each vascular route. The averages and standard deviations are computed based on 10 trials along each route.*

Vascular route	**Forward VAP [mm/s]**	**Backward VAP [mm/s]**	**Obstruction time** $[s]$	**Success rate** [%]
Right CCA to right ECA	18.2 ± 6.1	10.8 ± 3.1	0.02 ± 0.06	83.3 ($n = 12$)
Right CCA to right ICA	14.5 ± 0.3	31.7 ± 1.2	2.0 ± 0.5	100 ($n = 10$)
Left CCA to left ECA	19.6 ± 2.0	14.0 ± 2.4	0.3 ± 0.3	83.3 ($n = 12$)
Left CCA to left ICA	19.3 ± 3.4	28.7 ± 3.4	3.0 ± 1.2	90.9 ($n = 11$)

Equation (4) yields smooth curves arranged symmetrically about a common center, indicating that the velocity periodically increases to a maximum and then decreases to zero. However, there exists an optimal RPM-UMR gap (i.e., $p_z = 0.095$ m for a UMR and RPM of magnetic moment of $m = 6.2 \times 10^{-4}$ and $M = 19.9$ A.m^2, respectively) that yields zero vertical velocity on average. For an RPM-UMR gap of $p_z < 0.095$ m, the average vertical velocity component is greater than zero, indicating that the UMR would be attracted toward the RPM. In contrast, when the RPM-UMR gap is $p_z > 0.095$ m, the average vertical velocity component is less than zero, indicating that the UMR would move away from the RPM.

3.1.2 X-ray-guided magnetic control system

The tomography of the cerebral vascular phantom (Anatomical Vascular Model, HN-S-A-010, ELASTRAT, Switzerland) is generated from CBCT scans, as depicted in Fig. 9(B), using a robotic C-arm (Siemens Healthineers ArtisPheno, Erlangen, Germany). Using this tomography, each vascular route is mapped to determine the desired rotation axis for the magnetic field. This axis is adjusted according to the UMR's position along each vascular route (e.g., from the right common carotid artery to the right external carotid artery). Subsequently, the rotation axis of the RPM is controlled using the 6-DOF manipulator (KUKA KR-10 1100-2, KUKA, Augsburg, Germany) shown in Fig. 9(C), while simultaneously adjusting the RPM-UMR gap based on Equation (4) to provide active suspension during helical propulsion.

3.1.3 Description of cerebral vascular phantoms

The cerebral vascular phantom in this chapter replicate the intricate geometry of human cerebral vasculature, including arteries such as the internal carotid artery (ICA) with a diameter ranging from 4.3 to 5.8 mm, common carotid artery (CCA) with a diameter ranging from 7.7 to 8.2 mm, external carotid artery (ECA) with a diameter ranging from 4 to 4.3 mm, vertebral artery with a diameter ranging from 2 to 4 mm, posterior cerebral artery (PCA) with a diameter ranging from 2 to 3 mm, anterior cerebral artery (ACA) with a diameter of 2.8 mm, and middle cerebral artery (MCA) with a diameter ranging from 3 to 5 mm. They encompass diverse anatomical features, including varying lengths and branching patterns, mimicking the complex anatomy of cerebral arteries, such as bifurcations, tortuous pathways, and variations in vessel diameter. Based on the varying diameters of the mentioned vascular routes, a UMR with a diameter of less than 2 mm should be able to navigate throughout the entire system. However, our 4-mm-diameter UMR is limited to navigating through the CCA toward either the ECA or the ICA due to its size.

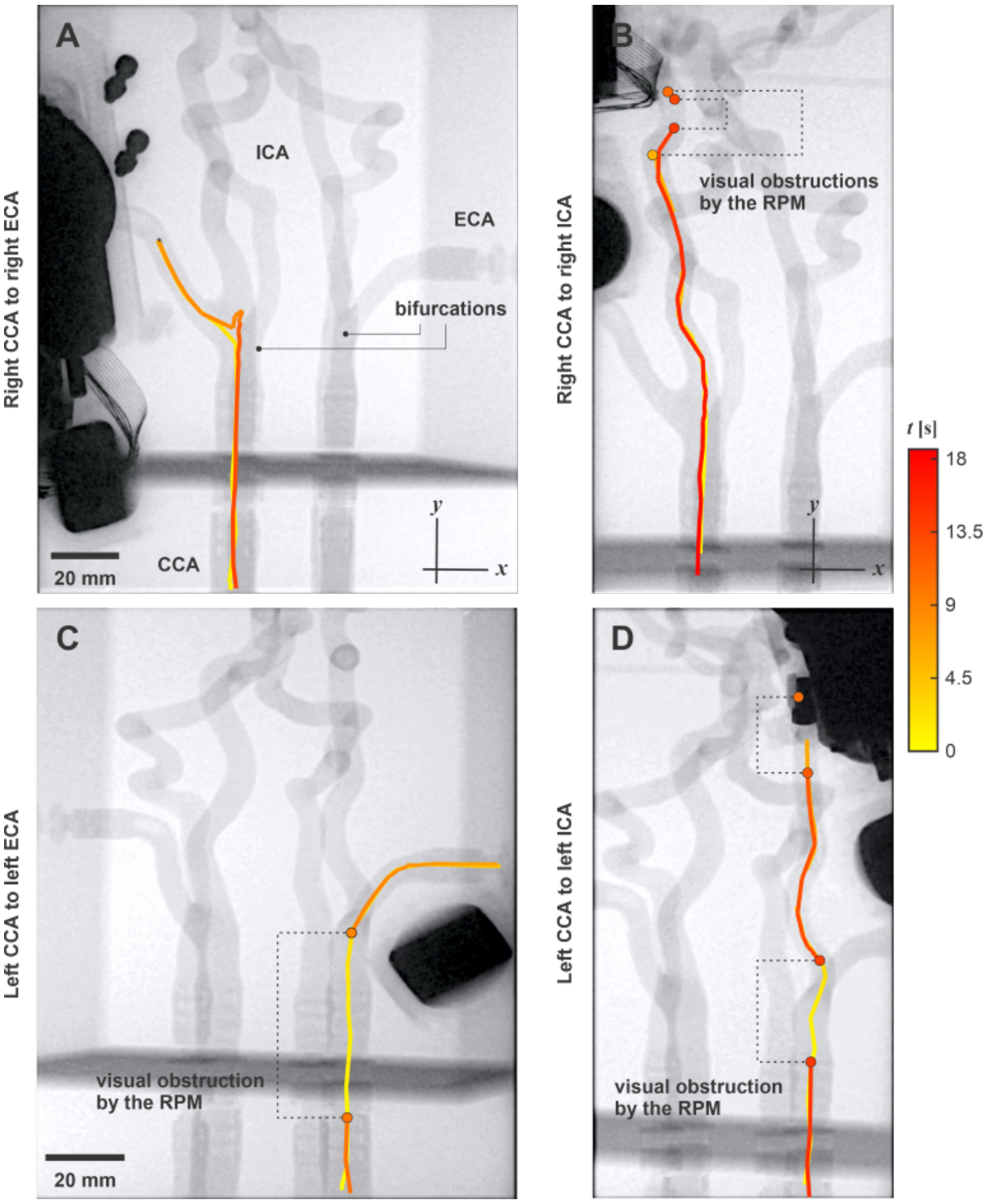

Fig. 11: *The untethered magnetic robot (UMR) is moved using X-ray-guided magnetic fields along desired paths within a cerebral vascular phantom. The black dashed lines indicate regions of visual obstruction in which the rotating permanent magnet obstructs the field of view between the detector and emitter of the C-arm. (A) The UMR is controlled to swim from the right common carotid artery (CCA) to the right external carotid artery (ECA). (B) Motion control is achieved between the right CCA to the right internal carotid artery (ICA). (C) The UMR is controlled between the left CCA to the left ECA. (D) Motion control is achieved between the left CCA to the left ICA.*

3.2 Evaluation of wireless control performance

3.2.1 Frequency response characterization

The frequency response of the UMRs is characterized within a range of 1 to 40 Hz, as depicted in Fig. 10(B). This range is constrained by the frequency capabilities of the RPM-actuator. The translational speed of the RPM shows a linear rise with the actuation frequency until 40 Hz, suggesting that the step-out frequency of the UMR exceeds 40 Hz. At each actuation frequency, the UMR is allowed to achieve straight runs along a transparent tube with a diameter of 9.525 mm, and the average speed is calculated offline from the captured camera footage. The shaded region represents the standard deviation. The determination of the drag coefficient c_{d} was conducted using COMSOL (COMSOL inc., Sweden), whereby the CAD model of the UMR was subjected to varying flow rates against its long axis. This analysis yielded an average c_{d} value of 0.94.

3.2.2 Motion control inside the cerebral vascular phantom

To showcase the controllable movement of the UMR within the cerebral vascular phantom, we establish four specific vascular routes. For each route, we conduct motion control tests consisting of ten runs, encompassing both forward and backward swimming movements.

Right CCA - right ECA

In this vascular route, the UMR starts from the proximal end of the right CCA and progresses towards the distal end of the right ECA, as depicted in Fig. 11(A). The UMR proceed toward the bifurcation, then turns towards the right ECA, ascending toward its distal end. At $t =$ 9 s, the UMR's motion direction is reversed, enabling it to swim downward along the ECA, and subsequently, it swims horizontally past the bifurcation along the CCA. At an actuation frequency of 9 Hz, the average path velocities (VAPs) for forward and backward motion are measured as 18.2 ± 6.1 and 10.8 ± 3.1 mm/s ($n = 10$), respectively. During traversal along the right CCA-right ECA route, no visual obstructions are observed in the collected X-ray Fluoroscopy images. The success rate along this route is calculated as 83.3% ($n = 12$).

Right CCA - right ICA

To navigate from the right CCA and reach the distal end of the right ICA, the UMR must traverse past the bifurcation of the ECA and the ICA, ascending along the ICA toward its distal end during the forward run. Along this route, the diameter of the vessel decreases progressively from 8.2 mm to 4.3 mm as the UMR advances. Therefore, the average VAP is 14.5 ± 0.3 mm/s. When the motion is reversed to enable the UMR to swim back toward the proximal end of the CCA, the UMR descends along the ICA from the distal end toward the bifurcation and then swims toward the proximal end of the CCA, at an average VAP of 31.7 ± 1.2 mm/s. Unlike the right CCA - right ECA route, two obstructions caused by the RPM-actuator are encountered during both the forward and backward runs, as shown in Fig. 11(B). For the ten trials along this vascular route, the average obstruction time is measured to be 2.0 ± 0.5 s. However, due to the downward drift (along the $-\boldsymbol{z}$-axis) by the UMR, its preferred path is the bottom most bifurcation (as indicated in Fig. 11(B)), this resulted in an increased success rate along this vascular route to 100% ($n = 10$).

Left CCA - Left ECA

Now, we shift our focus to the left CCA and ECA. Similar to the previous trials, the UMR begins its movement from the proximal end of the left CCA, progresses toward the bifurcation, and then swims downward along the narrower left ECA, as depicted in Fig. 11(C). Unlike the

previous instances of visual obstruction, the dynamic behavior of the RPM-actuator obstructs visual feedback in this trial, during the backward motion towards the CCA. However, despite this obstacle, the UMR and the RPM remain coupled throughout both the forward and backward runs. Along this vascular route, the average forward and backward VAP are measured as 19.6 ± 2.0 mm/s and 14.0 ± 2.4 mm/s, respectively. The average visual obstruction time for the runs is 0.3 ± 0.3 s. The success rate decreases to 83.3% ($n = 12$) due to the decreasing diameter of the ECA, which limits the movement of the UMR.

Left CCA - left ICA

Finally, during the navigation of the left CCA - left ICA route, additional visual obstructions are encountered, particularly during the backward run. Fig. 11(D) illustrates the UMR's forward movement from the proximal end of the left CCA toward the distal end of the left ECA. In this forward run, the UMR ascends toward the region with a decreasing diameter at an average VAP of 19.3 ± 3.4 mm/s. Upon reversing its motion, a visual obstruction is encountered along the left CCA. Another obstruction occurs as the UMR passes the bifurcation and enters the left CCA. However, despite these consecutive visual obstacles, the UMR maintains synchronization with the RPM-actuator. The average forward and backward VAPs are measured as 19.3 ± 3.4 mm/s and 28.7 ± 3.3 mm/s, respectively, while the average obstruction time is measured as 3.0 ± 1.2 s and the success rate is 90.9% ($n = 11$).

3.2.3 Interpretation of experimental findings and challenges

The experimental results of this chapter showcase the potential of UMRs for controlled navigation within a cerebral vascular phantom. Through rigorous testing across defined vascular routes, the UMRs demonstrated promising capabilities in maneuvering through complex vascular structures, overcoming challenges such as varying diameters and visual obstructions. The success rates obtained in controlling the UMRs through different vascular routes provide quantitative evidence of their effectiveness. The high success rates, ranging from 83.3% to 100% (Table 1), underscore the reliability and precision of UMRs in navigating through cerebral vasculature. Notably, achieving a 100% success rate when navigating from the right CCA to the right ICA highlights the UMRs' adaptability to different vessel types and configurations.

However, it is worth noting the challenges encountered during the experiments, such as visual obstructions and varying diameters along the vascular routes. These challenges reflect real-world scenarios in neurosurgical procedures where precise navigation through tortuous and narrow vessels is crucial. Despite these challenges, the UMRs maintained stable control and successfully completed their designated paths, demonstrating robust performance under challenging conditions. While the 4-mm-diameter UMR successfully navigated from the CCA to either the ECA or the ICA, it was limited in its ability to access other cerebral arteries. The finding underscores the importance of UMR size optimization, suggesting that a smaller diameter, ideally below 2 mm, would enable comprehensive navigation throughout the entire vascular system. This insight highlights a critical consideration for further development and refinement of UMR technology, emphasizing the need for size reduction to enhance versatility and applicability in neurosurgical interventions.

3.3 Conclusions

This chapter confirms the viability of using UMRs for precise navigation within a cerebral vascular phantom. Through structured vascular routes and motion control trials, we demonstrate the UMRs' adeptness in navigating intricate vascular structures, addressing challenges such as varying diameters and visual obstructions. The success rates, ranging from 83.3% to 100% across different routes (i.e., left and right CCA toward left and right ECA and ICA), highlight the

potential of UMRs for minimally invasive biomedical interventions in cerebral vasculature, offering promising advancements in neurosurgical procedures and the treatment of cerebrovascular conditions.

In future work, we plan to utilize an *ex vivo* model to simulate more realistic physiological conditions and anatomical complexities [10]. This will involve decreasing the size of the UMR to enable navigation throughout the entire cerebrovascular system of the *ex vivo* model, addressing the need for miniaturization to accommodate the intricate anatomy of cerebral vasculature. By incorporating an *ex vivo* model, we aim to evaluate the performance of UMRs in a more lifelike environment, considering factors such as blood flow dynamics and tissue interactions. This approach will provide valuable insights into the behavior and efficacy of UMR-based interventions, advancing their development and translation for neurosurgical procedures and cerebrovascular therapies.

References

[1] R. Dreyfus et al., "Dexterous helical magnetic robot for improved endovascular access," *Sci. Robot.*, vol. 9, no. eadh0298, 2024.

[2] J. B. Mathieu, G. Beaudoin, and S. Martel, "Method of propulsion of a ferromagnetic core in the cardiovascular system through magnetic gradients generated by an MRI System," *IEEE Trans. Biomed. Eng.*, vol. 53, pp. 2929-2935, 2006.

[3] Q. Wang, L. Yang, J. Yu, P. W. Y. Chiu, Y.-P. Zheng, and L. Zhang, "Real-Time magnetic navigation of a rotating colloidal microswarm under ultrasound guidance," *IEEE Trans. Biomed. Eng.*, vol. 67, no. 12, pp. 3519-3528, Dec. 2020.

[4] T. Wang, H. Ugurlu, Y. Yan, et al., "Adaptive wireless millirobotic locomotion into distal vasculature," *Nat. Commun.*, vol. 13, article 4465, 2022.

[5] X. Liu et al., "Magnetic soft microfiberbots for robotic embolization," *Sci. Robot.*, vol. 9, no. eadh2479, 2024.

[6] Leendert-Jan Ligtenberg, Nicole Rabou, et al., "Ex Vivo Validation of Magnetically Actuated Intravascular Untethered Robots in a Clinical Setting," Preprint (Version 1), Research Square, December 3, 2023. Available at: [https://doi.org/10.21203/rs.3.rs-3526473/v1].

[7] A. Hong, A. J. Petruska, and B. J. Nelson, "Tracking a magnetically guided catheter with a single rotating C-Arm," in *Proc. IEEE Int. Conf. Robot. Autom.*, Seattle, WA, pp. 618-623, 2015.

[8] J. Leclerc, H. Zhao, D. Bao, and A. T. Becker, "In vitro design investigation of a rotating helical magnetic swimmer for combined 3-D navigation and blood clot removal," *IEEE Trans. Robot.*, vol. 36, no. 3, pp. 975-982, 2020.

[9] T. W. R. Fountain, Prem V. Kailat, and J. J. Abbott, "Wireless control of magnetic helical microrobots using a rotating-permanent-magnet manipulator," in *Proc. IEEE Int. Conf. Robot. Autom.*, 2011, pp. 576–581.

[10] A. Servant, F. Qiu, M. Mazza, K. Kostarelos, and B. J. Nelson, "Controlled in vivo swimming of a swarm of bacteria-like microrobotic flagella," *Adv. Mat.*, vol. 27, no. 19, pp. 2981-2988, Apr. 2015.

4 *Ex Vivo* Validation of Magnetically Actuated Intravascular Untethered Robots in a Clinical Setting

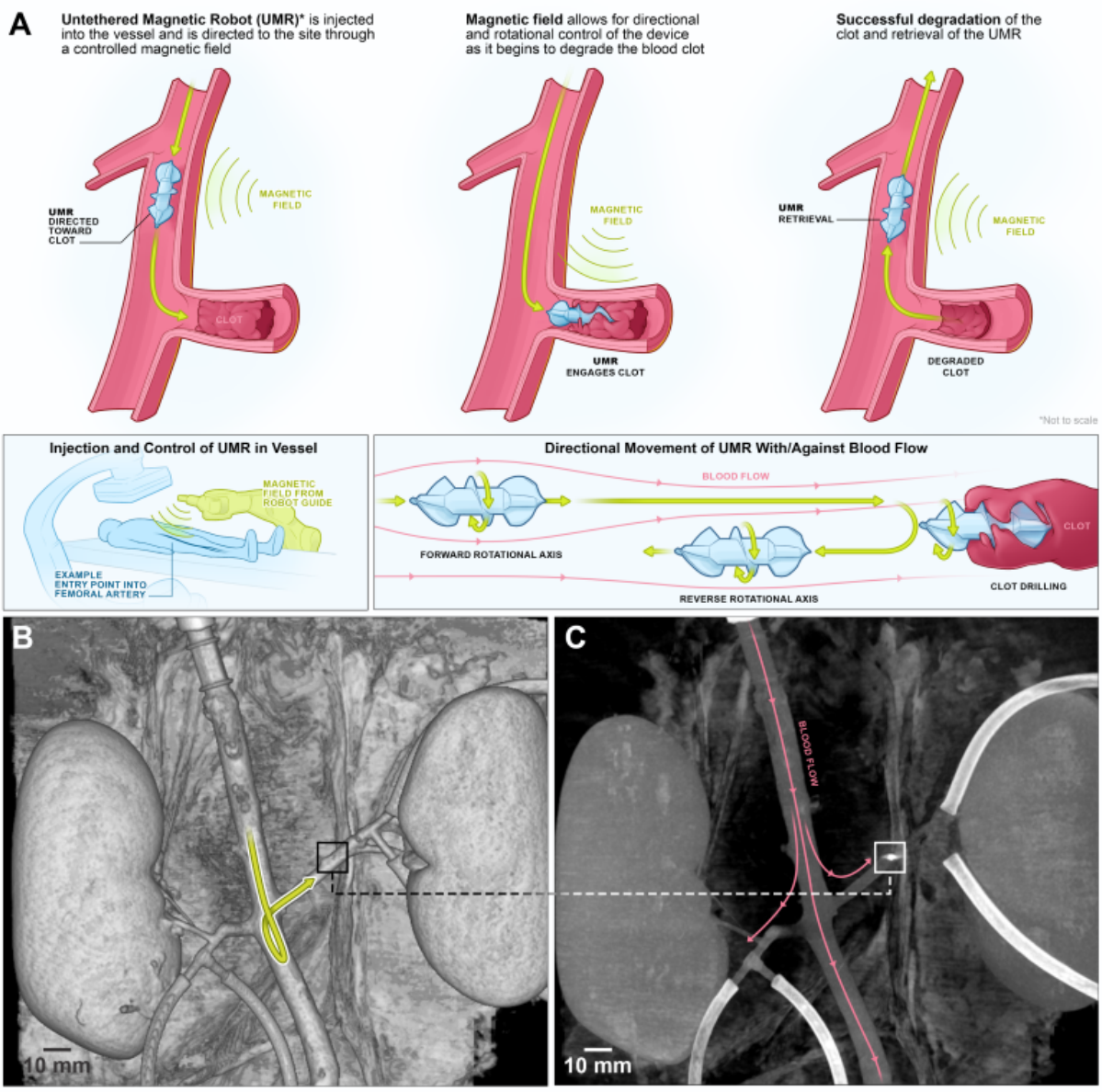

Fig. 12: *The untethered magnetic robot (UMR) can swim inside natural pathways of a porcine aorta model under controlled conditions, enabling interventions and retrieval with minimal incisions. (A) The wireless actuation and non-invasive localization of UMRs are achieved through a robotic platform, consisting out of an external rotating magnetic field and a C-arm imaging system. UMRs navigate both with and against the blood flow for various interventions. (B)-(C) A 9-mm-long UMR moves both with and against the blood flow inside the abdominal aorta and is then guided to swim within the left renal artery. The UMR's location is highlighted by squares in the CBCT scans, and its trajectory is depicted by the yellow arrow.*

Untethered magnetic robots have the potential to navigate through bodily fluids for surgical or therapeutic procedures, such as targeted therapy and material removal. When operating *in vitro*, the navigation of UMRs is often greatly simplified by a controlled environment in which detailed analysis of one or more important physical effects are studied inside petri dishes or test tubes. This type of experiment has allowed to advance our knowledge about the incorporation of a specific physical intelligence into UMRs, which is significantly important at small scales, allowing them to be used as end-effectors of wireless manipulation systems [1, 2]. Mi-

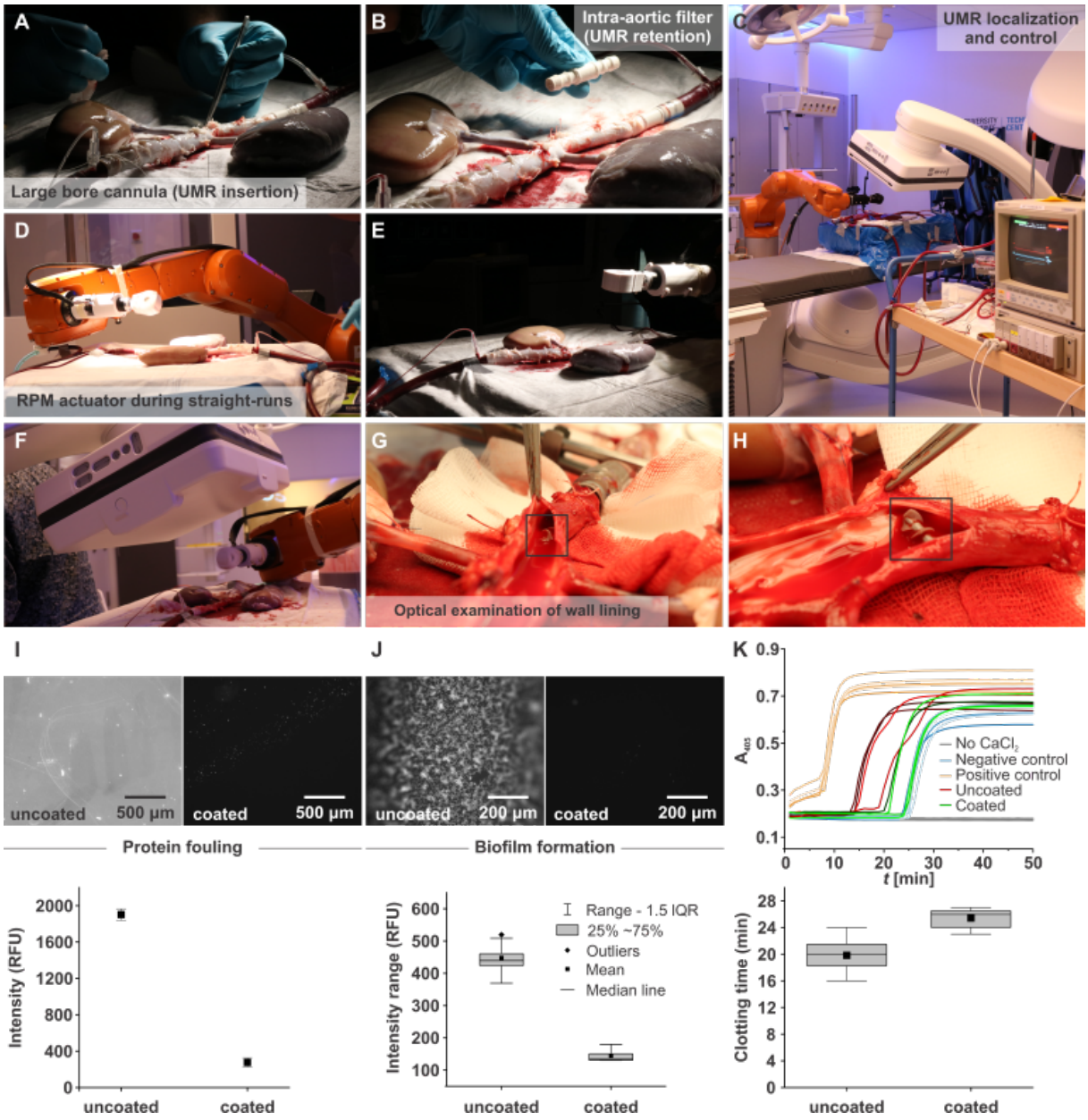

Fig. 13: Ex vivo *trials are conducted using a porcine aorta model. (A) The* ex vivo *organs are harvested and connected to a circulation pump prior to each motion control session. (B) Placement of an intra-aortic 3D printed filter allows the untethered magnetic robot (UMR) to remain inside the aorta irrespective of the ongoing blood circulation. (C)-(F) Wireless magnetic actuation and C-ARM imaging systems enable control and localization, respectively. (G)-(H) Optical examination of the internal wall lining of the vessels shows no risk of damage by the UMR. The black squares indicate the UMR. (I)-(K) Hemocompatibility tests included (**I**) protein fouling, (J) biofilm formation and (K) coagulation evaluation.*

croactuation [3], high-precision transportation and cargo delivery [4, 5], gamete transport [6, 7], microassembly [8, 9], diagnosis [10], material removal and targeted drug delivery [11] have been demonstrated *in vitro* at a number of scales [12]. While these promising experiments have indeed demonstrated the significant potential of UMRs across various technologies and therapies, it is important to acknowledge that they currently fall short of replicating the intricate conditions found within living organisms. As a result, the full extent of their capabilities and limitations remains unexplored.

It is unlikely that UMRs can effectively be used *in vivo* unless multiple hurdles are addressed simultaneously, such as wireless power [13], locomotion [14, 15], localization [16, 17], control

robustness [18], and biocompatbility [19]. Consider, for example, a scenario where reaching a particular location proves challenging through conventional tethered methods (Fig. 12A) [20]. In this case, the UMR would be inserted in either fluid-filled lumen or soft tissue, allowing access to the whole human body by swimming through bodily fluids or drilling through tissue, or both. This is most practically done through a UMR designed with a chiral geometry (e.g., screw-shaped or helical body), which can be driven by homogeneous rotating magnetic fields [21, 22, 23, 24]. To achieve the objective of reaching its location, the UMR must effectively harness sufficient mechanical energy for its locomotion while contending with the dynamics of blood circulation. To reach the desired location in Fig. 12A, the UMR must be steered controllably at bifurcations and driven with optimal rate at which maximum propulsive thrust is achieved. This scheme requires that we localize the UMR, reconstruct its physical surroundings, and achieve an acceptable level of biocompatibility and control robustness using a robotic platform at a scale relevant for clinical use. Even then, the true capabilities of these devices can only be conclusively demonstrated through *ex vivo* and *in vivo* experimental results. This is due to the complex interplay of multiple physical effects (such as the wall effect, blood flow, vessel bifurcations, and magnetohydrodynamic coupling), which cannot be accurately replicated *in vitro*.

Here we translate UMRs into *ex vivo* trials and achieve directional control inside a porcine aorta model with varying blood vessel diameter. Figs. 12B and 12C show the planned path of the UMR and the arterial blood flow, respectively. This planned trajectory ensures that the UMR navigates both against and along arterial flow, progressing toward the distal end of the renal artery, with validation performed using CBCT scans. To achieve this level of control, we assess the UMR's swimming behavior in a porcine aorta model in a clinical setting (Figs. 13A and 13B) by using wireless actuation and localization systems that can be effectively scaled up (Figs. 13C-13F). Initially, we undertake the design and characterization of UMRs that possess the ability to navigate through the whole porcine aorta model. The magnetic behavior of these UMRs in response to an external actuating magnetic field is assessed through an *in vitro* blood vessel model. Notably, only extended-duration characterization experiments are conducted *in vitro*. The predictions for optimal actuation inputs—specifically, actuation frequency and magnetic field strength—are made using ultrasound images and are correlated with the fluid properties. Subsequently, with these calculated inputs, we successfully showcase that UMRs are capable of controlled movement within confined spaces. This controlled movement enables the UMRs to navigate the interior of blood vessels in the porcine aorta model while minimizing contact with the vessel walls (Figs. 13G and 13H). In order to assure hemocompatibility of the UMRs a lipid-based coating was applied and various assay were carried out to verify this hemocompatibility. Fig. 13I shows micrographs of coated UMR material after incubation with fluorescently-labeled fibrinogen. Fibrinogen adsorption on the coated samples is reduced by 95% compared to the uncoated samples. Fig. 13J shows micrograph images of biofilms formed by *Staphylococcus aureus* on coated and uncoated samples, with a reduction of more than 99%. Fig. 13K compares the fibrin generation in time, of platelet-poor plasma in contact with coated versus uncoated samples. Fibrin generation was delayed by > 6 min for the coated samples compared to the uncoated samples. Together with further assays (see Section 4.2) the data indicates that no detrimental effect of coated UMRs is expected during *in vivo* applications.

4.1 *Ex vivo* model and robotic platform

4.1.1 Renal artery perfusion model

Porcine retroperitoneal organs, including the abdominal aorta and kidneys, along with blood, were procured from a slaughterhouse. Following the standard practice for meat processing, the pigs (*Sus scrofa domesticus*, the Netherlands) were rendered unconscious with an electric current applied through electrodes on the body. Subsequently, the carotid artery was incised to drain the animals of blood. The collected blood was directly obtained from the carotid artery wound

and placed in a plastic container prepped with 1000 IE heparin per liter of blood (Leo Pharma, Ballerup, Denmark). A total of ten liters of blood was collected from multiple pigs for a single experiment. The retroperitoneal organs, including the aorta and kidneys along with attached soft tissues, were excised and immediately placed in a plastic bag on ice for transport to the operating room (OR). During transport, the blood was kept at room temperature.

In the OR, the abdominal aorta, renal vessels, and kidneys were isolated. All aortic side branches, except the renal arteries, were ligated. A standard roller pump perfusion system employing a disposable set of tubing for extracorporeal organ perfusion was utilized. An overflow-secured reservoir was interposed between the pump and the aorta. The system was primed with the heparinized blood. The aorta, with the attached kidneys, was positioned on a plastic sheet and connected to the pump perfusion system by cannulating the proximal and distal ends of the aorta, to allow flow from the proximal end towards the distal end. Both renal arteries were also cannulated and linked to the pump perfusion system to ensure flow towards the kidneys within both renal arteries, while minimizing blood loss through the renal veins. The blood flow was measured at the proximal end to allow experiments at varying flow rates [25].

4.1.2 Untethered magnetic robot design and fabrication

The UMRs were designed using 3D computer-aided design software (SolidWorks, Dassault Systèmes, SolidWorks Corp. Inc., USA). The design consists of two identical halves which are joint together while enclosing a permanent magnet. The design finds it origin in previous research where they demonstrated blood clot removal [26]. The length and diameter of the UMRs are based on the inner diameters of the abdominal artery and renal artery respectively.

The UMRs were produced through Masked Stereolithography Apparatus (MSLA) employing a 3D printer (Phrozen Sonic Mini 4K). Phrozen Aqua-Gray 4K resin was the chosen material. During printing, a single layer height of 50 µm was utilized. Subsequent to printing, the components underwent cleaning with isopropyl alcohol (IPA) in an ultrasonic bath for a duration of 7 minutes. Post-curing was carried out using an Elegoo Mercury plus curing station for a duration of 12 minutes. After curing, UMRs were coated with LipoCoat 4AC coating technology by manual dipcoating for 10 s. Coated UMRs were, then, left to dry overnight under ambient conditions in the dark.

UMRs, possessing a minimum length (L) and diameter 9 mm and 3.75 mm respectively, were constructed by assembling a 3D-printed screw-shaped body with an enclosed permanent magnet composed of NdBFe Grade-N45 material (S-01-01-N Supermagnete, Gottmadingen, Germany). The permanent magnet is cylindrical with axial magnetization, measuring 1 mm in diameter and 1 mm in length, with a magnetic moment (m) of 8.4×10^{-4} A·m^2. The permanent magnet was positioned such that its magnetic moment was perpendicular to the long axis of the screw-shaped body. This configuration enabled the UMR to swim within blood upon rotation and follow an external weak-strength magnetic field of 5 mT.

4.1.3 Untethered magnetic robot performance evaluation

Leveraging the detailed understanding of the aorta's anatomy and physiology, we are able to evaluate the swimming capabilities of the UMRs. By conducting straight runs within the abdominal aorta, we can observe the UMRs' swimming behavior both against and with the blood flow. Additionally, the setting of the renal aortic side-branch offers a suitable environment for assessing the UMRs' ability to achieve directional control (Figs. 12B and 12C). The proximal and distal ends of the abdominal aorta are connected to a peristaltic pump for blood circulation at controlled pulsatile flow rate in the $15 \leq \dot{Q} \leq 260$ mL/min range. The average flow rate inside the abdominal aorta is 2.9 L/min [27], presenting a significant challenge for the UMR. However, enhancing the UMR's propulsive thrust is feasible by increasing its magnetic moment and strengthening the external magnetic field. Constructed with a screw-shaped body made

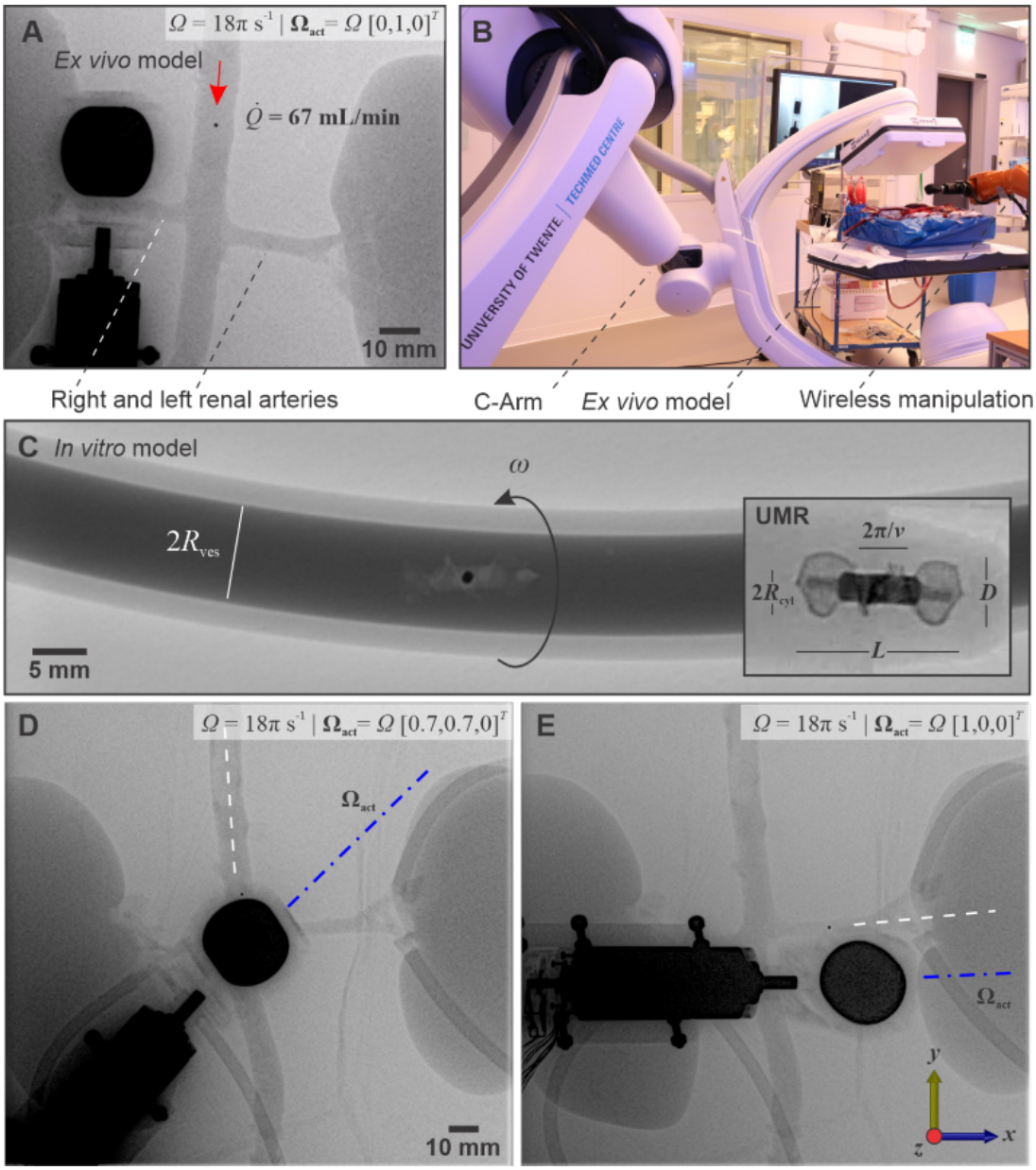

Fig. 14: *Untethered magnetic robots (UMRs) are employed to navigate vascular pathways for interventions. (A) X-Ray Fluoroscopy images are gathered online to detect the UMR, the rotating permanent magnet (RPM)-actuator, and the physical surroundings using clinically relevant radiation settings. (B) Our robotic platform consists of a C-Arm imaging and permanent magnet robotic systems. (C) To show the shape of the UMR, a radiocontrast agent is injected into an* in vitro *model. (D)-(E) The process of steering and maneuvering the UMR within the left renal artery is achieved by manipulating the rotation axis of the RPM about the* $\boldsymbol{z}$*-axis.*

through additive techniques, the UMR incorporates a fixed permanent magnet. Augmenting the proportion of ferromagnetic material is anticipated to refine its flow response, enabling greater magnetic torque under a given magnetic field, while concurrently reducing buoyancy. Although the physiological flow rate surpasses the range simulated in our *ex vivo* model, a UMR deployed for targeted blood flow restoration due to blockage is unlikely to encounter such high flow rates in practice.

Through the addition of a lipid-based coating, the UMR can attain self-sufficiency and maintain cellular viability [28]. The lipid-based coating has been shown to be highly hemocompatible, activating neither of the clotting pathways nor the complement system (see Section 4.2

and Fig. S2). Because of the miniature permanent magnet, we avoid the need to create strong magnetizing fields. The UMR is inserted into the model from the proximal end of the abdominal aorta through a large bore cannula (Fig. 13A). An intra-aortic 3D printed filter is connected to the distal end of the aorta (Fig. 13B) to retain the UMR when the applied blood flow is much greater than its propulsive thrust, or when the UMR is not magnetically coupled with the RPM actuator, temporarily. The *ex vivo* model and the RPM-actuator are placed between an X-ray source and a detector, as shown in Figs. 13C-13F. As the X-ray beam traverses through the model, the affixed UMR magnet, and the RPM-actuator, its intensity is diminished. This attenuation occurs as the X-ray travels from the source to the detector array. The acquired CBCT scan data enables us to reconstruct the internal structure of the model in 3 dimensions with precision, as shown in Figs. 12B and 12C, which would be useful in examining the positioning accuracy after actuation.

In contrast, X-ray Fluoroscopy images are gathered online with good resolution and at adequate frame rate (5 frames per second) for direct teleoperation, allowing the UMR to swim controllably under the influence of external inputs given directly by a clinician. Fig. 14A shows an X-ray Fluoroscopy image during a straight-run inside the abdominal aorta. A rotating magnetic field gradient is generated by the RPM-actuator, which is directly teleoperated based on the gathered X-ray Fluoroscopy images, similar to Section 2. Our robotic platform (i.e., C-Arm and wireless manipulation system) is configured such that the UMR, its physical surroundings, and the RPM-actuator are captured in each X-ray Fluoroscopy image, as shown in Fig. 14A. This is accomplished by using an oblique angle for the X-ray source and the detector array (Fig. 14B). The source and the detector of the C-Arm imaging system are kept at an oblique angle of 20° with the z-axis (in the frame of reference in Fig. 14). This setup enables the captured X-ray Fluoroscopy images to clearly display both the UMR and the RPM-actuator, thereby enhancing the intuitiveness of teleoperation. Furthermore, the oblique orientation of the C-Arm offers the RPM-actuator an expanded workspace, minimizing the potential for interference with the detector array. Fig. 14C illustrates the UMR's geometry, achieved by introducing a radiocontrast agent into an *in vitro* model, enhancing the visibility of the radiolucent structure.

Fig. 14A shows the configuration of the RPM-actuator and the position of the UMR during a straight-run against arterial flow. In this case, the RPM rotation axis, $\boldsymbol{\Omega}_{\text{act}}$, is oriented parallel to the centerline of the abdominal aorta and its translational velocity is controlled such that it remains in sync with the UMR. Under clinically relevant radiation doses, the low contrast resolution allows for a detectable signal from the attached radiopaque magnet. Consequently, only the magnet of the UMR becomes visible in the X-ray Fluoroscopy images in Figs. 14A, 14D, and 14E. Although controlling the UMR is challenging without orientation information at this radiation level (Fluoroscopy dose rate of: 0.35 $\text{mGy}\cdot\text{cm}^2\text{s}^{-1}$), the magnetic torque would ultimately allow the UMR to align with the RPM rotation axis. This is the method used in Fig. 14D to steer the UMR and enter the left renal artery, as shown in Fig. 14E. Additionally, it is worth noting that the orientation of the UMR can be determined by incorporating radiopaque markers into it or by utilizing a permanent magnet with a nonuniform aspect ratio, enabling orientation detection.

4.2 Hemobiocompatibility of untethered magnetic robots

Previously, we have shown that cell adhesion, cell morphology, focal adhesion formation, cell proliferation, and cell differentiation potential remain unaffected by the coating components [29]. Here, we investigate biocompatibility *in vitro* in terms of protein fouling, biofilm formation, and various hemocompatibility assays. These tests are conducted using coated UMR- and other materials. It is well-established that the initial step of the surface-activated (intrinsic) pathway of the clotting cascade involves the interaction of a protein (factor XII) with a foreign substrate. Similarly, the complement system is activated through protein interactions [30]. Hence, the affinity of proteins for a material is believed to be a significant determinant of a material's

hemocompatibility [31]. To evaluate this critical protein-material affinity, fibrinogen (clotting Factor I) is selected for use in a protein fouling assay. Microscopy of coated UMR material after incubation with fluorescently-labeled fibrinogen revealed a 95% reduction in protein adsorption compared to uncoated UMR material (Fig. 13I). This reduction in protein fouling is expected to diminish the activation of the clotting cascade and complement system during *in vivo* use.

Bacterial infections pose a significant and prevalent risk when using medical devices [32]. Bacteria that adhere to medical devices often lead to severe complications and can contribute to the formation of biofilms, which are challenging to treat and can promote antibiotic resistance[33]. Therefore, we conducted an assessment to inhibit bacterial attachment and subsequent biofilm formation on coated samples, initially focusing on attachment. attachment. In this regard, both coated and uncoated PU catheter materials were exposed to *Staphylococcus aureus* for 3 days, followed by washing, staining with propidium iodide, and imaging using a fluorescence microscope. The results indicated that the coated samples exhibited a reduction of over 99% in attached bacteria compared to the uncoated samples. This underscores the potential of using coated UMRs to reduce the risk of infection when compared to their uncoated counterparts. In the case of short dwell time UMRs, the primary infection risk appears to stem from bacterial introduction during insertion, rather than supporting biofilm formation.

Another common hemocompatibility assay is the fibrin generation test [34, 35]. It is routinely used to assess the formation of fibrin fibres, which, together with platelets, constitute the final stage of the clotting cascade, the blood clot. For the independent assessment of the intrinsic pathway, fibrin formation was tested using platelet poor plasma (PPP) isolated from freshly drawn, citrated whole-blood. Coated and uncoated UMR material was immersed in citrated PPP and, subsequently, the clotting cascade was re-initiated by reconstituting Ca^{2+} to physiological levels. The clotting cascade eventually leads to the formation of fibrin fibres, which causes a sudden increase in light scattering. The scatter signal at 405 nm is monitored in time, starting immediately after initiation. A sharp increase in the scatter signal, denotes the start of fibrin generation and can be accelerated by materials incompatible with the in vivo environment. Comparing coated with uncoated UMR material, a maximum of 6 min delay in fibrin formation was observed for the coated material. Thus, the coated material clearly delays the clotting via the intrinsic pathway and, therefore, coated UMRs are expected to carry a reduced embolic risk *in vivo* compared to uncoated UMRs.

LipoCoat 4AC coated PU catheter material was subjected to a variety of hemocompatibility tests carried out by a company dedicated to hemocompatibility testing of blood contacting devices, HAEMOSCAN BV. Standard hematology tests were carried out, consisting of platelet and red blood cell counts as well as quantification of hemobglobin and material-induced hemolysis. Thrombus tests included, visual and gravimetric assessment of thrombi formed on the samples, quantification via immunostaining of fibrin adsorbed to the samples and enzymatic quantification of attached platelets. Platelet activation was tested by quantifying released thromboxane B2 and beta thromboglobulin as well as platelet aggregation. Coagulation tests consisted of the quantification of thrombin-antithrombin III complex and fibrinopeptide A. Inflammation and complement activation were assessed by quantifying complement component fragments C3a-desArg and C5b-9 as well as elastase. The coated samples passed all hemocompatibility tests at levels comparable if not better than the negative control. The entirety of the data discussed above indicates coated samples to be highly hemocompatible and to expect no issues with regard to coagulation nor complement activation during *in vivo* use.

4.3 *In vitro* and *ex vivo* wireless locomotion of untethered magnetic robots

4.3.1 Fluidic and structural effects

The UMR is a screw-shaped rigid body with a length of L, a diameter of D, and an average magnetic moment $\mathbf{m}$ oriented perpendicular to its long axis. Fluid velocity, vessel walls, and

fluid flow within the vessels influence the velocity of the UMR. The body is mathematically represented as a helical wave superimposed onto a cylinder with a radius of R_{cyl}, and its surface is described by:

$$\mathbf{x}(\theta,\zeta) = \rho(\theta)\left[\cos(\nu^*\zeta+\theta)\hat{\mathbf{x}} + \sin(\nu^*\zeta+\theta)\right]\hat{\mathbf{y}} + \zeta\hat{\mathbf{z}}, \tag{5}$$

where $\theta \in [0, 2\pi)$ and $\zeta \in (-\infty, \infty)$ are helical coordinates and the function $\rho(\theta) = R_{\mathrm{cyl}}[1 + \epsilon f(N\theta)]$ describes the profile of the cross-section of the screw-shaped body, and $f(N\theta) = \sin(N\theta)$ is a periodic function, N and ϵ are the number and the amplitude of starts of the screw. When the UMR submerged in blood is subject to an external magnetic torque, $\mathbf{T} = \mathbf{m} \times \mathbf{B}$, it will move with velocity U and angular rotational rate, ω, satisfying

$$U = 2R_{\mathrm{cyl}}\omega\varepsilon^2 \sum_{q\geq 1} \frac{(1+\beta q^2 De^2) \mid \hat{f}_q \mid^2}{1+q^2De^2} J_q, \tag{6}$$

where $De = \tau\omega$ is the Deborah number, τ is the fluid relaxation timescale, and $\beta = \eta_{\mathrm{s}}/\eta$ is a ratio of the blood serum viscosity to the total viscosity of blood [36, 37]. The fluid relaxation timescale is estimated from oscillatory shear experiments as

$$\tau = \lim_{\omega\to 0} \frac{G'}{\omega G''}. \tag{7}$$

Here the real and imaginary parts of the complex elastic modulus denoted as G' and G'', respectively. In the case of blood, the Deborah number is typically $De = 0.1$ [38]. The viscosity of blood serum is approximately $1.4 - 1.5$ mPa·s, resulting in a value of $\beta = 0.43$ for blood and $\beta = 0.0015$ for blood clot.

The determination of translational velocity for UMRs within vessels of radius R_{ves} is carried out by distributing Stokeslet points on both the screw-shaped rigid body and the cylindrical vessel surface [39]. Stokeslet points on the screw-shaped rigid body are positioned according to Equation 5 for a total of two turns. These points on the UMR surface possess a velocity of $v(\theta,\zeta) = \omega \times x + U_N$. Meanwhile, the Stokeslet points on the vessel surface remain at a zero velocity. Subsequently, forces acting on the Stokeslet points are computed, ultimately leading to the determination of the total force acting on the UMR. The translational velocity along the capillary is adjusted until the net force on the UMR reaches zero. This velocity is then determined for various wavenumbers ν^* and cylinder-to-vessel ratio $R_{\mathrm{cyl}}/R_{\mathrm{ves}}$. The utilized UMRs have an ϵ value of 0.33 and a normalized wavenumber of $\nu = R_{\mathrm{cyl}}\nu^* = 2.2$. The $R_{\mathrm{cyl}}/R_{\mathrm{ves}}$ ratio varies with specific UMR applications: The ratio is 0.42 for large UMRs within the aorta, 0.75 for large UMRs in arteries, 0.32 for small UMRs within the aorta, and 0.56 for small UMRs in arteries.

When the UMR moves through a vessel with a flow rate, a plug flow relation is assumed, denoted as $\dot{Q} = \pi R_{\mathrm{ves}}^2 U_{\mathrm{f}}$, between the flow rate $\dot{Q}$ and the fluid flow velocity U_{f}. The UMR's velocity with the flow is given by $U_{\mathrm{w}} = U + U_{\mathrm{f}} - cU_{\mathrm{w}}$, and against the flow, it is $U_{\mathrm{a}} = U - U_{\mathrm{f}} - cU_{\mathrm{a}}$. Here, U represents the UMR velocity in the absence of flow, cU accounts for the friction between the UMR and the vessel wall, and c is the friction coefficient. The friction coefficient c and velocity U can be determined as follows: c is calculated as $c = (2U_{\mathrm{f}}/(U_{\mathrm{w}} - U_{\mathrm{a}})) - 1$, and U is determined as $U = (c+1)(U_{\mathrm{w}} + U_{\mathrm{a}})/2$.

The rheology measurements of our blood indicate viscosities of 27 mPa.s and 15 mPa.s at room temperature (25°C) and body temperature (37°C), respectively, for a shear rate of 2π 1/s. Consequently, the Reynolds number of the 9-mm-long UMR is 0.53 and 0.95 at room and body temperature, respectively, under the influence of an actuating field of 1 Hz. At an actuation frequency of 9 Hz, the Reynolds number increases to 4.2 and 7.6 for room and body temperature, respectively. For the 12-mm-long UMR, the Reynolds number is 0.71 and 1.3 at room and body temperature, respectively, under the influence of an actuation frequency of 1 Hz. With an actuation frequency of 9 Hz, the Reynolds number increases to 8.4 and 15.3 at room and body temperature, respectively.

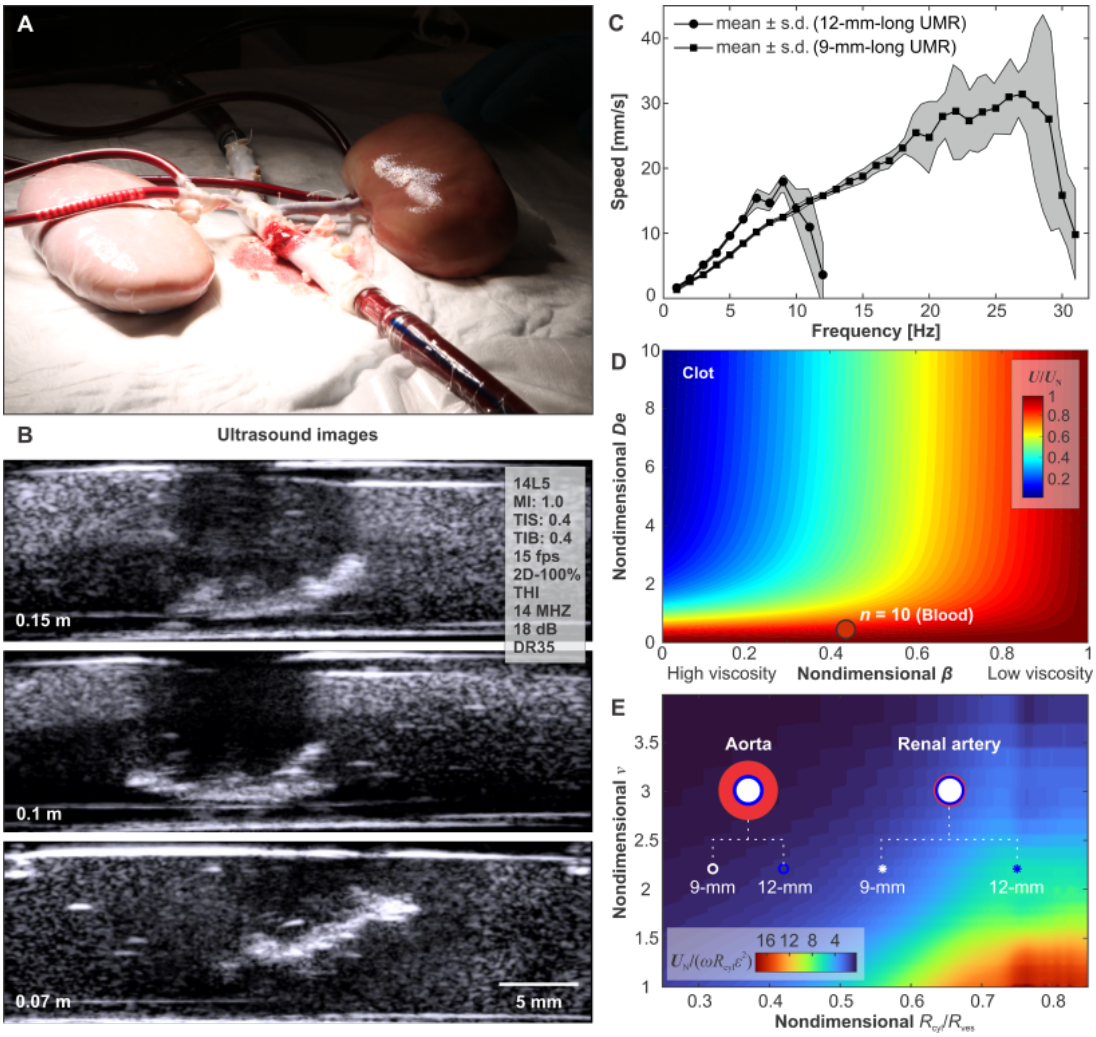

Fig. 15: *The movement of the untethred magnetic robot (UMR) is influenced by several factors, including the constraints imposed by the* ex vivo *model's confinement, the viscosity of the blood, and the external control inputs applied. (A)-(B) The actuation of the UMR is evaluated by utilizing ultrasound images to identify an optimal gap between the rotating permanent magnet (RPM) and the UMR. This gap is determined to achieve enough RPM clearance while minimizing contact with the inner wall of the lumen. (C) Frequency response of the UMR is characterized in blood. (D) Prediction of swimming speed of a UMR in blood and through a clot. The speed of the UMR, U, is normalized with swimming speed, U_{N}, in a Newtonian fluid (water). De and β are the Deborah number and ratio of serum to blood viscosity, respectively. (E) The UMR's swimming speed is influenced by the normalized wavenumber $\nu = \nu^* R_{\mathrm{cyl}}$ and diameter of the surrounding vessel ($2R_{\mathrm{ves}}$). The white and blue markers indicate the small and large UMRs used in this chapter, which share the same normalized helical pitch ($2\pi/\nu$) but differ in their ratios of $R_{\mathrm{cyl}}/R_{\mathrm{ves}}$.*

4.3.2 *In vitro* tissue and vessel phantom

We conducted prolonged experiments, including characterizing the frequency response in blood, using an *in vitro* tissue and vessel phantom. Developing the phantom (275 mm×85 mm×40 mm) involved employing a three-piece mold. Initially, the muscle edge layer was positioned on the base plate, and within the muscle edge, vessels (artery: Rehau Silicone 3/8" × 3/32"; vein: Rehau Silicone 3/16" × 1/16") and a femoral nerve (silicone round cord: Ø5 mm), each measuring 350 mm in length, were inserted. To mimic the femoral sheath, an interfacing tissue (80×50 mm) was enveloped around the vein and artery, temporarily secured using a paperclip. Following exposure to a heat gun, the paperclip could be detached, allowing the overlapping sides of the tissue to rotate downwards. Mimicking muscle tissue required preparing Ecoflex$^{\mathrm{TM}}$ 00-30 with

Silc Pig^{TM} Blood pigment, utilizing a WASSERMAN Wamix Touch vacuum mixer. After the curing process, the fat edge layer was added on top of the preceding edge. To mimic fat tissue, Soma Foama^{TM} 15 silicone with Silc Pig^{TM} blood and Silc Pig^{TM} white pigment was prepared using a hand mixer. Following another curing step, the skin edge layer was superimposed onto the previous edge. Subsequently, to replicate skin tissue, Ecoflex^{TM} 00-30 with Silc Pig^{TM} flesh tone was prepared using a WASSERMAN Wamix Touch vacuum mixer. Upon completing the final curing period, the entire mold was extracted.

The frequency response of the UMRs in blood was determined by assessing the swimming speed using ultrasound images, Fig. 15B. For this purpose, the UMRs were placed within the vessel of the *in vitro* phantom model, characterized by a diameter of 9.5 mm. A 14L5 ultrasound transducer was securely positioned beneath the phantom model, emitting ultrasound waves at a frequency of 11 MHz. A series of consecutive straight runs of the UMR were conducted ($n = 6$) for each actuation frequency of the RPM. The shading displayed in Fig. 15C illustrates the standard deviation (s.d.) in the results.

4.3.3 Wireless locomotion of untethered magnetic robots in arterial flow

The movement of screw-shaped UMRs within low-Re (in the range between 0.5 to 20) blood flow depends on three significant physical phenomena. The initial effect involves drag anisotropy, crucial for generating a net propulsive thrust through lateral movement or rotation around the long axis of the UMR. This characteristic is attained through the screw-shaped configuration of the body. In this case, the helical pitch, $2\pi/\nu$, is a crucial design feature which can be optimized to yield sufficient thrust. The second effect is the impact of the lumen wall. This wall effect becomes significant within restricted spaces and is anticipated to increase the swimming speed for a given helical pitch of the UMR. However, within confinement, the swimming speed demonstrates an increase up to a local maximum and subsequently declines to a local minimum as the helical pitch decreases [36]. As a result, when encountering blood vessel diameters of different sizes, the interplay between drag anisotropy and confinement effects would lead to fluctuations in the UMR's swimming speed as it advances. The third physical phenomenon is the magnetic interaction between the RPM-actuator and the UMR. When UMRs are directed to navigate toward a specific vessel, such as selecting one of three pathways at a bifurcation in the model, it involves controlling the plane of rotation of the magnetic field through the rotation axis of the RPM. A periodic torque about the long axis of the UMR drives the time-averaged propulsion, while another torque in-plane (within the $\boldsymbol{xy}$-plane about the $\boldsymbol{z}$-axis) is responsible for steering. Note that the *ex vivo* model is naturally constrained to lie on the horizontal plane (Fig. 15A), and therefore only these torques are sufficient to navigate and target any location of interest. Taking these effects into consideration results in a managed reaction of the UMR within the vessels. However, accessing the renal artery could remain challenging if the alignment between the UMR's long axis and the local tangent at the entry point of the centerline is not precise. In such cases, only UMRs with dimensions slightly smaller than those of the abdominal aorta and renal artery might have the potential to reach specific points of interest.

The distance between the UMR's long axis and the blood vessel's centerline varies with the UMR-RPM gap. Adjusting the UMR-RPM gap is achievable by moving the RPM closer to the vessel, which in turn influences the UMR's proximity to the vessel's centerline. Fig. 15B illustrates the influence of this gap on a UMR inside porcine blood, visualized using ultrasound images. The average *in vivo* gap from the abdominal aorta to the skin is approximately 10 cm to 12 cm. Therefore, this UMR-RPM gap is limited to approximately 0.1 m, generating a sufficient magnetic field to propel the UMR. Alternatively, further reducing the UMR-RPM gap can enhance the applied field in other parts of the body where blood vessels are more superficial. This control input becomes particularly valuable when managing a UMR at the onset of step-out (i.e., the frequency beyond which the UMR cannot keep pace with the actuating field). By moving the RPM-actuator closer to the vessel, the step-out frequency in such cases can be

elevated. The step-out frequency of two UMRs (9-mm- and 12-mm-long) is shown in Fig. 15C, for an RPM-UMR gap of 0.1 m. Associated with the increase in the actuation frequency of the RPM is a linear increase in the swimming speed of the UMR in blood, U, and similar response is observed in water U_{N}. Slightly below step-out (i.e., 10 Hz), the swimming speed of the 12-mm-long UMR is greater than that of any other actuation frequency, making it favorable for actuation. In contrast, the 9-mm-long UMR boasts a wider frequency range and can be actuated at frequencies of up to 28 Hz. While reducing the gap between the UMRs and the RPM actuator may not practically enhance the step-out frequency due to physical constraints in this body region, increasing the magnetic moment using a stronger magnet is a feasible solution.

In contrast to swimming in water, the interaction between blood and UMR is not solely elastic, as depicted in Fig. 15D. In the case of blood with a specific ratio of serum viscosity to total viscosity denoted as β, the UMR's swimming speed diminishes with higher fluid relaxation, indicated by De. The application of the Oldroyd-B model, Section 4.3.1, offers predictions for the UMR's swimming speed across a spectrum of blood solvent viscosity ratios and relaxation values. If the viscosity of the blood were to increase to the point where β approaches zero, the resultant swimming speed would also tend toward zero. In a potential medical intervention scenario (as shown in Fig. 12A), a UMR might need to be moved toward a blood clot to reinstate local flow. In this instance, it is more instructive to predict its response using our model. Our UMR speeds, scaled by their speed in a Newtonian fluid (U/U_{N}), are noticeably slower in clots compared to their speeds in blood. Therefore, for our experiments, it suffices to demonstrate controlled locomotion toward a specific location of interest, and potentially facilitate the release of a drug to reinstate the flow.

Fig. 15E presents the projected UMR swimming speed as a function of the normalized wavenumber ν and cylinder-to-vessel ratio $R_{\mathrm{cyl}}/R_{\mathrm{ves}}$. Smaller normalized wavenumber values correspond to increased speed. Both the 9-mm-long UMR and the 12-mm-long UMR exhibit an average normalized wavenumber of approximately 2.2. In narrower vessels, there is an observed speed increase compared to wider vessels. Consequently, higher speeds are anticipated in the renal artery compared to the aorta. In the aorta, the small and large UMRs possess cylinder-to-vessel ratios of 0.32 and 0.42, resulting in predicted speeds of 6 mm/s and 12 mm/s, respectively. Conversely, in the renal artery, the small and large UMR feature cylinder-to-vessel ratios of 0.56 and 0.75, leading to predicated speeds of 18 mm/s and 74 mm/s, respectively. We compare the observed swimming speeds when the UMRs are allowed to move both against and with the blood flow. Straight runs of the UMR along the abdominal aorta of the *ex vivo* model are conducted at actuation frequencies below the step-out threshold, aiming to achieve maximum propulsive thrust. Fig. 16 illustrates the trajectory taken by the same 12-mm-long UMR during a straight run at actuation frequency of 9 Hz. In this trial, the run begins by propelling the UMR against the flow, originating from the distal end of the abdominal aorta and progressing toward its proximal end. As the UMR moves along its path, it encounters varying flow velocities. Notably, the blood flow speed past the bifurcation of the renal arteries exceeds that of any other parts of the *ex vivo* model. Consequently, at $t = 5$ s, a noticeable disparity in the UMR's trajectory emerges. The presence of the renal circulation leads to a reduction in blood flow past the bifurcation, and as the UMR advances beyond this location, it encounters greater arterial flow. Once the UMR reaches the renal bifurcation, its previously smooth trajectory transforms into a zigzag curve, resulting in increased lateral displacement and, on average, a decrease in swimming speed (Fig. 16A). Alternatively, when the UMR is allowed to swim with the flow (as indicated by the blue trajectories), its propulsive thrust aligns with the direction of the flow, resulting in more seamless swimming behavior, as shown in Fig. 16B. In Fig. 16C, the graph displays the measured distance between the UMR and the centerline of the aorta during this straight-run. The UMR exhibits greater lateral displacement when swimming against the flow, especially when it swims closer to the centerline of the aorta where the flow velocity is higher. On the other hand, when the motion is reversed and the UMR swims with the flow, it becomes

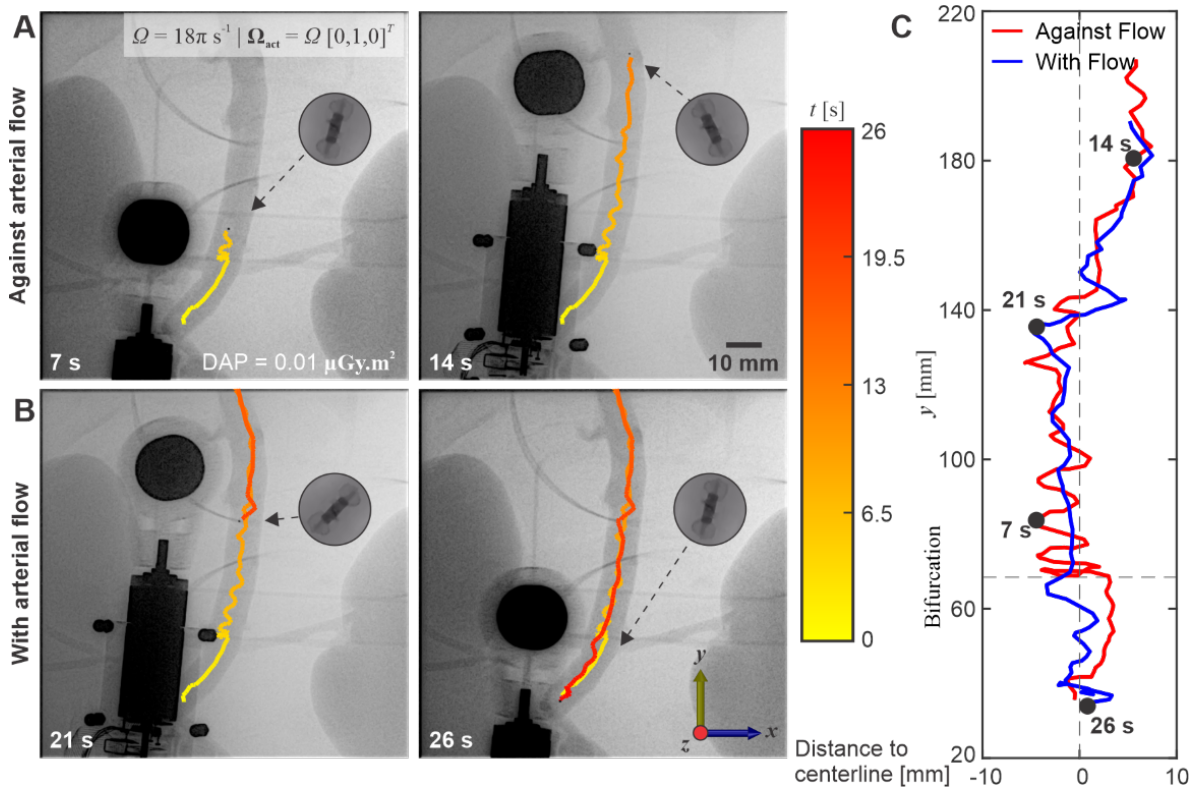

Fig. 16: *The untethered magnetic robot (UMR) is directed in a controlled manner both against and with the direction of arterial flow, maintaining movement below its step-out frequency. The UMR is actuated against (A) and with (B) arterial flow at actuation frequency of 9 Hz. (C) The UMR exhibits greater lateral displacement when swimming against the flow.*

more oriented toward the centerline due to the velocity gradient within the aorta.

We gradually increase the pulsatile blood flow and evaluate the straight-run performance of the UMRs both against and with the arterial flow, as shown in Fig. 17 The measured swimming speed of the UMR against the flow exhibits a seemingly linear trend, with the speed decreasing as the flow increases. At a flow rate of 67 mL/hr, the propulsive thrust proves adequate to counteract the flow, although resulting in a small net displacement. In contrast, swimming with the flow results in a speed increase, yet still demonstrates a qualitative correlation with blood flow. Although the average flow rate in the abdominal aorta is 2.9L/min [27], incorporating additional magnetic material can enhance the UMR's magnetic moment and step-out frequency. Alternatively, increasing the strength of the external magnetic field can improve propulsive thrust, especially when combined with field-gradient pulling. It's worth noting that UMRs deployed to target clogged vessels (Fig. 12A) are unlikely to encounter such high flow rates since the flow is obstructed.

A plug flow model aligns well with flow rates exceeding 15 mL/min, where the calculated speed, U, falls within the range of $16 - 19$ mm/s, under a 9 Hz actuation frequency of the UMR. This is in agreement with the frequency response depicted in Fig. 15C. Additionally, a friction factor ranging from $0.8 - 1.4$ for small UMR and 0.4 to 0.74 for large UMR estimates a reduction in the UMR's speed attributed to friction with the vessel wall (aorta). In the renal artery, the friction coefficient of the small UMR increased to 1.6 indicating a higher friction due to narrower vessel. The swimming speed with flow displays a trend that seems to be less responsive to variations in blood flow. With the UMR and the RPM magnetically interconnected, the field gradient will likely induce a pulling force in the opposite direction of the flow.

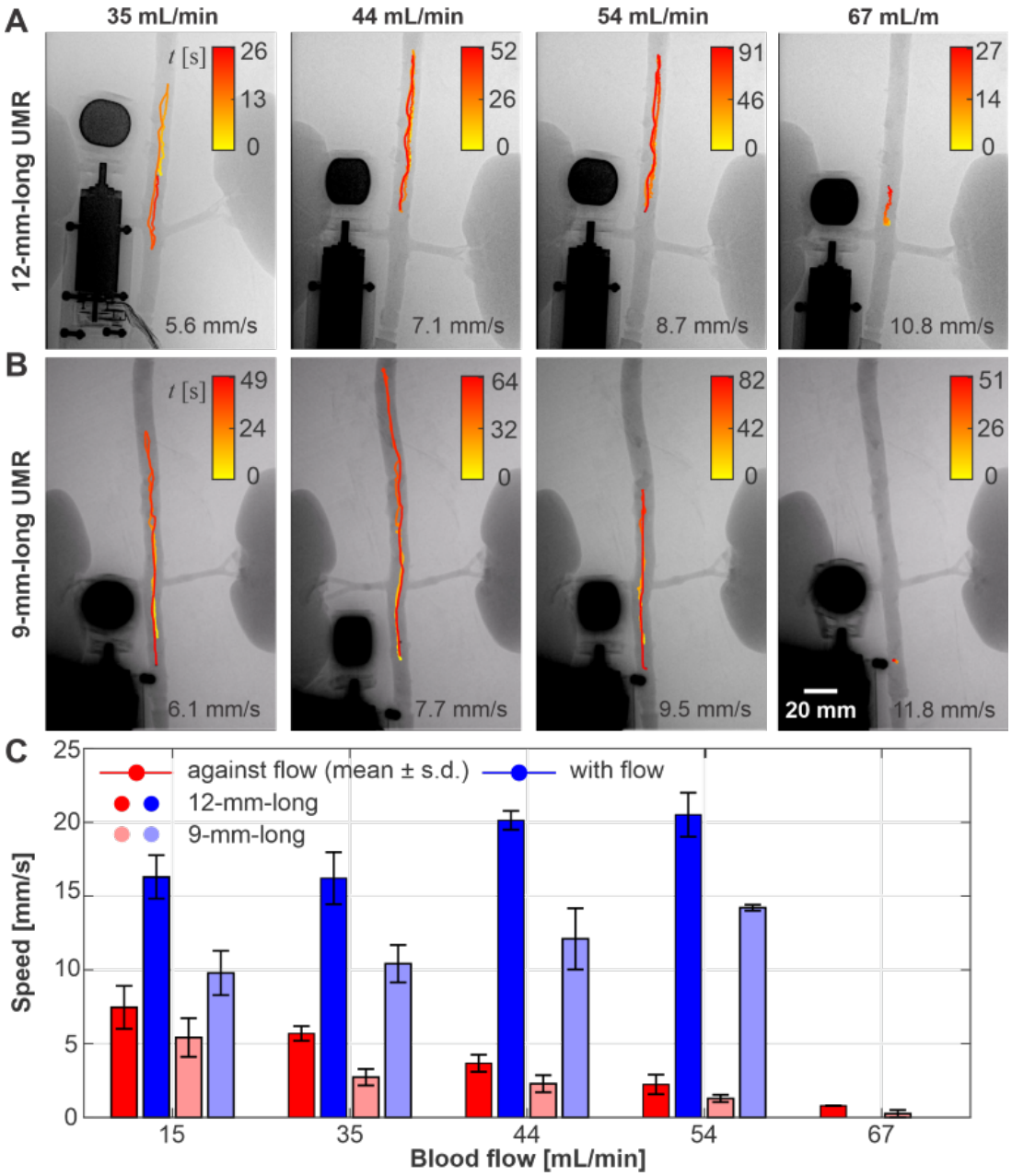

Fig. 17: *The swimming velocity of the untethered magnetic robots (UMRs) is assessed within the range of blood flow rates from 15 to 67 mL/min. (A)-(B) To achieve consecutive straight-runs at an actuation frequency of 9 Hz for each flow rate, the UMR is moved under controlled maneuver. The average speeds are determined based on data collected from five separate trials. (C) The robotic platform effectively maintains the UMR's position against the highest blood flow rate of 67 mL/min.*

4.3.4 Directional control and steering maneuver into the renal artery

Guided by the motion characteristics and theoretical model of the UMR, we control the UMR toward the LRA to showcase its navigational capabilities. Controlling the magnetic fields is achieved by employing a position-controlled RPM-actuator configured in a manner that enables direct teleoperation of its rotation axis, $\mathbf{\Omega}_{\text{act}}$, and position. Visual tracking of the UMR is facilitated through X-ray Fluoroscopy images captured at a fluoroscopy dose rate of 0.62 $\text{mGy}\cdot\text{cm}^2\text{s}^{-1}$. Radiation exposure is monitored throughout each trial, ensuring a reduction in the overall radiation dosage, leading to relatively low contrast resolution.

The UMR's passage into the LRA along renal flow is achieved through several stages: an

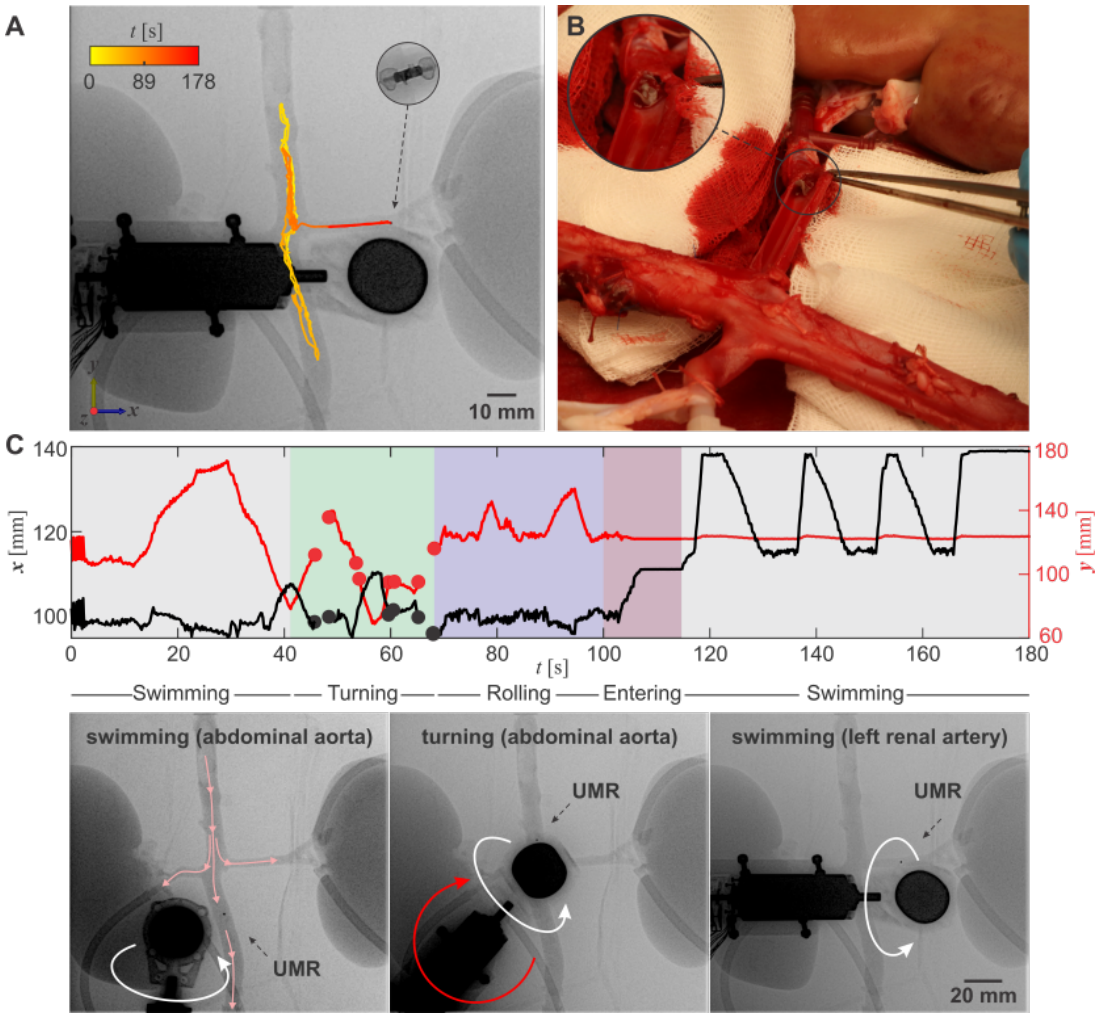

Fig. 18: *The untethered magnetic robot (UMR) is remotely operated to navigate through the abdominal aorta, engaging in a series of straight runs before executing a turning maneuver within the left renal artery. (A) The rotating permanent magnet (RPM)-actuator is teleoperated to exert in-plane torque required to steer the UMR toward the left renal artery. (B) The UMR is extracted from the left renal artery and no damage in the wall lining is observed. (C) A four-stage sequence is executed to transition the UMR from its location in the abdominal aorta to the renal artery. The small circles on the visual representation denote instances where the visual feedback of the UMR is obscured by the RPM-actuator. The black-dashed arrows indicate the position of the UMR and the pink arrows indicate the direction of blood flow. The white and red circular arrows indicate the direction of rotation of the RPM with respect to its rotation axis and the $\boldsymbol{z}$-axis, respectively.*

initial swimming maneuver toward the renal artery's bifurcation (aligned along the $\pm\boldsymbol{y}$-axis within the reference frame of Fig. 18A), a subsequent turning maneuver toward the entry point of the renal artery, followed by a rolling maneuver along the $\pm\boldsymbol{y}$-axis, and ultimately a swimming maneuver with the renal flow along the $\pm\boldsymbol{x}$-axis. This four-stage sequence is adopted due to the near right angle formed by the renal artery and the abdominal aorta, making a direct turn substantially challenging. Additionally, due to the inherent limitations of 2D X-ray Fluoroscopy image acquisition, accurately determining the UMR's depth within the abdominal aorta is unfeasible. This, in turn, hinders the ability to make precise adjustments to its height in relation to the entry point of the renal artery using out-of-plane pitch angle swimming.

Screw-shaped UMRs are adept at maneuvering and rolling in proximity to any wall. By rotating the UMR by 90° about the $\boldsymbol{z}$-axis, its long axis becomes perpendicular to the abdominal aorta and aligned with the left renal artery. Consequently, alternating rolling motions around

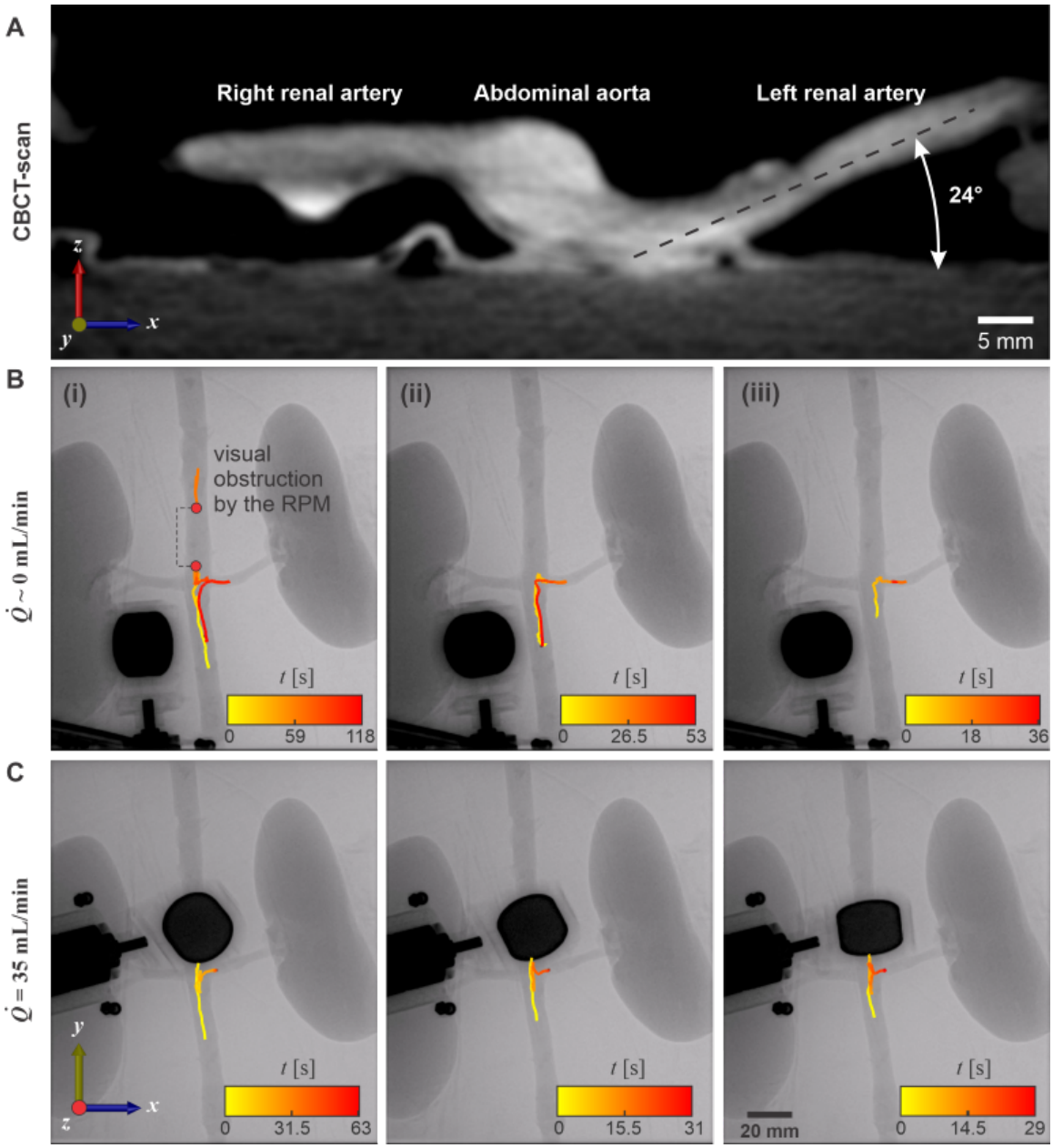

Fig. 19: *The 9-mm long untethered magnetic robot is controllably moved back and forth between the abdominal aorta and the proximal end of the left renal artery. (A) A CBCT scan shows the* $\boldsymbol{xz}$*-plane of the renal bifurcation. (B) Motion control is achieved in a stationary blood flow* ($\dot{Q} \sim 0$)*. (C) Motion control is achieved in blood flow of 35 mL/min.*

the entry point for roughly 30 seconds results in successful entry. This rolling is succeeded by swimming and sequential motion reversals within the renal artery. In this trial, teleoperation guides the UMR to the distal end of the LRA in less than 180 seconds. Furthermore, upon internal wall inspection, we observe no indications of damage (as depicted in Fig. 18B).

Fig. 18C depicts the sequence of teleoperated inputs that guide the UMR from the abdominal artery to the distal end of the left renal artery. Between $0 < t < 40$ seconds, the UMR initiates swimming against the blood flow along the $+\boldsymbol{y}$-axis, moving past the renal bifurcation. Around $t \sim 30$ seconds, the UMR's direction is reversed, and it is directed to swim again toward the renal bifurcation along the $-\boldsymbol{y}$-axis, following the flow. Upon passing the renal bifurcation, the swimming direction is reversed again and the RPM is gradually turned about the $\boldsymbol{z}$-axis to exert an in-plane torque, steering the UMR parallel to the renal artery. Multiple overlaps between

the RPM and the UMR obstruct visual feedback during this turning maneuver. This is clearly indicated by the small circles in Fig. 18C between $40 < t < 65$ seconds. Subsequently, the UMR is controlled to roll back and forth between $65 < t < 110$ seconds to enter the left renal artery, assisted by the renal flow.

Once inside the renal artery (around $t \sim 115$ seconds), the UMR swims toward its distal end at a faster speed than that in the abdominal artery. Similarly, when the swimming direction inside the renal artery is reversed (around $t \sim 125$ seconds) and the UMR swims back toward the entry point, its speed is exceeded by that against the arterial flow. This motion enhancement is attributed to the wall effect. With the smaller diameter inside the renal artery, the flow provides an extra force on the body, which increases the swimming speed along flow.

Fig. 19A presents a cross-section view of the renal bifurcation obtained through a CBCT scan. Clearly, the centerline of the abdominal aorta does not align with the horizontal planes of either the left or the right renal arteries. The LRA exhibits a 24° inclination with respect to the horizontal $\boldsymbol{xy}$-plane. Nevertheless, it remains feasible to guide the UMR toward the entry point of the LRA and subsequently return to the abdominal aorta. Fig. 19(B) shows three consecutive motion control trials directed toward the LRA under conditions of stationary blood flow. Throughout these trials, the operator effectively maintained synchronization between the UMR and the RPM, even when faced with temporary visual obstructions (Fig. 19B(i)). To mitigate such visual obstructions, adjusting the UMR's trajectory to enable a direct entry into the left renal artery, as demonstrated in Figs. 19B(ii) and 19B(iii), can prove to be a highly effective strategy. Direct turns like these are achievable under stationary fluid conditions or with very low flow rates. However, as the flow rate increases, executing a direct 90° turn becomes challenging. In such cases, we employ a combination of rolling and swimming to access the renal artery in less than 60 seconds, as demonstrated in three representative trials in Fig. 19C.

4.4 Conclusions

In this chapter, we demonstrate the feasibility of biocompatible UMRs, which are actuated by X-ray-guided magnetic fields. We conduct an in-depth analysis of the UMRs' response using magneto-hydrodynamic models, which serves as a basis for selecting design parameters and control inputs for motion control within an *ex vivo* porcine aorta model. For UMRs that display a small normalized wavenumber (large normalized helical pitch), the cylinder-to-vessel ratio significantly impacts their swimming speed. Conversely, as the normalized wavenumber increases, the influence of confinement diminishes. Based on these theoretical predictions, several design concepts can be proposed to address navigation challenges within varying blood-vessel diameters. The first design involves screw-shaped bodies with relatively small normalized helical pitch (large wavenumbers), resulting in slower locomotion but reduced sensitivity to the diameter of the confinement. A second design features screw-shaped bodies with relatively high helical pitches (small normalized wavenumber), which enhances swimming speed as the cylinder-to-vessel ratio increases, making them well-suited for narrower vessels. Our design blends the robustness of the first type in response to varying blood-vessel diameters with the propulsion enhancement anticipated with the low helical pitch and increasing cylinder-to-vessel ratio of the second type. With this level of control and based on our theoretical predictions, we demonstrate successful direct teleoperation of 9-mm-long UMRs within the abdominal aorta, advancing toward the distal end of the renal artery.

The swimming speeds of our UMRs demonstrate remarkable efficiency, comparable to tethered catheters. It is crucial to emphasize that in medical procedures, clinicians typically have control over the speed at which a catheter is advanced or withdrawn, allowing for adjustments as needed for the specific procedure. When scaled by their body length, our 12-mm-long and 9-mm-long UMRs achieve maximum swimming speeds of 1.6 and 3.3 body lengths per second below their step-out frequencies, respectively. The enhanced efficiency of the smaller UMR is mainly enabled by its reduced resistance to rotation, a characteristic that scales as R_{cyl}^2, resulting

in a swimming speed that increases linearly with rotational speed ω and R_{cyl}. This scaling effect highlights the advantages of smaller UMRs in achieving higher relative speeds, comparable to those achieved by tethered devices when controlled by clinicians. However, it is worth noting that catheters have the advantage of exerting much greater force, making them effective for engaging with, for example, thrombus. Currently, our UMRs efficiently harvest magnetic energy and transduce it entirely into work to reach the desired site. Achieving comparable engagements with thrombus as catheters may require significantly greater force. To enhance the frequency response and propulsive thrust of our UMRs, we can explore increasing their magnetic moment and enhancing the strength of the actuating field, which could further improve their performance in targeted applications.

References

[1] B. J. Nelson, I. K. Kaliakatsos, J. J. Abbott, "Microrobots for minimally invasive medicine," *Annual Review of Biomedical Engineering*, vol. 12, no. 1, pp. 55–85, 2010.

[2] M. Sitti, H. Ceylan, W. Hu, J. Giltinan, M. Turan, S. Yim, E. Diller, "Biomedical applications of untethered mobile milli/microrobots," *Proceedings of the IEEE*, vol. 103, no. 2, pp. 205-224, 2015.

[3] L. Ricotti, B. Trimmer, A. W. Feinberg, R. Raman, K. K. Parker, R. Bashir, M. Sitti, S. Martel, P. Dario, A. Menciassi, "Biohybrid actuators for robotics: A review of devices actuated by living cells," *Science Robotics*, vol. 2, no. 12, 2017.

[4] O. Felfoul, M. Mohammadi, S. Taherkhani, et al. "Magneto-aerotactic bacteria deliver drug-containing nanoliposomes to tumour hypoxic regions," *Nature Nanotechnology*,vol. 11, 941–947, 2016.

[5] T. Xu, J. Zhang, M. Salehizadeh, O. Onaizah, E. Diller, "Millimeter-scale flexible robots with programmable three-dimensional magnetization and motions," *Science Robotics*, vol. 4, 2019.

[6] M. Medina-Sánchez, L. Schwarz, A. K. Meyer, F. Hebenstreit, O. G. Schmidt, "Cellular cargo delivery: Toward assisted fertilization by sperm-carrying micromotors" *Nano Letters*, vol. 16, 1, 555–561, 2016.

[7] F. Rajabasadi, S. Moreno, K. Fichna, A. Aziz, D. Appelhans, O. G. Schmidt, M. Medina-Sánchez, "Multifunctional 4D-Printed sperm-hybrid microcarriers for assisted reproduction," *Advanced Materials*, vol. 34, no. 50, 2022.

[8] S. Martel and M. Mohammadi, "Using a swarm of self-propelled natural microrobots in the form of flagellated bacteria to perform complex microassembly tasks," in *IEEE International Conference on Robotics and Automation (ICRA)*, pp. 500–505, 2010.

[9] F. N. P. Basualdo, A. Bolopion, M. Gauthier, P. Lambert, "A microrobotic platform actuated by thermocapillary flows for manipulation at the air-water interface," *Science Robotics*, vol. 6, 2021.

[10] F. Carpi and C. Pappone, "Magnetic maneuvering of endoscopic capsules by means of a robotic navigation system," in *IEEE Transactions on Biomedical Engineering*, vol. 56, no. 5, pp. 1482-1490, 2009.

[11] S. Taherkhani, M. Mohammadi, J. Daoud, S. Martel, M. Tabrizian, "Covalent binding of nanoliposomes to the surface of magnetotactic bacteria for the synthesis of self-propelled therapeutic agents," *ACS Nano*, vol. 27, no. 8(5), pp. 5049-60, 2014.

[12] Q. Wang, J. Zhang, J. Yu, J. Lang, Z. Lyu, Y. Chen, L. Zhang, "Untethered small-scale machines for microrobotic manipulation: from individual and multiple to collective machines," *ACS Nano*, 2023.

[13] A. W. Mahoney and J. J. Abbott, "Generating rotating magnetic fields with a single permanent magnet for propulsion of untethered magnetic devices in a lumen," *IEEE Transactions on Robotics,* vol. 30, no. 2, pp. 411-420, 2014.

[14] R. Dreyfus, J. Baudry, M. L. Roper, M. Fermigier, H. A. Stone, J. Bibette, "Microscopic artificial swimmers," *Nature*, 437, 862-865, 2005.

[15] L. Zhang, J. J. Abbott, L. Dong, B. E. Kratochvil, D. Bell, B. J. Nelson, "Artificial bacterial flagella: fabrication and magnetic control," *Applied Physics Letters*, vol. 94, no. 6, pp. 064107, 2009.

[16] F. Bianchi, A. Masaracchia, E. S. Barjuei, A. Menciassi, A. Arezzo, A. Koulaouzidis, D. Stoyanov, P. Dario, G. Ciuti, "Localization strategies for robotic endoscopic capsules: a review," *Expert Review of Medical Devices*, vol. 16, no. 5, pp. 381-403, 2019.

[17] A. Aziz, S. Pane, V. Iacovacci, N. Koukourakis, J. Czarske, A. Menciassi, M. M. Sánchez, O. G. Schmidt, "Medical imaging of microrobots: Toward in vivo applications," *ACS Nano*, vol. 14, no. 9, pp. 10865-10893, 2020.

[18] J. Jiang, Z. Yang, A. Ferreira, L. Zhang, "Control and autonomy of microrobots: recent progress and perspective," *Advanced Intelligent Systems*, vol. 4, no. 5, 2022.

[19] X. Yan, Q. Zhou, M. Vincent, Y. Deng, J. Yu, J. Xu, T. Xu, T. Tang, L. Bian, Y.-X. J. Wang, K. Kostarelos, Li Zhang, "Multifunctional biohybrid magnetite microrobots for imaging-guided therapy," *Science Robotics*, vol. 2, no. 12, 2017.

[20] D. Jin, Q. Wang, K. F. Chan, N. Xia, H. Yang, Q. Wang, S. C. H. Yu, L. Zhang, "Swarming self-adhesive microgels enabled aneurysm on-demand embolization in physiological blood flow," *Science Advances*, vol. 9, no. 6, 2009.

[21] A. Ghosh and P. Fischer, "Controlled propulsion of artificial magnetic nanostructured propellers," *Nano Letters*, vol. 9, no. 6, 2009.

[22] X. Wang, X.-H. Qin, C. Hu, A. Terzopoulou, X.-Z. Chen, T.-Y. Huang, K. Maniura-Weber, S. Pané, Bradley J. Nelson, "3D Printed enzymatically biodegradable soft helical microswimmers," *Advanced Functional Materials*, vol. 28, no. 45, 2018.

[23] H. Ceylan, I. Ceren Yasa, O. Yasa, A. F. Tabak, J. Giltinan, M. Sitti, "3D-Printed biodegradable microswimmer for theranostic cargo delivery and release," *ACS Nano*, vol. 13, no. 3, 2019.

[24] A.C. Bakenecker, A. von Gladiss, H. Schwenke, et al. "Navigation of a magnetic micro-robot through a cerebral aneurysm phantom with magnetic particle imaging," *Scientific Reports*, vol. 11, no. 14082, 2021.

[25] J. Edwards, H. Abdou, N. Patel, M. H. Madurska, K. Poe, J. E. Bonin, M. J. Richmond, T. E. Rasmussen, J. J. Morrison, "The functional vascular anatomy of the swine for research," *Vascular*, vol. 30, no. 2, pp. 392-402, 2022.

[26] J. Leclerc, H. Zhao, D. Bao, A. T. Becker, "In Vitro design investigation of a rotating helical magnetic swimmer for combined 3D navigation and blood clot removal," *IEEE Transactions on Robotics*, vol. 36, no. 3, pp. 975-982, 2020.

[27] Taylor, C.A., Cheng, C.P., Espinosa, L.A. et al. In Vivo Quantification of Blood Flow and Wall Shear Stress in the Human Abdominal Aorta During Lower Limb Exercise. Annals of Biomedical Engineering 30, 402–408 (2002).

[28] G. Koçer and P. Jonkheijm, "About chemical strategies to fabricate cell-instructive biointerfaces with static and dynamic complexity," *Advanced Healthcare Materials*, vol. 7, pp. 1701192, 2018.

[29] G. Koçer and P. Jonkheijm, "Guiding hMSC adhesion and differentiation on supported lipid bilayers," *Advanced Healthcare Materials*, vol. 7, no. 3, 2017.

[30] P. Garred, J. Olsen, T. E. Mollnes, T. Bidle, B. E. Glahn, "Biocompatibility of urinary catheters. effect on complement Activation," *British Journal of Urology*, vol. 63, no. 4, 1989.

[31] W. van Oeveren, "Obstacles in Haemocompatibility Testing," *Scientifica*, vol. 2013, 2013.

[32] P. Eggimann, H. Sax, D. Pittet, "Catheter-related infections. Microbes and infection," *Microbes and Infection*, vol. 6, 2004.

[33] M. L. W. Knetsch and L. H. Koole, "New strategies in the development of antimicrobial coatings: The example of increasing usage of silver and silver nanoparticles," *Polymers*, vol. 3, 2011.

[34] F. A. W. Coumans, A. R. Brisson, E. I. Buzas, F. Dignat-George, E. E. E. Drees, S. El-Andaloussi, C. Emanueli, A. Gasecka, A. Hendrix, A. F. Hill, R. Lacroix, Y. Lee, T. G. van Leeuwen, N. Mackman, I. Mäger, J. P. Nolan, E. van der Pol, D. M. Pegtel, S. Sahoo, P. R. M. Siljander, G. Sturk, O. de Wever, R. Nieuwland, "Methodological guidelines to study extracellular vesicles," *Circulation Research*, vol. 120, 2017.

[35] M. Hellum, R. Øvstebø, A.-M. S. Trøseid, J. P. Berg, P. Brandtzaeg, C. E. Henriksson, "Microparticle-associated tissue factor activity measured with the Zymuphen MP-TF kit and the calibrated automated thrombogram assay," *Blood Coagul Fibrinolysis*, vol. 23, 2012.

[36] L. Li and S. E. Spagnolie, "Swimming and pumping by helical waves in viscous and viscoelastic fluids," *Physics of Fluids*, vol. 27, pp. 021902-1–021902-23, 2015.

[37] E. Lauga, "Propulsion in a viscoelastic fluid," *Physics of Fluids*, vol. 19, pp. 083104-1–083104-13, 2007.

[38] A. N. Beris, J. S. Horner, S. Jariwala, M. J. Armstrong, N. J. Wagner, "Recent advances in blood rheology: a review," *Soft Matter*, vol. 17, 2021.

[39] R. Cortez, L. Fauci, A. Medovikov, "The method of regularized Stokeslets in three dimensions: Analysis, validation, and application to helical swimming," *Physics of Fluids*, vol. 17, 2005.

5 X-Ray-Guided Robotic Platform for Remote Control of Untethered Magnetic Robots Targeting Blood Clots in the Iliac Artery

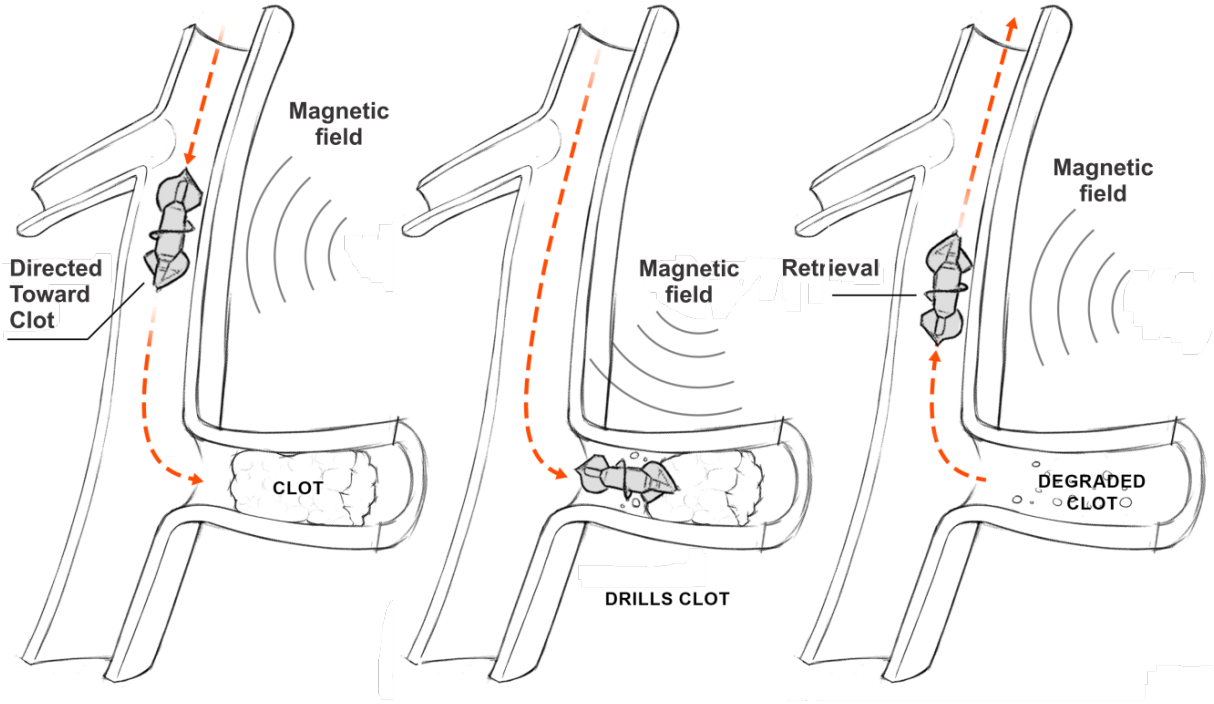

Fig. 20: *An untethered magnetic robot (UMR) is deployed within an* ex vivo *endovascular thrombosis model situated in the iliac artery, employing precise control through magnetic fields. The UMR is navigated toward the clot, facilitating engagement and subsequent reduction in size, before being directed back toward the insertion point for retrieval.*

In the healthcare landscape, where the emphasis on minimally-invasive surgery is pivotal, addressing the challenges posed by acute ischemic stroke and occlusions in deep-seated vessels is paramount due to their significant impact on global morbidity and mortality. The pressing need for inventive solutions has driven the exploration of integrating robotics and electromagnetics, as demonstrated by the promising potential of wireless manipulation systems in medical interventions [1]. These wireless manipulation systems enable the control of untethered devices at the millimeter or micrometer scale without a tether, making occlusions in deep-seated vessels accessible (Fig. 20). While these UMRs activated by RPMs have demonstrated effectiveness in controlled settings [2], their application in the dynamic conditions of *in vivo* scenarios remains challenging, requiring advancements to enhance their adaptability and functionality.

This chapter aims to bridge this gap by investigating the challenges associated with transitioning UMRs (i.e., screw-shaped body with an affixed permanent magnet) from artificial environments to realistic *ex vivo* scenarios, with a particular focus on targeting blood clots within the iliac artery. Employing an X-ray-guided robotic platform for precise control, Chapter 2, millimeter-sized UMRs are deployed to demonstrate their efficacy in engaging with blood clots and reinstating blood flow. Additionally, CBCT scans are employed for volume reconstruction of the clots at specific time points, revealing a volume reduction within 30 minutes—achieved without the use of thrombolytic agents. The outcomes presented herein not only contribute to the field of medical robotics but also hold promise for the development of minimally invasive procedures in the management of acute ischemic stroke and occlusions in deep-seated vessels. The rest of this chapter is structured as follows: Section 5.1 offers insights into the *ex vivo* endovascular thrombosis model and the the robotic platform (Fig. 21). Our teleoperation control

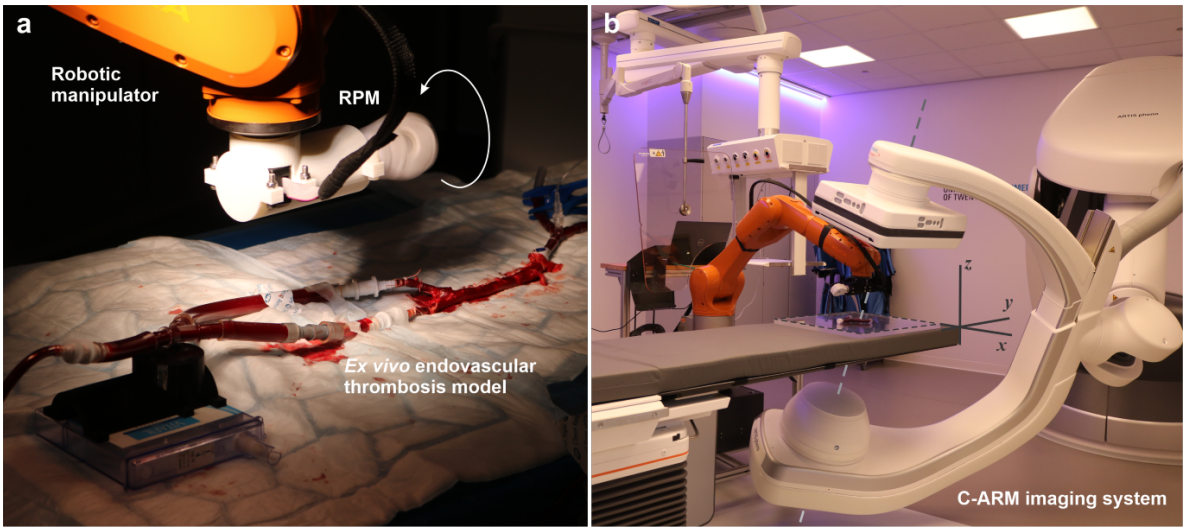

Fig. 21: *Accurate blood clot targeting is demonstrated in an* ex vivo *endovascular thrombosis model within the iliac artery. (a) The iliac artery, connected to a circulation pump, exhibits a blood clot confined by a diameter-reducing wire. (b) The robotic platform integrates a C-ARM imaging system and a wireless manipulation system, collaborating to achieve precise localization and wireless actuation. The untethered magnetic robot, situated within the iliac artery, is navigated using rotating magnetic fields.*

strategy and the hemobiocompatability of our UMRs are outlined in Section 5.2. The *ex vivo* targeting of blood clots is presented in Section 5.3. Finally, Section 5.4 provides conclusions and outlines directions for future research.

5.1 Occlusive thrombus model within an X-ray-guided robotic platform

Engaging with a blood clot in an *ex vivo* setting requires overcoming several hurdles. First, the clot must be effectively trapped inside the blood vessel and continuously monitored to determine its size over time. Second, the UMR must be deployed and teleoperated toward the clot, achieving a satisfactory reduction in clot size. The wireless manipulation and medical imaging systems employed for actuation and clot reconstruction, respectively, must be scalable to the dimensions required for *in vivo* applications. These requirements are fulfilled through the utilization of an occlusive thrombus model and an X-ray-guided robotic platform.

5.1.1 *Ex vivo* endovascular thrombosis model

The aorta, renal arteries, and iliac arteries, along with blood, were obtained from euthanized sheep. The sheep (*Ovis aries*) were euthanized by injecting 15 mL of Euthasol (AST Pharma, Oudewater, the Netherlands) mixed with 5 mL of Heparin (5000 IU/mL, Leo Pharma, Ballerup, Denmark) into the jugular vein. After confirming death, the sheep was positioned in a Trendelenburg position, and both the jugular vein and the carotid artery were ligated to allow blood to flow into a container. After collecting as much blood as possible, it was stored on ice. Subsequently, the sheep was transported to the laboratory, where the vessels were carefully excised and placed in a bag on ice for transport to the operating room, as depicted in Fig. 21(a). During transport, the blood and excised vessels were kept on ice.

In experimental settings, blood clots resembling a 1-day-old state are induced by promoting natural coagulation, allowing the blood to undergo thickening and form a semisolid mass. Subsequently, the clot is carefully inserted into the iliac artery and guided beyond the iliac bifurcation, as illustrated in Fig. 22. At this stage, a diameter-reducing wire is employed to precisely trap the clot within the vessel. While the interaction between the clot and arterial wall naturally results in a trapping response and resistance to sliding, the deliberate use of a diameter-reducing

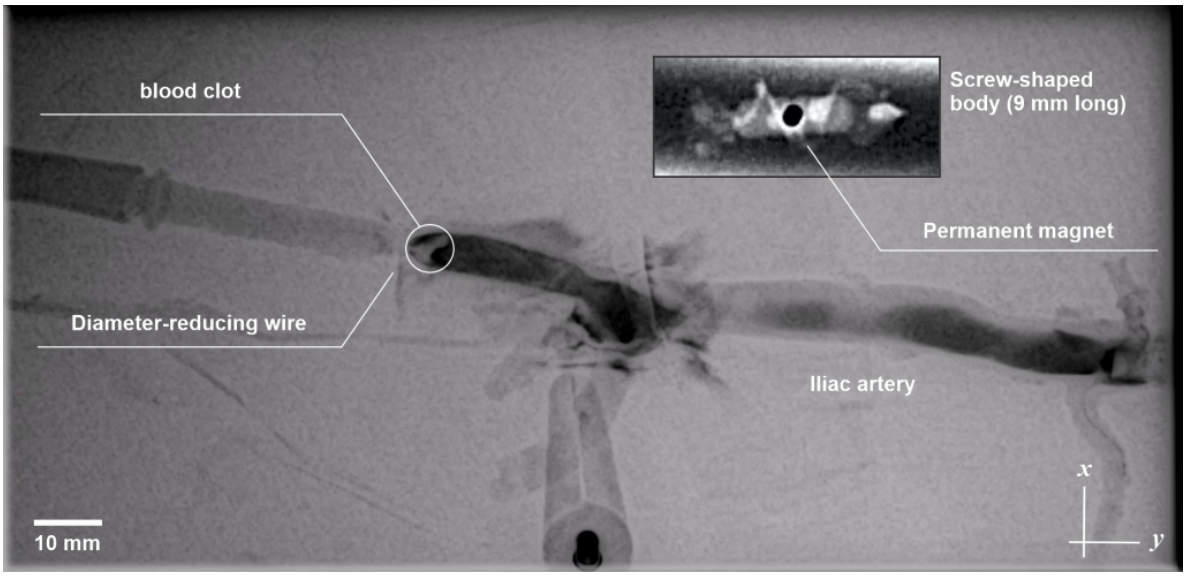

Fig. 22: *The* ex vivo *endovascular thrombosis model is depicted through X-ray Fluoroscopy imaging while injecting a radiocontrast agent along the negative* $\boldsymbol{y}$*-axis. A diameter-reducing wire is used to trap the blood clot. The untethered magnetic robot (top-right inset) is inserted from the proximal end of the iliac artery and guided toward the blood clot.*

wire becomes necessary due to the smaller diameter of the blood clots compared to that of the vessel. This facilitates easier insertion and manipulation of the clots within the experimental setup. Upon establishing an occlusive thrombus model, the X-ray-guided platform is employed to systematically assess the interactions between the UMR and the clot.

5.2 X-ray-guided teleoperation of biocompatible untethered magnetic robots

To deploy the UMR inside the *ex vivo* model, three essential functionalities must be incorporated: biocompatibility, controlled response to an external stimulus (i.e., an external magnetic field), and the generation of a detectable signal with a sufficient contrast to noise ratio in the acquired X-ray Fluoroscopy images, described in Section 2. Therefore, we fabricate screw-shaped bodies with an affixed permanent magnet (inset in Fig. 22) and coat their surface for biocompatibility, as outlined in Section 4.2.

5.2.1 Wireless control and targeting

The UMR is teleoperated to navigate toward the blood clot in the iliac artery, guided by X-ray Fluoroscopy images acquired at a real-time frame rate of 5 Hz, as discussed in Chapter 2. This operational frame rate facilitates precise control inputs from the operator, specifying the desired orientation for the RPM's rotation axis, the actuation frequency, and the direction of rotation of the RPM. The RPM's rotation axis (and its pose) is automatically controlled to facilitate the movement of the UMR within the iliac artery, a process dependent on the artery's geometry. The actuation frequency has a linear relationship with the swimming speed of the UMR, provided it stays below the step-out frequency. The third control input is the direction of rotation of the RPM, allowing the UMR to swim back and forth along the vessel. This control input is particularly useful, as one direction of rotation enables the UMR to swim toward the clot, while the other direction reverses its motion after engagement.

Fig. 23 illustrates the targeting response of the UMR. In this experiment, the UMR is controlled to move along the $+\boldsymbol{y}$-axis against blood flow, and then its motion is reversed. Upon motion reversal, the UMR moves along the blood flow (in the $-\boldsymbol{y}$-axis) toward the clot, which prevents its advancement. When the UMR is controlled to move away from the blood clot, its

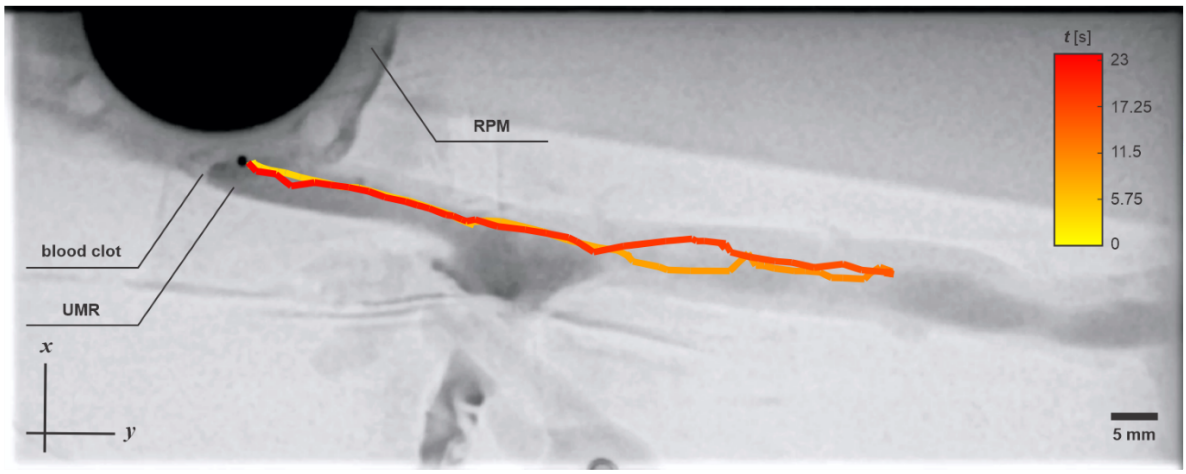

Fig. 23: *The untethered magnetic robot (UMR) is deployed within an* ex vivo *endovascular thrombosis model located in the iliac artery. The UMR is guided to swim along the* $\boldsymbol{y}$*-axis away from the blood clot, and its motion is then reversed, directing it back toward the clot for engagement. The rotating permanent magnet (RPM) rotation axis is controlled robotically to move and guide the UMR.*

swimming speed is measured to be 9.5 mm/s. In its path toward the blood clot, the swimming speed increases to 11.5 mm/s. The difference in forward and backward swimming velocity is attributed to blood flow, which is induced in the direction towards the blood clot.

In this trial, the UMR swims back and forth approximately 24 body lengths in approximately 20 seconds, at an actuation frequency of 9 Hz. At around 23 seconds, the UMR comes in contact with the blood clot, initiating its engagement with the fibrin network. At this point, several engagement strategies can be adopted to reinstate blood flow. One of these strategies is to drill through the blood clot using the propulsive thrust of the screw-shaped body. Alternatively, the UMR may be used to deploy a concentrated cargo of thrombolytic agent, breaking up and dissolving blood clots that impede blood flow. This chapter investigates the first method.

5.3 Engagement with blood clots

To evaluate the impact of the UMR on the clot, we investigate two distinct groups. The first group involves measuring the blood clots without drilling using the UMR, while the second group involves mechanical drilling for 30 minutes. In each case, the volume of the blood clot is reconstructed using CBCT scans taken every fifteen minutes. Cross-sectional images were generated through CBCT reconstruction to determine the clot's volume over time, as shown in Fig. 24.

5.3.1 Pre-interventional CBCT imaging – control

For the control, we measure the volume of the clot in the absence of any external stimuli, either mechanical or chemical. Blood clots are produced and trapped inside the iliac artery past the iliac bifurcation using the diameter-reducing wire. In the absence of clot-UMR interaction, the clot is reconstructed using CBCT scans every 15 minutes for 30 minutes. Our observations indicate minimal measurable change in the volume of the clot (Fig. 25). Therefore, the deployment of the UMR toward the clot and measuring the size of the clot versus drilling time can be assessed using this control measurment.

5.3.2 Post-interventional CBCT imaging – mechanical drilling

The UMR is deployed and guided using controlled rotating magnetic fields toward the clot, as depicted in Fig. 24. In this trial, a new blood clot is inserted and trapped inside the iliac artery.

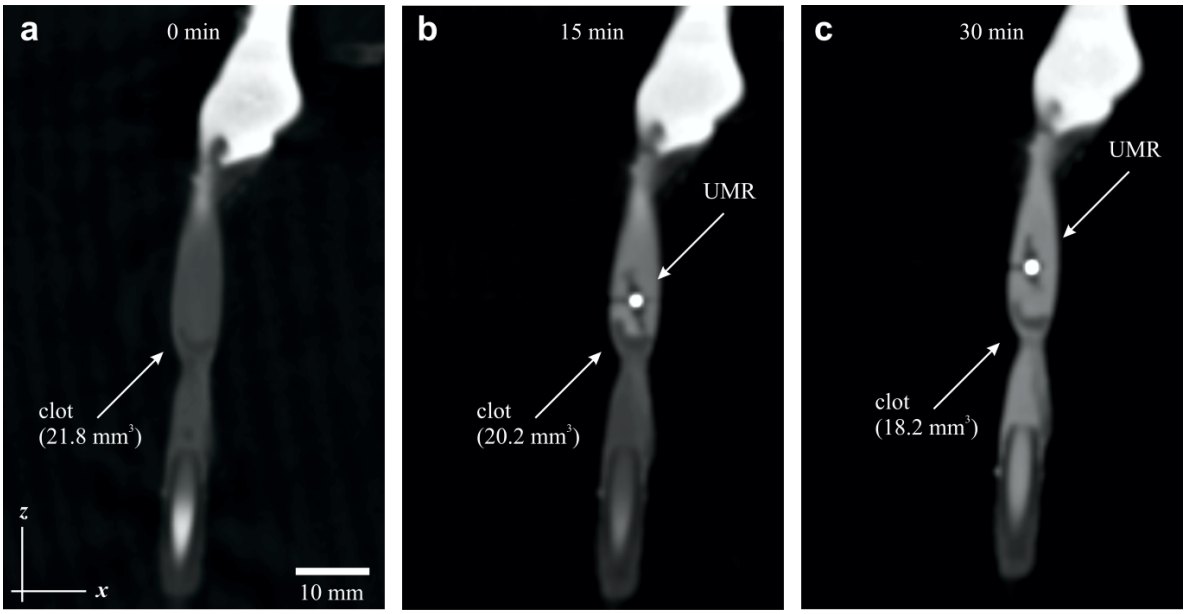

Fig. 24: *Pre- and post-interventional CBCT scans are collected every 15 minutes to establish the control and the drilling measurement, respectively. The size of the blood clot is measured from reconstructed scans, with the bright region indicating the untethered magnetic robot (UMR). (a) Initial blood clot volume measured using volume acquisition CT is 21.8 mm*^{3}*. (b) After 15 minutes, the volume decreases to 20.2 mm*^{3}*. (c) Grinding the blood clot for 30 minutes results in a volume reduction of* 16%*, yielding a clot volume of 18.2 mm*^{3}*.*

The blood clot and the UMR are highlighted in the CBCT scan as the bright and dark regions, respectively. Upon reaching the blood clot site, the UMR is allowed to grind the clot for 30 minutes on the axial plane, Fig. 26, and CBCT scans are collected every 15 minutes to monitor the clot's size and assess the impact of the UMR. The propulsive thrust of the rotating screw-shaped UMR enables continuous engagement with the clot, as illustrated in Fig. 24. While the UMR is not permitted to advance forward and drill through the clot, the magnetic torque exerted on its magnetic dipole facilitates continuous rotational motion, resulting in a grinding action. Similarly to the swimming speed of the UMRs, the rate of clot removal is likely to depend on the rotational frequency of the UMR, particularly below its step-out frequency. In this trial, the UMR operates at 11 Hz with a 10 cm distance from the RPM actuator, resulting in a maximum magnetic field of 4 mT at the UMR's position.

Fig. 24(a) illustrates the initial interaction between the UMR and the blood clot, with a corresponding volume acquisition CT measurement of 21.8 mm^3. Following 15 minutes of uninterrupted grinding with the rotating UMR, the volume decreases to 20.2 mm^3, as depicted in Fig. 24(b), reflecting a 1.6 mm^3 reduction in clot volume. Finally, the volume of the blood clot decreases to 18.2 mm^3 after 30 minutes, as shown in Fig. 24(c). Therefore, this experiment indicates that the grinding action between the UMR and blood clot yields a volume reduction of 3.6 mm^3.

Volume acquisition CT measurement of the blood clot involves using CT imaging to capture a 3D representation of the clot's volume, as shown in Fig. 25 and Fig. 26. In this context, the initial volume, measured at 21.8 mm^3, serves as a baseline. Subsequent CT scans at specific time intervals, such as 15 minutes and 30 minutes, provide insights into how the clot volume changes over time. The acquired images allow for a detailed assessment of the clot's structure and dimensions, enabling the evaluation of the impact of the UMR's grinding action on clot reduction.

At the initial time point ($t = 0$), the coronal plane displays a relatively blunt peak, and curved structure of the blood clot. However, after 30 minutes of continuous grinding, the peak

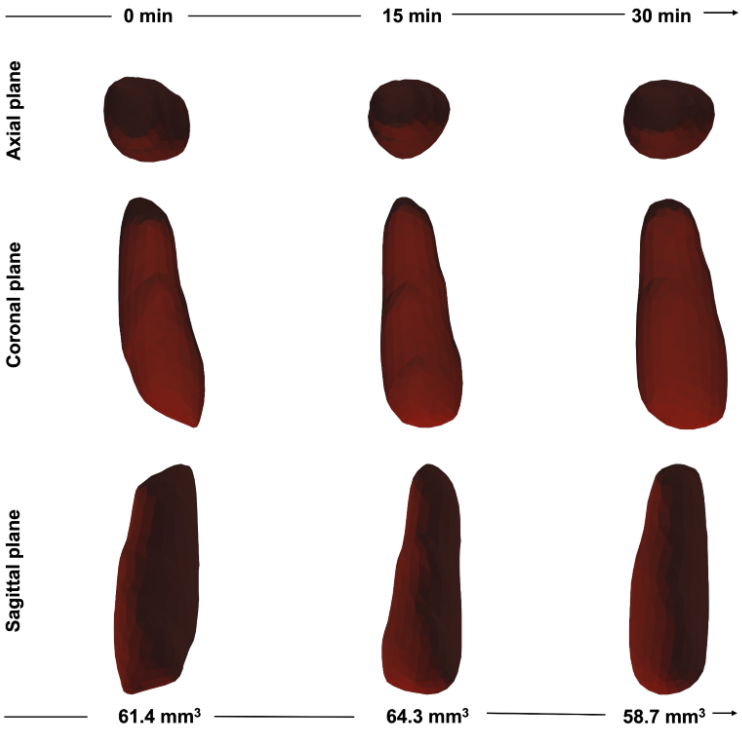

Fig. 25: *Volume acquisition CT is employed to reconstruct the volume of the blood clot int the control measurement. The initial volume of the blood clot is 61.4 mm^3, and it decreases to 58.7 mm^3 after 30 minutes. The clot size exhibits minimal change within a relative measurement error of* 5%.

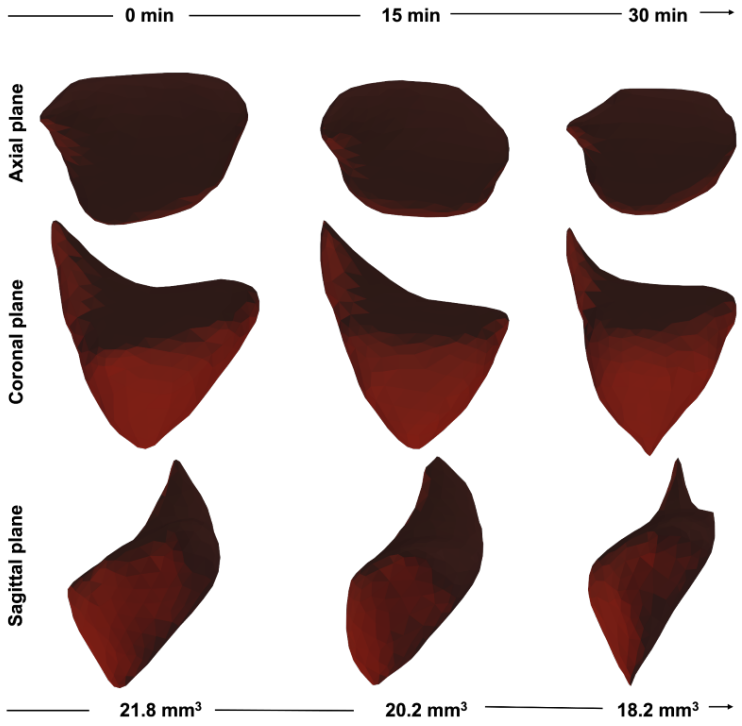

Fig. 26: *Volume acquisition CT is employed to reconstruct the volume of the blood clot. The initial volume of the blood clot is 21.8 mm^3, decreasing to 18.2 mm^3 after 30 minutes of grinding with an untethered magnetic robot (UMR). The tapering of the blood clot suggests that the UMR exerts a pushing force on the clot during the drilling process, grinding while oriented orthogonal to the axial plane.*

near the top-left side of the clot has shrunk and become distinctively sharper, viewed from the coronal plane in Fig. 26. This observation indicates the localized impact of the UMR's grinding action on the clot's geometry, resulting in the formation of a more prominent features within the clot structure. The axial and sagittal views further confirm that the UMR induces a tapered clot geometry that becomes progressively sharper with increased grinding time. This observation across multiple planes suggests a consistent and localized effect of the UMR's grinding action on the clot's overall shape.

5.4 Conclusions

In conclusion, our study represents an important advancement in medical microrobotics through the introduction of biocompatible UMRs designed for controlled responses to external magnetic fields. A key innovation is the implementation of an advanced *ex vivo* endovascular thrombosis model within the iliac artery, providing a vital tool for evaluating the efficacy of UMRs. These UMRs, featuring permanent magnets, exhibited precise real-time control in X-ray-guided interventions. The integration of CBCT scans for precise volumetric reconstruction unveiled a remarkable 16% reduction in clot volume within just 30 minutes of engagement. This pioneering approach holds immense potential for addressing acute ischemic stroke and vessel occlusions, opening avenues for advanced exploration in complex scenarios and future clinical applications. In future work, we aim to enhance the efficacy of the UMR's mechanical drilling or grinding approach by exploring a hybrid strategy that incorporates chemical lysis using thrombolytic agents. This involves investigating the potential benefits of either injecting or encapsulating thrombolytic agents with the UMR. The synergistic combination of mechanical and chemical approaches holds promise for optimizing clot dissolution, potentially improving the overall performance and efficiency of the UMR in addressing vascular occlusions and acute ischemic stroke.

References

[1] F. Carpi and C. Pappone, "Stereotaxis Niobe magnetic navigation system for endocardial catheter ablation and gastrointestinal capsule endoscopy," *Expert Rev. Med. Devices*, vol. 6, no. 5, pp. 487–498, 2009.

[2] T. W. R. Fountain, Prem V. Kailat, and J. J. Abbott, "Wireless control of magnetic helical microrobots using a rotating-permanent-magnet manipulator," in *Proc. IEEE Int. Conf. Robot. Autom.*, 2011, pp. 576–581.

[3] M. P. Kummer, J. J. Abbott, B. E. Kratochvil, R. Borer, A. Sengul, and B. J. Nelson, "OctoMag: An electromagnetic system for 5-DOF wireless micromanipulation," *IEEE Trans. Robot.*, vol. 26, no. 6, pp. 1006–1017, Dec. 2010.

6 Non-Buoyant Microrobots Swimming with Near-Zero Angle of Attack

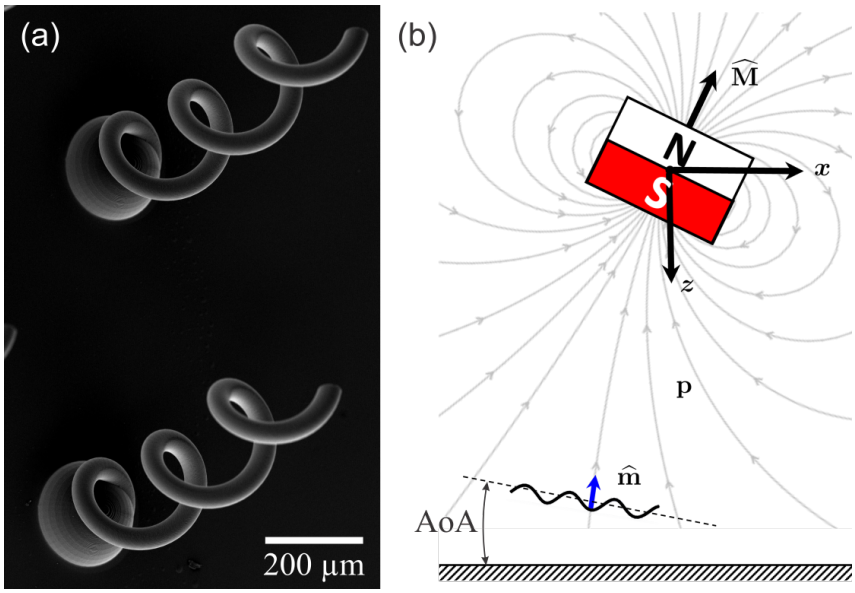

Fig. 27: *Helical microrobots (a) micrograph of microrobots (18% Ni, Wt%)(b) angle of attack (AoA) is increased to swim horizontally, to counteract downward drift due to gravity when submerged in a fluid. An AoA can be achieved by using the actuator's magnetic dipole* **M** *to orient the microrobots magnetization vector* **m** *perpendicular to the helical structure.*

Microorganisms have evolved locomotion mechanisms and densities that successfully exploit drag at low Reynolds numbers. The energy efficiency and anatomy of these organisms have inspired microrobot designs that consist mostly of a wire formed into a helix [1, 2] or an elastic filament [3, 4]. However, when compared in terms of hydrodynamic efficiency, microorganisms outperform microrobots by a large margin in terms of swimming efficiency. Despite the bio-inspired geometrical design of most microrobots, their swimming efficiency is considerably lower than microorganisms. Consider, for example, a microrobot formed into a helix (Fig. 6(a)), the most common design [5], of a non-buoyant material to work under the influence of an external magnetic field. Unlike buoyant microorganisms, the microrobot would be required to swim with a relatively large angle of attack (i.e., vertical angle enclosed between the long axis of the microrobot and the horizontal plane, as shown in Fig. 6(b)) to avoid sinking under its own weight [6].

At least three implications for the increased angle of attack (AoA) can be expected. The first involves a decrease in the swimming speed resulting in a decrease in the swimming efficiency, due to having a thrust component to counteract gravity. The second challenge relates to the restricted maneuverability of microrobots in confined environments like capillaries or small vessels. However, these adjustments may not always be feasible due to the physical constraints of the confined environment. The third involves controlling the AoA in closed-loop, placing strong requirement for orientation localization, which has been proven to be challenging in bodily fluids using imaging systems at microscale [7]. For practical use, the orientation of the microrobot must be controlled based on a prescribed trajectory towards its target without using the microrobot's propulsive thrust to compensate for its weight. The goal of this chapter is to bridge the gap between theoretical predictions and experimental application for helical propulsion at low-Re with near-zero AoA when the microrobot is heavier than buoyant microorganisms.

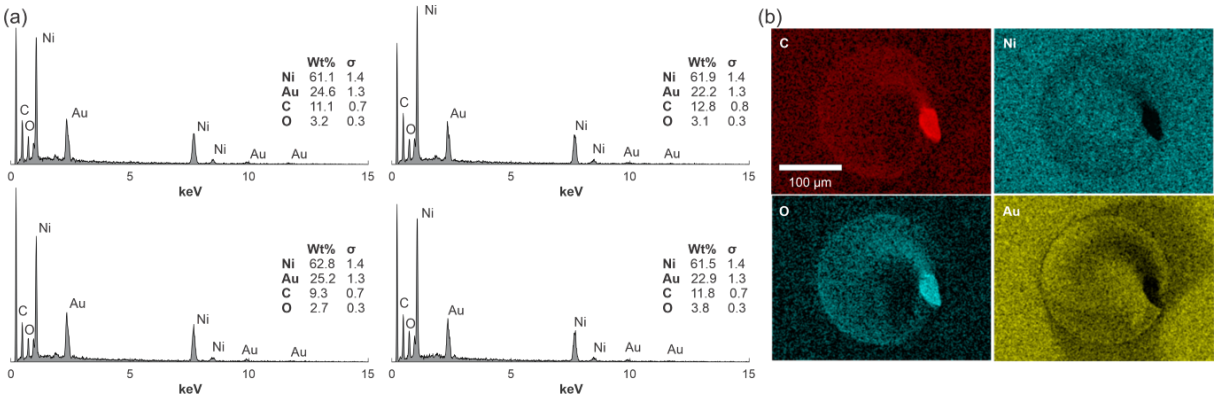

Fig. 28: *Element-wise composition of the magnetic microrobot using scanning electron microscopy (SEM) coupled with energy dispersive x-ray (EDX): (a) EDX spectra for four different instances of the microrobot, and (b) EDX color-coded elemental map (Ni, Au).*

6.1 Boundedness of an open-loop controlled microscale untethered magnetic robots

Despite the considerable progress in the development of biohybrid microrobots which consist of microorganisms that have a density close to water [8, 9, 10], a magnetic component must still be incorporated for a specific functionality such as emitting detectable signal for localization or transducing power for propulsion and steering. Our approach is universal to any magnetic microrobot, and applies to both predominant forms of actuation using magnetic fields, i.e., field-driven torques or gradient pulling. Such magnetic microrobots may be submerged in a viscous fluid and subject to external torques to advance with forward motion out of rotation about their long axis.

In the limit of low-Re, the total hydrodynamic drag of the helical body with a centerline $\mathbf{r}(s)$, $\mathbf{f}$, magnetic force and torque, $\mathbf{f}_\mathrm{m}$ and $\mathbf{T}_\mathrm{m}$, and gravitational force and torque, $\mathbf{f}_\mathrm{g}$ and $\mathbf{T}_\mathrm{g}$, must vanish:

$$\int_0^L \mathrm{d}s \begin{pmatrix} \mathbf{f}(s) \\ \mathbf{f}(s) \times \mathbf{r}(s) \end{pmatrix} + \begin{pmatrix} \mathbf{f}_\mathrm{m} + \mathbf{f}_\mathrm{g} \\ \mathbf{T}_\mathrm{m} + \mathbf{T}_\mathrm{g} \end{pmatrix} = 0, \tag{8}$$

where L is the length of the helix and s is the arc length position ($0 \leq s \leq L$). According to Equation (8), if the helical body is subject to an external field-gradient pulling, it will move with a velocity satisfying the force balance. Unless the microrobot has a similar density to that of the surrounding, there will not be any steady swimming horizontally. A microrobot with density ρ_r submerged in a fluid with density ρ_f is subject to gravitational force $\mathbf{f}_\mathrm{g} = V(\rho_\mathrm{r} - \rho_\mathrm{f})\mathbf{R}_\mathrm{Lab}^T \boldsymbol{g}$, which will likely be responsible for a downward drift, where V, $\mathbf{R}_\mathrm{Lab}^T$ and $\boldsymbol{g}$ are the volume, rotation matrix of the microrobot and gravitational acceleration, respectively.

Achieving near-zero AoA requires the compensation of gravitational forces, $\mathbf{f}_\mathrm{g}$, by the vertical magnetic forces, $\mathbf{f}_\mathrm{mz}$. This enables the average vertical velocity of the microrobot, $\dot{p}_z$, to be zero, which can be predicted by [11, 12, 13]:

$$\dot{p}_\mathrm{z} = \frac{\cos(\theta)}{C_\mathrm{n} \sin^2(\theta) L} \left(\mathbf{f}_\mathrm{mz} - \mathbf{f}_\mathrm{g}\right), \tag{9}$$

$$C_\mathrm{n} = \frac{4\pi\eta}{\ln\left(\frac{2p}{d_\mathrm{w}}\right) + \frac{1}{2}} \tag{10}$$

where p represent the helical pitch and d_w diameter of the filament, while θ represents the helical pitch angle. The viscosity of the surrounding fluid is given by η. The magnetic forces acting on a soft magnetic structure are influenced by the magnetization vector $\mathbf{m}$, the applied magnetic

Table 2: *The geometric and material properties of the microrobot, based on its computer-aided design (CAD) model and fabrication properties, respectively.*

CAD measurements		Material predictions	
L [µm]	1200	t_{Ni} [nm]	300
d_{UMR} [µm]	235	t_{Au} [nm]	50
d_{w} [µm]	50	V_{Ni} [m^3]	1.11×10^{-13}
p [µm]	333	V_{Au} [m^3]	1.87×10^{-14}
V [m^3]	4.74×10^{-12}	$V_{\mathrm{C\&O}}$ [m^3]	4.61×10^{-12}

field $\mathbf{H}_{\mathrm{f}}$, the volume of the soft-magnetic material nickel, denoted as V_{Ni}. This relationship can be expressed as follows:

$$\mathbf{f}_{\mathrm{m}} = \mu_0 V_{\mathrm{Ni}} (\mathbf{m}(\mathbf{p}) \cdot \nabla) \mathbf{H}_{\mathrm{f}}(\mathbf{p}), \tag{11}$$

where μ_0 is the permeability of free space. The magnetization vector $\mathbf{m}$ depends on the applied magnetic field $\mathbf{H}_{\mathrm{r}}$ on the nickel based microrobot and the susceptibility of nickel χ_{Ni}, $\mathbf{m} = \chi_{\mathrm{Ni}} \mathbf{H}_{\mathrm{r}}$. The magnetic field $\mathbf{H}$ at point $\mathbf{p}$ is given by:

$$\mathbf{H}(\mathbf{p}) = \frac{1}{4\pi\mu_{\mathrm{r}} ||\mathbf{p}||^3} \left(3\hat{\mathbf{p}}\hat{\mathbf{p}}^{\mathrm{T}} - \mathbb{I}\right) \mathbf{M}, \tag{12}$$

where μ_{r} is the relative permeability, $\mathbf{p}$ is the position of the microrobot, $\mathbb{I}$ is an identity matrix and $\mathbf{M}$ is the dipole moment created by the rotating permanent magnet. By utilizing Equations (11-12), we can determine the velocity of the microrobot, denoted as $\dot{p}_z$, as $\mathbf{M}$ undergoes a full cycle within the range of 0 to 2π, and at a distance $\mathbf{p}$. This analysis allows us to find the equilibrium position where the microrobot can swim with a zero AoA, with the average velocity $\langle \dot{p}_z \rangle$ being equal to zero.

6.2 Microrobot fabrication and characterization

Microbots are 3D micro-printed with IP-Dip photoresin on substrate using Direct Laser Writing (DLW, Nanoscribe GmbH). Next, the microrobots are deposited with a layer of Ni with thichness, t_{Ni}, 300 nm, followed by a, t_{Au}, 50 nm Au layer, serving as an inert protective. The EDX spectra (Fig. 28) reveal the predominant Ni and Au composition of the microbots, with additional organic impurities such as C and O due to the presence of photoresin.

The geometric and material properties of the microrobots, as detailed in Table 2, can be utilized in Equation (9-10) to predict their vertical speed during helical propulsion. In Fig. 29(a), a periodic solution (represented by the black closed curve) is depicted within the interval $[0, 2\pi)$. This periodic solution regularly intersects with the equilibrium trajectory, denoted as $\langle p_z^* \rangle$, averaged over one period of the actuator magnet rotation and shown as a red circle. The periodic intersection between $\langle p_z^* \rangle$ and p_z^* enables the vertical speed of the microrobot to change periodically and follow a rose curve profile, as shown by the blue curve in Fig. 29(a).

Note that Equation 9 provides an optimal actuator-microrobot gap of approximately 40 mm, allowing the microrobot to remain bounded for all $t > 0$. The influence of this gap on the velocity profile is shown in Fig. 29(b). For a relatively large actuator-microrobot gap, the field-gradient pulling may not be sufficient to overcome the weight, resulting in an oval curve velocity profile. Therefore, the vertical velocity components never go to zero, leading to vertical drift and an unbounded response. As the actuator-microrobot gap decreases, the velocity profile transforms into a rose curve. This velocity profile indicates that field-gradient pulling and gravity balance at four angular orientations during each full cycle of actuator rotation. As the gap further increases, the velocity profile changes to a periodic lemniscate curve. This velocity profile indicates that the vertical velocity varies periodically along one direction, resulting in attraction toward the actuator and unbounded response.

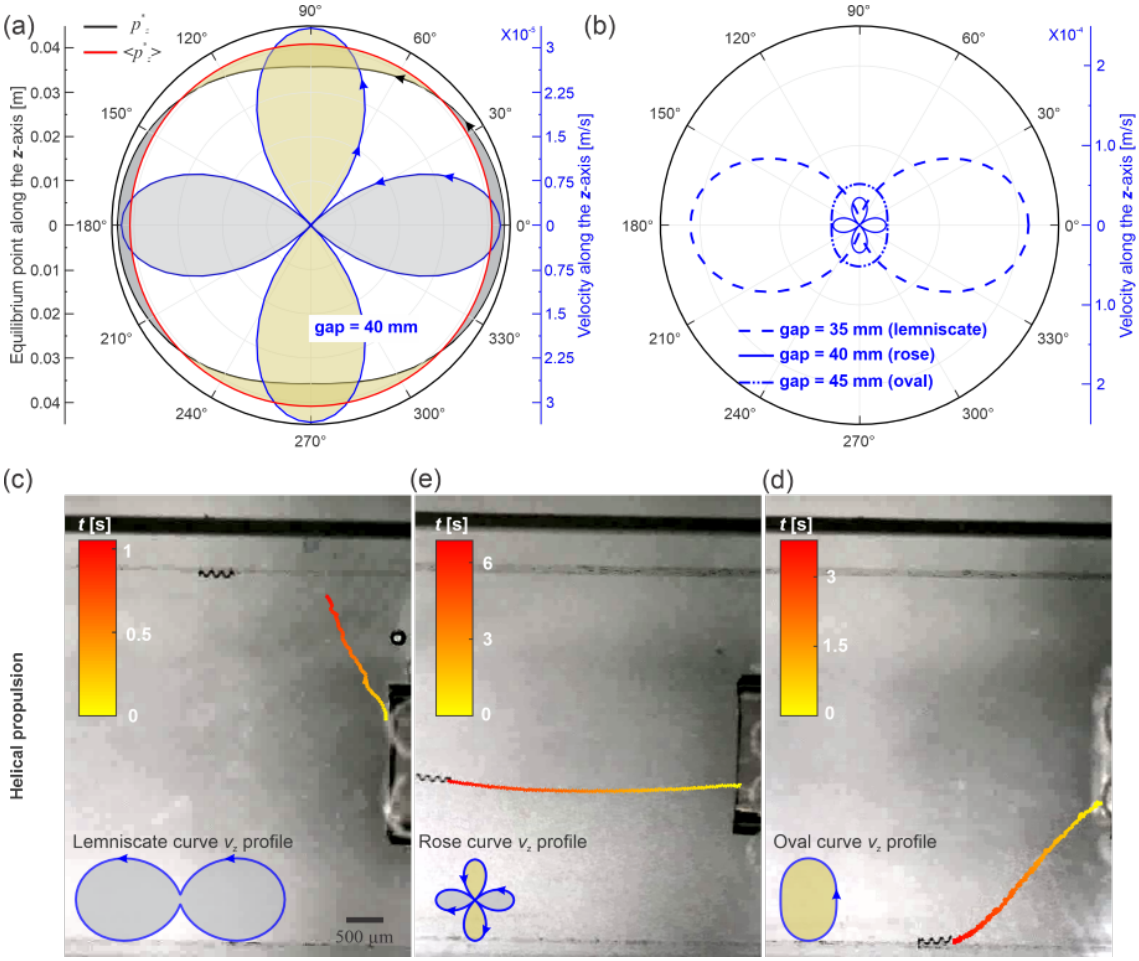

Fig. 29: *Active suspension of the helical microrobot is achieved and enables swimming with near-zero angle of attack. (a) The rotational motion of the rotating permanent magnet (RPM) and the microrobot in the interval* $[0, 2\pi)$ *provides a periodic solution for the equilibrium,* p_z^* *(black curve). The equilibrium,* $\langle p_{\mathrm{h}_z}^* \rangle$*, is averaged over one period of RPM rotation (red curve). The velocity (rose curve) decreases and tends to a minimum in the first-quadrant-third-quadrant. It decreases from a maximum and tends to a minimum in the second-quadrant-fourth-quadrant as the actuator completes one period. (b) As the actuator-microrobot-gap increases, the velocity profile changes from a lemniscate curve (35 mm) to a rose curve (40 mm) to an oval closed curve (45 mm). (c)-(e) Swimming with a velocity profile resembling a rose curve allows for a reduction in the angle of attack and minimizes the average vertical speed.*

6.3 Experimental validation

To evaluate the performance of the model, experiments were conducted at actuator-microrobot gap within a range of 35 mm to 45 mm and were actuated at frequencies ranging from 10 to 40 Hz. The microcrobot's displacement is visualized using a Keyence Digital Microscope. Figs. 29(c)-29(e) shows the vertical displacement of the swimming microrobot in three cases, irrespective of the actuation frequency. In Fig 29(c), the field-gradient pulling dominates, resulting in a lemniscate curve velocity profile and unbounded attraction toward the actuator (the microrobot is confined by the inner side wall of the cuvette). On the contrary, Fig 29(d), the rose curve velocity profile enables symmetric reciprocating velocity, facilitating bounded locomotion without vertical drift. Subsequently, Fig. 29(e), the rose curve velocity profile transitions into an oval curve, leading to a downward drift due to gravity.

Fig. 30 depicts the swimming trajectory of the microrobot and the measured AoA for three different trials. A near-zero AoA of $0.8° \pm 0.6°$ is achieved allowing the microrobot to swim horizontally making use of a greater portion of the propulsive thrust for locomotion. Swimming

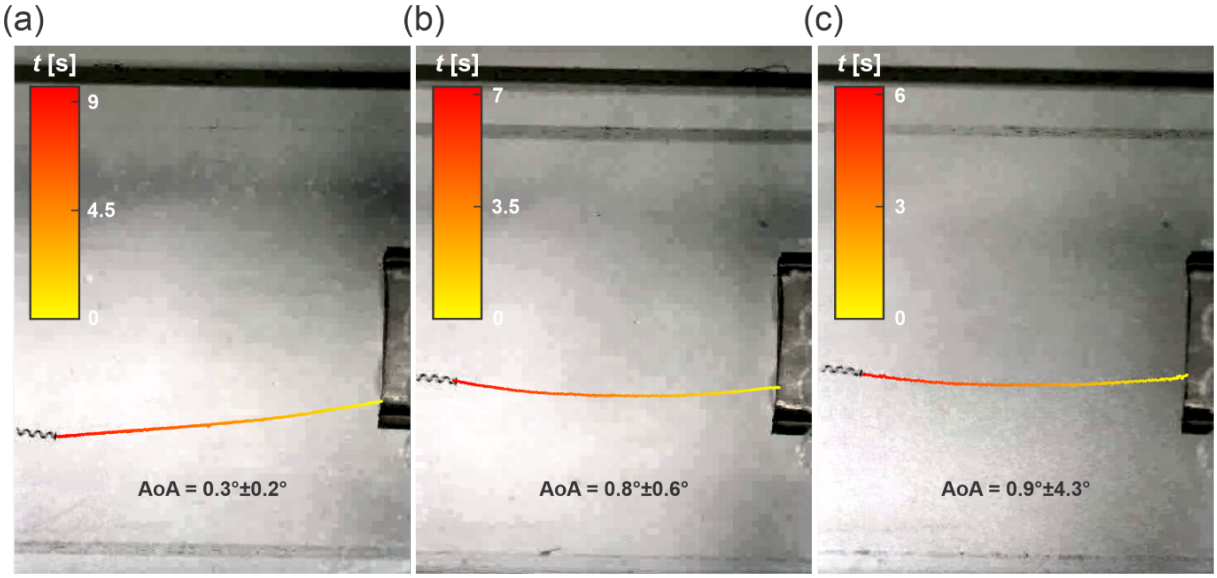

Fig. 30: *The helical microrobot demonstrates near-zero angle of attack (AoA) under varying actuation frequencies. (a-c) The microrobot swim horizontally with AoA of* $0.3° \pm 0.2°$, $0.8° \pm 0.6°$, *and* $0.9° \pm 4.3°$, *respectively.*

with near-zero AoA allows a larger portion of the propulsive thrust to contribute to forward velocity.

This chapter highlights the critical influence of the actuator-microrobot gap on the swimming behavior of helical microrobots. It demonstrated that the gap size plays a pivotal role in determining the AoA and, consequently, the efficiency of forward swimming. Varying the gap size and actuation frequency provide distinct velocity profiles and behavioral patterns. These findings offer valuable insights for optimizing the design and control of microrobots in microscale environments, contributing to advancements in microrobotic locomotion.

References

[1] L. Zhang, J. J. Abbott, L. Dong, B. Kratochvil, D. Bell, and B. Nelson, "Artificial bacterial flagella: Fabrication and magnetic control," *Applied Physics Letters*, vol. 94, pp. 064107, 2009.

[2] A. Ghosh and P. Fischer, "Controlled Propulsion of Artificial Magnetic Nanostructured Propellers," *Nano Letters*, vol. 9, pp. 2243-2245, 2009.

[3] R. Dreyfus, J. Baudry, M. Roper, M. Fermigier, H. Stone, and J. Bibette, "Characterizing the Swimming Properties of Artificial Bacterial Flagella," *Nature*, vol. 437, pp. 862-865, 2006.

[4] B. Williams, S. Anand, J. Rajagopalan, and M. Saif, "A self-propelled biohybrid swimmer at low Reynolds number," *Nature*, vol. 5, pp. 3081, 2014.

[5] J. Abbott, K. Peyer, M. Lagomarsino, L. Zhang, L. Dong, I. Kaliakatsos, and B. Nelson, "How Should Microrobots Swim?," *The International Journal Of Robotics Research*, vol. 28, pp. 1434-1447, 2009.

[6] A. Mahoney, J. Sarrazin, E. Bamberg, and J. J. Abbott, "Velocity Control with Gravity Compensation for Magnetic Helical Microswimmers," *Advanced Robotics*, vol. 25, pp. 1007-1028, 2011.

[7] A. Aziz, S. Pane, V. Iacovacci, N. Koukourakis, J. Czarske, A. Menciassi, M. Medina-Sánchez, and O. Schmidt, "Medical Imaging of Microrobots: Toward In Vivo Applications," *ACS Nano*, vol. 14, pp. 10865-10893, 2020.

[8] B. Behkam and M. Sitti, "Bacterial flagella-based propulsion and on/off motion control of microscale objects," *Applied Physics Letters*, vol. 90, pp. 023902, 2007.

[9] V. Magdanz, S. Sanchez, and O. Schmidt, "Development of a Sperm-Flagella Driven Micro-Bio-Robot," *Advanced Materials*, vol. 25, pp. 6581–6588, 2013.

[10] X. Yan, Q. Zhou, M. Vincent, Y. Deng, J. Yu, J. Xu, T. Xu, T. Tang, L. Bian, Y. Wang, K. Kostarelos, and L. Zhang, "Multifunctional biohybrid magnetite microrobots for imaging-guided therapy," *Science Robotics*, vol. 2, pp. eaaq1155, 2017.

[11] L. Ligtenberg and I. Khalil, "Input-Output Boundedness of a Magnetically-Actuated Helical Device," *2023 IEEE International Conference On Robotics And Automation (ICRA)*, 2023.

[12] B. Rodenborn, C. Chen, H. Swinney, B. Liu, and H. Zhang, "Propulsion of microorganisms by a helical flagellum," *Proceedings Of The National Academy Of Sciences*, vol. 110, pp. E338-E347, 2013.

[13] J. Gray and G. Hancock, "The propulsion of sea-urchin spermatozoa," *Journal Of Experimental Biology*, vol. 32, pp. 802-814, 1955.

7 Controlled Locomotion of IRONSperm Clusters: Evaluating Maneuverability with X-Ray-Guided Magnetic Fields

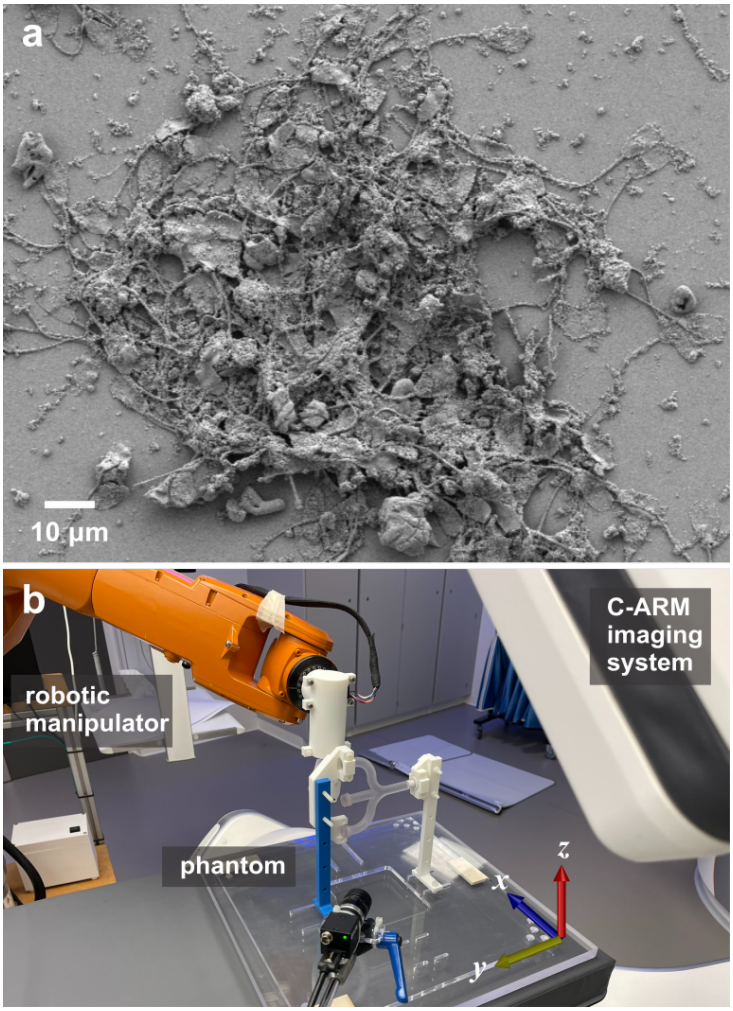

Fig. 31: *Nanoparticle-coated sperm cells are precisely guided through X-ray-guided magnetic fields. (a) Surrounding sperm cells with nanoparticles generates a dipole moment, allowing for magnetic actuation and enabling noninvasive detection through radiation absorption. (b) An X-ray-guided robotic system ensures accurate localization and control of the sperm cells.*

Annually, more than 142,000 cases of endometrial cancer and approximately 225,000 cases of ovarian cancer are reported, ranking them as the 6th and 8th most common cancers in women. The current treatment approach for these cancers involves a combination of surgical cytoreduction and adjuvant chemotherapy, leading to a 5-year survival rate below 50% for ovarian cancer and approximately 75% for endometrial cancer [1]-[4].

In the field of biomedical engineering, there has been a notable increase in interest surrounding soft biohybrid microrobots. These microrobots show promise for applications such as targeted drug delivery, local hypothermia generation, and cell microsurgery [5]. Their compact design and biocompatibility make them highly desirable, especially for navigating cavities and small spaces where traditional robots and catheter-based approaches face limitations. Various articles have proposed different methods of actuation techniques for biohybrid microrobots [6]-[10].

Magnetic control stands out among other methods due to its non-chemical interaction, negligible attenuation in the human body, and a long-range working distance, allowing for excellent external control [11]. Magnetic actuation provides various locomotion principles, including field

gradient pulling, helical or flagellar propulsion, and surface rolling, with many of these techniques utilizing rotating magnetic fields to propel microrobots.

RPMs have been proposed as a suitable method for generating these rotating magnetic fields. RPMs are often coupled to a 6-DOF manipulator to control the position and orientation of the magnet in 3D space. Despite their success, RPM control schemes typically rely on closed-loop feedback for accurate control, which can be challenging to provide [12, 13]. This challenge arises for two key reasons: First, biohybrid microrobots, composed of organic matter such as nanoparticle-coated microorganisms (Fig. 31(a)), are difficult to localize using noninvasive imaging systems due to their relatively low acoustic impedance with their surroundings or radiolucent material, making them challenging to localize using ultrasound or X-ray Fluoroscopy imaging, respectively. Second, feedback using radiation-based imaging techniques may have negative side-effects when high doses of radiation are used to improve localization resolution during feedback control. Therefore, open-loop control methods can be a reliable option when feedback is temporarily or permanently unavailable.

Overcoming challenges in achieving complete control for microrobots, especially in automating control in 5-DOF (three translational and two rotational dimensions), remains a persistent issue. Many locomotion techniques face limitations in dealing with gravitational and viscous drag forces, particularly in maintaining a vertical position. The need to counteract these forces significantly affects the efficiency of the intended motion, resulting in reduced speed in the desired direction. However, rolling locomotion eliminates the requirement for force compensation by maintaining continuous contact between the microrobot and a nearby rolling surface. This approach eliminates the necessity to navigate freely within a fluid-filled space or cavity, making use of their natural physical constraint to reach the intended target.

Spermatozoa provide an excellent template for magnetically actuated microrobots, owing to their intrinsic flexibility and drug loading capability. With their organic components, they demonstrate low cytotoxicity. Coating the spermatozoa with nanoparticles, resulting in IRONSperm, enables magnetic actuation and visualization using medical imaging. Clusters of these IRONSperm cells showcase the ability to engage in rolling locomotion when exposed to a rotating magnetic field controlled robotically using a robotic manipulator, as shown in Fig. 31(b). However, achieving reliable control of this locomotion is essential to unlock a greater potential for IRONSperm.

Ultrasound imaging has been identified as the preferred modality for detecting and assessing the position of IRONSperm clusters [14]. While this cost-effective technique has shown success in localization trials, it is characterized by a poor contrast to noise ratio. X-ray fluoroscopy imaging has been acknowledged as the most suitable method for real-time tracking of IRONSperm clusters. This chapter aims to investigate and visualize the 3D locomotion of IRONSperm clusters, with a focus on rolling locomotion, maneuverability, and RPM tracking capability within an enclosed environment featuring 3D geometry, utilizing X-ray-guided magnetic fields.

7.1 IRONSperm cluster formation and actuation

Individual bovine sperm cells are immersed in a suspension containing magnetic iron nanoparticles (MNPs) with an approximate diameter of 15 nm. Utilizing electrostatic interactions, the negatively charged cells and positively charged MNPs undergo a self-assembly process (Fig.31(a)). The resulting IRONSperm cells are aggregated into cohesive clusters through a rotating magnetic field [15]. In response to an external magnetic field generated by an RPM (Fig.31(b)), the magnetic dipole moment of the clusters trails behind the magnetic moment of the RPM, compelling them to mimic the magnet's motion. Consequently, this prompts the IRONSperm clusters to engage in rolling locomotion (Fig. 32(a)).

IRONSperm clusters undergo diverse physical interactions, facilitating rolling locomotion. Given the anticipated low Reynolds number conditions in the target environment for IRONSperm, the force and torque (magnetic, drag, and friction) balance governing the cluster's be-

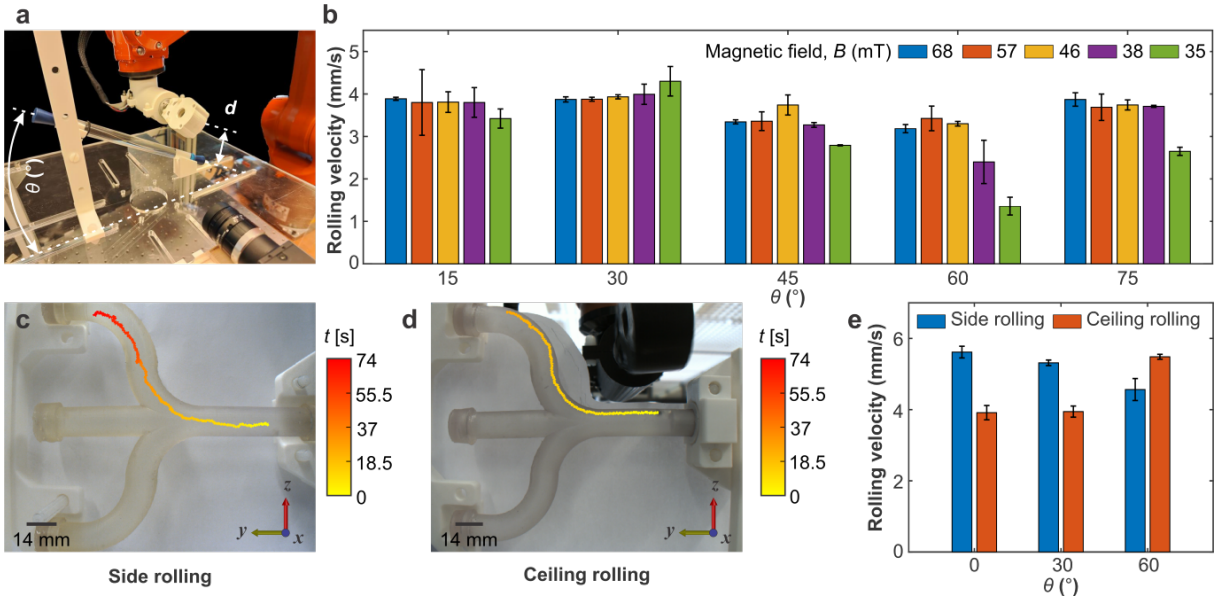

Fig. 32: *The investigation explores the impact of both the gap (d) between the RPM and the biohybrid microrobots and the inclination angle (θ) of the confinement on the rolling velocity. In (a), the microrobots are confined within a transparent water-filled tube, allowing them to roll at various inclination angles concerning the xy-plane. (b) illustrates the rolling speed (mean ± standard deviation) under constant rotating magnetic field of 1.5 Hz, demonstrating a slight decrease as the inclination angle increases from* 15° *to* 75° *and as the RPM-cluster gap widens from* $d = 37.5$ *mm to* $d = 47.5$ *mm. (c)-(d) showcase successful side and ceiling rolling maneuvers employed for navigating the pitchfork phantom. Additionally, (e) reveals an inverse relationship between the inclination angle (θ) increase and the corresponding decrease in side rolling, while ceiling rolling displays an increase.*

havior is described by the following equation:

$$\begin{pmatrix} \mathbf{F}_\mathrm{m} + \mathbf{F}_\mathrm{d} + \mathbf{F}_\mathrm{f} \\ \boldsymbol{\tau}_\mathrm{m} + \boldsymbol{\tau}_\mathrm{d} + \boldsymbol{\tau}_\mathrm{f} \end{pmatrix} = 0, \tag{13}$$

where $\mathbf{F}_\mathrm{m}$ represents the magnetic field gradient pulling force between the RPM and the IRONSperm cluster. This force may also come into play between individual particles of a cluster, which are formed when the external forces outlined in Equation 13 surpass the forces preserving the cohesion of the individual IRONSperm cells within the cluster, resulting in partial or complete disintegration. In this case, the force between two nearby IRONSperm clusters is given by

$$\mathbf{F}_\mathbf{m} = \frac{3\mu_0}{4\pi|\mathbf{r}|^4}(\mathbf{m_2}(\mathbf{m_1}\cdot\hat{\mathbf{r}}) + \mathbf{m_1}(\mathbf{m_2}\cdot\hat{\mathbf{r}})\hat{\mathbf{r}}(\mathbf{m_1}\cdot\mathbf{m_2}) - 5\hat{\mathbf{r}}(\mathbf{m_1}\cdot\mathbf{r})(\mathbf{m_2}\cdot\hat{\mathbf{r}})), \tag{14}$$

where $\mathbf{m}_1$ and $\mathbf{m}_2$ are the magnetic moment of two nearby clusters, μ_0 is the permeability of free space, $\hat{\mathbf{r}}$ is the unit vector between the clusters, and $|\mathbf{r}|$ is the distance between them. In Equation (13), $\mathbf{F}_\mathrm{d}$ denotes the viscous drag force given by $\mathbf{F}_\mathrm{d} = \mathrm{f_t}\mathbf{v}$ (with $\mathrm{f_t}$ the translational drag coefficient and $\mathbf{v}$ the cluster velocity), and $\mathbf{F}_\mathrm{f}$ represents the frictional force exerted on the cluster. Additionally, $\boldsymbol{\tau}_\mathrm{m}$, $\boldsymbol{\tau}_\mathrm{d}$, and $\boldsymbol{\tau}_\mathrm{f}$ stand for the magnetic, drag, and frictional torques, respectively. The magnetic torque is expressed as $\boldsymbol{\tau}_\mathrm{m} = \mathbf{m} \times \mathbf{B}$, where $\mathbf{B}$ is the magnetic field. This magnetic torque is generated by the misalignment of the magnetic field of the cluster and RPM, tending the cluster to rotate in an attempt to align with the field. The friction exerted by the rolling plane on the cluster in combination with the magnetic torque enables the IRONSperm cluster to roll.

The viscous drag torque is calculated using $\boldsymbol{\tau}_\mathrm{d} = \mathrm{f_r}\omega_\mathrm{c}$, where $\mathrm{f_r}$ is the rotational drag coefficient, and ω_c is the angular velocity of the cluster [14]. Depending on the magnitude of gradient pulling, a cluster can travel along the surface closest to the RPM or the opposite surface [15].

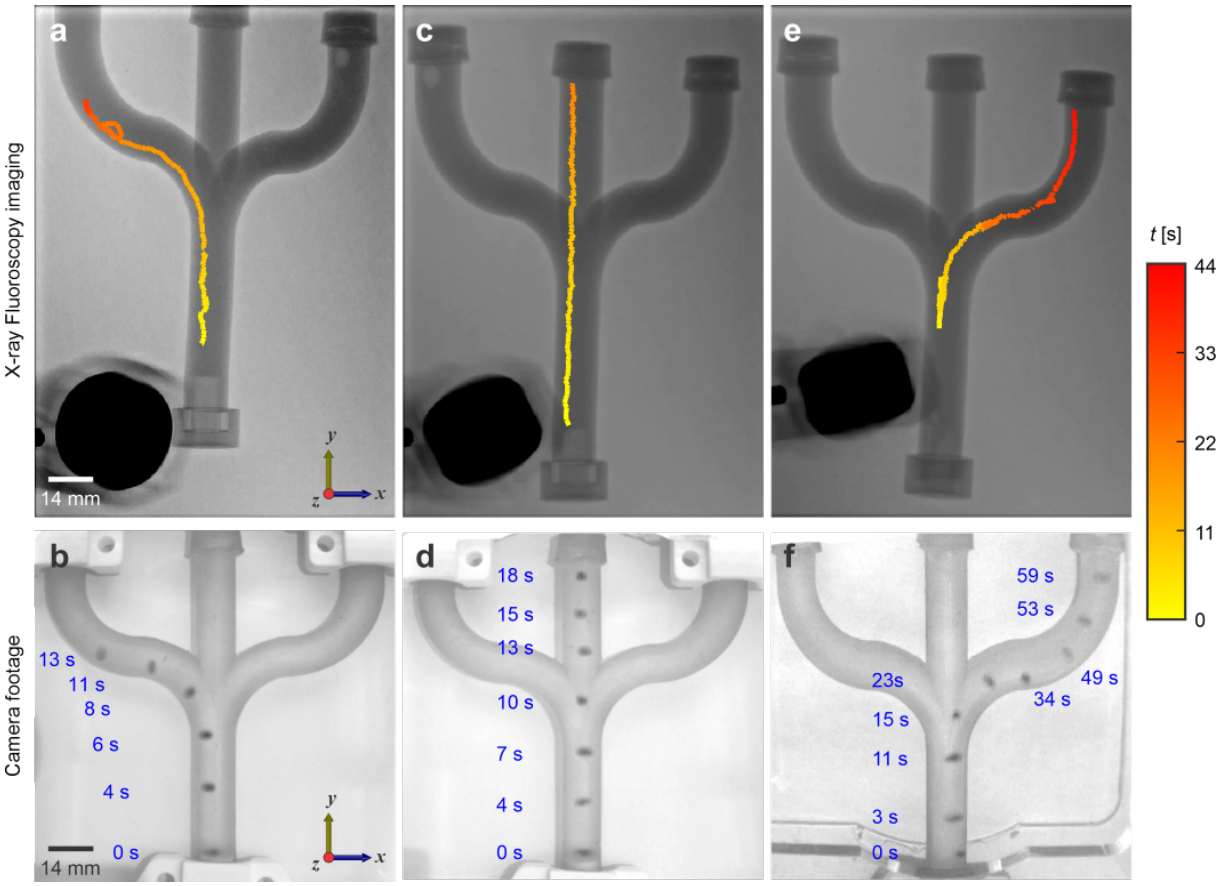

Fig. 33: *Successful trials of the forward left, middle, and right branch in the trifurcation phantom. The cluster's trajectory over time [s] is visualized with a color gradient line. Certain segments of the trajectory were not visible in the X-ray images due to radiation absorption by the RPM or low contrast of the cluster. (a)-(b) The cluster is controlled to roll along the left branch of the phantom. (c)-(d) The cluster is controlled to roll along the middle branch of the phantom. (e)-(f) The cluster is controlled to roll along the right branch of the phantom.*

The pulling force allows for a larger frictional force with the rolling plane and has been shown to increase rolling speed rather than bottom-floor locomotion.

7.2 Characterization and wireless actuation

7.2.1 Impact of inclination angle and actuation distance

To assess and quantify the vertical rolling capabilities of IRONSperm clusters, their response was examined on inclined surfaces of varying angles, θ. A single IRONSperm cluster, with a nanoparticle concentration of 3 mg/mL and fabricated using the method proposed by Magdanz *et al.*, was employed for all trials [15]. The cluster was situated in a transparent perspex tube filled with a 0.9% saline solution, as shown in Fig. 32(a). The experiment encompassed testing 5 angles, ranging from 15° to 75° in 15° increments for each angle. For each angle, 5 different actuation distances, d, were examined, corresponding to increasing magnetic field strength. The RPM traversed in a linear trajectory above the tube, covering a distance of 180 mm under the respective angles parallel to the tube.

The trials were conducted in triplicate, ensuring a consistent linear speed of the RPM at 4 mm s^{-1} and an RPM rotation frequency of 1.5 Hz. The direction was switched upon alterations in the RPM trajectory using a KUKA 6-DOF manipulator (KUKA KR-10 1100-2, KUKA, Augsburg, Germany). The entire experimental process was recorded using a FLIR Blackfly camera equipped

with a Fujinon 1:1.2/6 mm lens, capturing at a framerate of 30 frames per second.

Fig. 32 presents an analysis of the cluster's velocity under varying conditions, illustrating the rolling motion along the slope as depicted in Fig. 31(b). The data shows a slight linear regressive pattern in velocity with increasing angle, with a magnetic field strength of 68 mT resulting in relatively constant velocities for all angles. In the range of 37.5-47.5 mm (magnetic field strength of 68-46 mT), there was a minimal decrease in speed for all angles, defining the optimal working range for vertical locomotion.

The actuation distance exhibited a distinct regressive trend per angle, particularly under steeper sloped conditions. Trials with slope angles of 60° and 75° revealed a loss of magnetic coupling with the RPM below a magnetic field strength of 38 mT. This prevented the protocol from completing three successful runs for each direction.

7.2.2 Comparison of side rolling and ceiling rolling

Investigating the dynamics of side and ceiling rolling on sloped trajectories governed by gradient pulling, the experimental setup replicated the conditions of the previous section. A different cluster, maintaining a nanoparticle concentration of 3 mg/mL, was utilized. The RPM executed lateral and parallel movements relative to the tube, with both the RPM and the cluster rotating in the same plane along a linear trajectory of 110 mm at a speed of 7 mm s^{-1}. The experiment considered inclination angles of 0, 30, and 60 degrees, employing a field strength of 35 mT for a comprehensive examination of side and ceiling rolling dynamics.

The experiment revealed differences in the rolling velocity of the cluster on an inclined surface when employing side rolling or ceiling rolling, as depicted in Fig. 32. Side rolling exhibited higher velocities at less inclined surfaces, including angles of 0 and 30 degrees. However, for more inclined slopes, ceiling rolling became more dominant, showing a positive relation between rolling velocity and inclination. In contrast, side rolling indicated a declining trend with increased slope angles.

Figs. 32(c) and 32(d) illustrate the behavior of ceiling rolling and side rolling for the top branch of the trifurcation phantom oriented in a vertical position. Ceiling rolling demonstrated a faster trajectory compared to side rolling, confirming the results found in the 1-D environments. The side-rolling trajectory took 74 seconds, initiating upon movement in the starting branch and concluding upon stationary rolling. In contrast, ceiling rolling completed the trajectory in 26 seconds, maintaining near-consistent rolling behavior throughout.

7.3 Motion control using X-ray-guided magnetic fields

7.3.1 Navigation in a trifurcation Phantom

To explore the 3D control of IRONSperm clusters in a confined space, a trifurcation phantom filled with a 0.9% saline solution is utilized. The phantom, measuring 140 mm by 125 mm, consists of a furcation with three distinct cylindrical branches, each having inner and outer diameters of 9.5 mm and 14 mm, respectively. The objective of this experiment is to establish a proof of principle by demonstrating successful navigation of a cluster toward all three branches of the phantom in both horizontal and vertical orientations. Two different 3 mg/mL IRONSperm clusters were employed for these trials.

The phantom is positioned in two different orientations. In the $\boldsymbol{xy}$-plane orientation, only ceiling rolling is employed, while both side and ceiling rolling are used in the $\boldsymbol{yz}$-plane orientation. The cluster is navigated into each branch by synchronizing with a complementary RPM trajectory. Occasionally, the RPM direction is altered during a trial to keep the cluster in close proximity to the RPM. Successful proof of the cluster rolling into the intended branch is considered, quantifying the open-loop response of such robot trajectories. Each branch undergoes at least three successful trials to substantiate the proof of principle, and the paths are recorded using a camera. For each branch and orientation, one successful trial is captured using X-ray

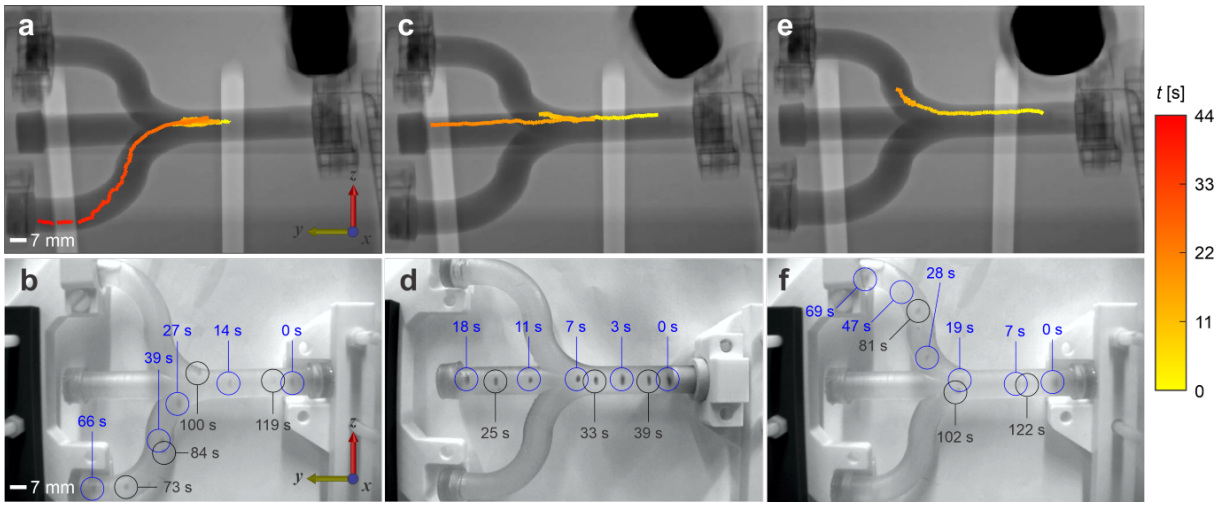

Fig. 34: *X-ray-Guided Control of IRONSperm Cluster is achieved in the Lower (a)-(b), Middle (c)-(d), and Upper Branches (e)-(f) inside a Trifurcation Phantom. X-ray fluoroscopy images are used to localize the cluster during each motion control trial, and simultaneously the video captures complete trifurcation trials (bottom). Blue ellipses depict forward movement, and black ellipses represent backward movement.*

Fluoroscopy images from a Siemens Artis Pheno C-arm system. For vertical trials, only the side-rolling approach will be used to avoid collisions with the phantom and detector of the imaging system.

Control mechanisms demonstrated in previous sections were applied to investigate the behavior in the trifurcation phantom. Figs. 33(b), 33(d), and 33(f) illustrate a proof of principle of forward motion of the cluster into the left, middle, and right branches. The middle branch proved to be the quickest trajectory with a total time of 18 seconds. The left branch showed an uncompleted trajectory due to a present obstruction inside the phantom, but the cluster was able to move past the junction point successfully. The right branch indicated misalignment of the cluster and the RPM, causing it to lose magnetic coupling. The trajectory was completed after regaining coupling with the RPM; however, this significantly reduced the cluster's velocity. This is evident in Fig. 33(b) and Fig. 33(f) as it took the cluster 12 seconds to move past the junction in the left trajectory, while the right trajectory required approximately 49 seconds to reach the same point. For the $\boldsymbol{yz}$-plane, the middle branch (Fig. 34(d)) showed the quickest trajectory with a time of 18 seconds, as this trajectory was the shortest of the three. The lower branch trial (Fig. 34(b)) appeared to be slightly quicker than the top branch (Fig. 34(f)) trial with total forward trajectory times of 66 and 69 seconds, respectively. The clusters remained magnetically coupled for all trials, showing no falling or slipping behavior. This resulted in close cluster to RPM tracking for all branches using the side-rolling approach.

7.3.2 X-ray flouroscopy imaging validation

To validate the investigated behavior using medical imaging modalities, the trajectory rolling was assessed in the trifurcation phantom under X-ray guidance. The trajectories of the traveled paths are visualized over time in Figs. 33 and 34, indicated by the gradient line transitioning from red to yellow. Instead of the typical trailing behavior of IRONSperm clusters, numerous trials showed the clusters rolling in front of the RPM. Clusters performed delayed movements with respect to the RPM. Switching of RPM rotation direction was performed to keep the cluster within a predictable distance of the RPM, showing an oscillating behavior in Figs. 34(d) and 34(f). The X-ray fluoroscopy images for the top branch were obstructed by the RPM, preventing their inclusion in the figure. However, it is noteworthy that despite this limitation, the cluster successfully completed its intended trajectory toward the distal end of the branch.

7.4 Discussions

Assuming negligible differences between the two distinct clusters employed for experimentation within the phantom, their robustness and size (approximately 1.5×10^{-2} and 7.5×10^{-2} mm^3) exerted a significant influence on rolling behavior. This impact compromised the repeatability of the experiments and raised concerns regarding the relevance of cluster characterization. Performance remained relatively constant within the same vessel, but susceptibility to entanglement with waste and particles occasionally hindered the performance of control. Noticeable size and shape differences between the clusters resulted in varied responses to trajectories and actuation distances. The larger cluster responded better to the RPM, demonstrating resilience to discontinuities in the rolling surface and being easier to localize using X-ray Flouroscopy imaging. Conversely, this cluster was prone to decompose and leave a trail of separated clusters. Smaller clusters in proximity affected the main cluster's rolling behavior, influencing results significantly. Comparisons between experiments are cautioned, and the focus should be on cluster control and standardization of fabrication, making the clusters more stable and structurally rigid, rather than characterization. The effect of cluster size on stability during rolling locomotion, maneuverability, and velocity remains to be studied.

This chapter delved into exploring vertical locomotion methods for IRONSperm, emphasizing the unique challenges presented by the confined joint space of the robotic arm. The intricacies of optimizing RPM trajectories for successful open-loop control paths within the trifurcation phantom revealed notable constraints. The manual alignment of the RPM and the phantom posed challenges in identifying an optimal trajectory. Nevertheless, once a successful trial was recorded for a specific trajectory, subsequent trials in the same branch demonstrated a high probability of replication. This observation suggests the potential efficacy of an open-loop control scheme for IRONSperm. To further improve this approach, the research recommends streamlining the process of identifying successful trajectories. The importance of magnetic field strength emerged as a critical factor for precise cluster control, prompting the suggestion to explore variations in this parameter throughout the trajectory.

While this chapter primarily focused on understanding IRONSperm behavior on positively inclined surfaces, there is a recognized need for additional exploration into descending motions. The gravitational force's influence often resulted in the cluster temporarily disconnecting from the RPM, requiring manual RPM directional control and real-time visualization to provide corrective actions through direct teleoperation. Future work should focus on refining trajectories to achieve accurate cluster-to-RPM synchronization, thereby enhancing the clinical applicability of the control method.

References

[1] U. Matulonis, A. Sood, L. Fallowfield, *et al.*, "Ovarian cancer," *Nat Rev Dis Primers*, vol. 2, p. 16061, 2016.

[2] F. Amant, P. Moerman, P. Neven, D. Timmerman, E. Van Limbergen, and I. Vergote, "Endometrial cancer," *The Lancet*, vol. 366, no. 9484, pp. 491-505.

[3] F. Reid *et al.*, "The world ovarian cancer coalition every woman study: identifying challenges and opportunities to improve survival and quality of life," *International Journal of Gynecological Cancer*, vol. 31, pp. 238-244, 2020.

[4] P. Morice *et al.*, "Endometrial cancer," *The Lancet*, vol. 387, pp. 1094-1108, 2016.

[5] J. Li *et al.*, "Biohybrid micro- and nanorobots for intelligent drug delivery," *Cyborg Bionic Syst.*, 2022.

[6] S. Nocentini *et al.*, "Optically driven soft micro robotics," *Adv. Opt. Mater.*, vol. 6, 2018.

[7] N. Pellicciotta *et al.*, "Light controlled biohybrid microbots," *Adv. Funct. Mater.*, vol. 33, 2023.

[8] L. Sun *et al.*, "Biohybrid robotics with living cell actuation," *Chem. Soc. Rev.*, vol. 49, no. 12, pp. 4043-4069, 2020.

[9] F. Iberite, L. Vannozzi, and L. Ricotti, "Biohybrid microrobots," *Springer International Publishing*, 2022.

[10] Y. Alapan, O. Yasa, B. Yigit, I. C. Yasa, P. Erkoc, M. Sitti, "Microrobotics and microorganisms: biohybrid autonomous cellular robots," *Annual Review of Control, Robotics, and Autonomous Systems*, vol. 2, no. 1, pp. 205-230, 2019.

[11] S. Zhu, *et al.*, "Biohybrid magnetic microrobots: An intriguing and promising platform in biomedicine" *Acta Biomaterialia*, vol. 169, pp. 88-106, 2023.

[12] L.-J. W. Ligtenberg, I. A. A. Ekkelkamp, F. Halfwerk, C. Goulas, J. Arens, M. Warle, and I. S. M. Khalil, "Helical propulsion in low-Re numbers with near-zero angle of attack," in *Proceedings of the IEEE International Conference on Intelligent Robots and Systems (IROS)*, Detroit, Michigan, USA, October 2023.

[13] P. Ryan and E. Diller, "Magnetic Actuation for Full Dexterity Microrobotic Control Using Rotating Permanent Magnets" in *IEEE Transactions on Robotics*, vol. 33, no. 6, pp. 1398-1409, Dec. 2017.

[14] K. I. N. A. Middelhoek *et al.*, "Drug-Loaded IRONSperm Clusters: Modeling, Wireless Actuation, and Ultrasound Imaging," *Biomedical Materials*, vol. 17, no. 6, 2022.

[15] V. Magdanz, J. Cumming, S. Salamzadeh, S. Tesselaar, L. Alic, L. Abelmann, I. S. M. Khalil, "Influence of nanoparticle coating on the differential magnetometry and wireless actuation of biohybrid microrobots", in *Proceedings of the IEEE International Conference on Intelligent Robots and Systems (IROS)*, Detroit, Michigan, USA, October 2023.

8 Sperm Cell Empowerment: X-Ray-Guided Magnetic Fields for Enhanced Actuation and Localization of Cytocompatible Biohybrid Microrobots

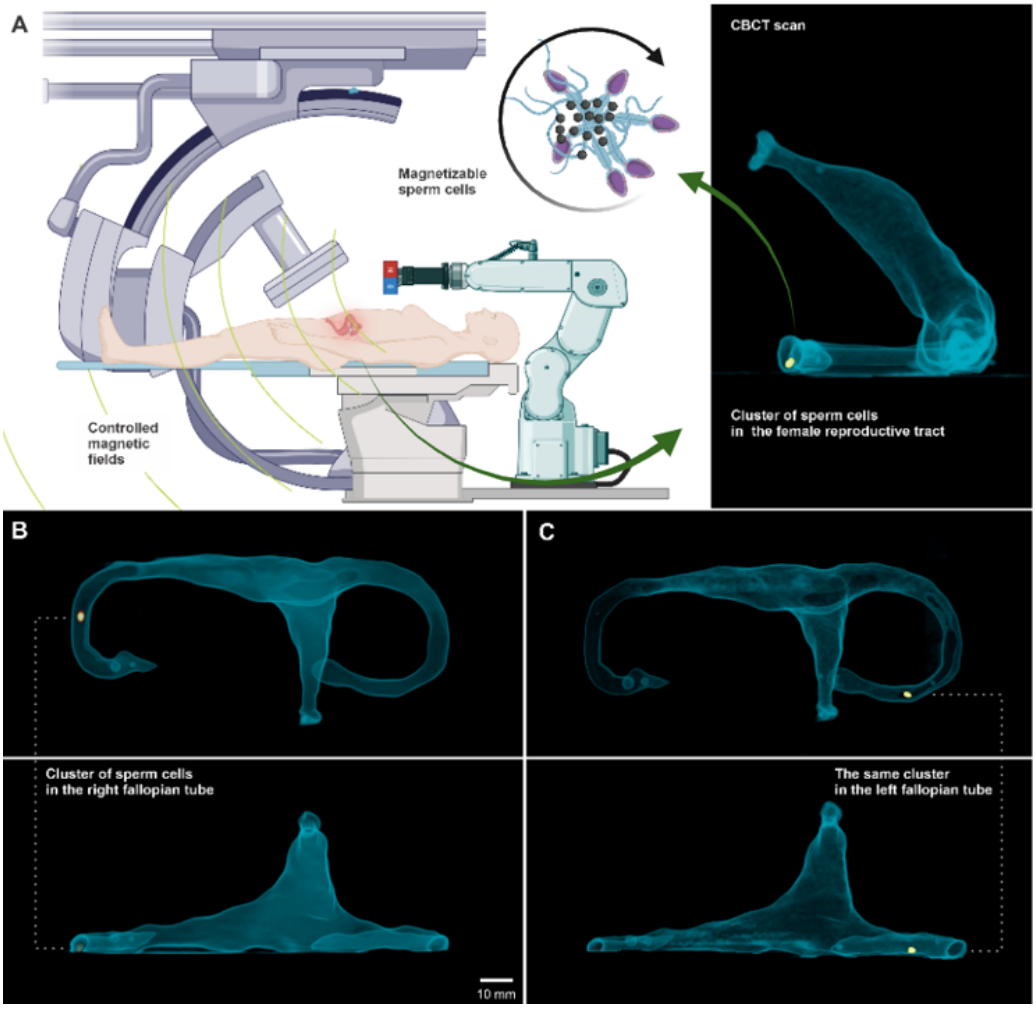

Fig. 35: *Sperm-based biohybrid microrobots targeting minimally invasive treatment of the female reproductive tract with weak, low frequency, controlled external magnetic fields and CT imaging for localization of the magnetizable sperm cell clusters. (**A**) Right: A cluster of nanoparticle-coated sperm cells is clearly visible in the CBCT scans of the female reproductive tract phantom and located in the right (**B**) and left (**C**) fallopian tube. The phantom was reconstructed from MRI images of the reproductive tract and represents the three-dimensional anatomical features of the organ in real size. The sperm cluster can be precisely controlled, responding to the influence of the external rotating magnetic fields within the female reproductive tract, rendering them detectable and controllable within the reproductive tract for potential applications in assisted fertilization or targeted therapy for uterine or oviduct diseases.*

In recent years, soft biohybrid microrobots have emerged as a promising technology with significant potential in various biomedical applications, including drug delivery [1, 2] and assisted fertilization [3]. These microrobots represent a fusion of biological cells and artificial components, capitalizing on the advantages of naturally evolved organisms in conjunction with cutting-edge technologies to address a wide range of biomedical challenges. Notable characteristics of these microrobots include their capability for wireless actuation in response to external stimuli and their excellent biocompatibility. Given their potential for *in vivo* applications, it is crucial that these microrobots can be both remotely controlled and detected using various imaging modalities. A variety of imaging techniques have been utilized for microrobot localiza-

tion, including optical [4], magnetic [5], computed tomography [6], photoacoustic [7], electrical impedance tomography [8], and pulse-echo [9] techniques, each presenting unique advantages and limitations [10]. Among these methods, magnetic-based techniques and computer tomography are advantageous because the former can be used for simultaneous actuation and localization for ferromagnetic field-driven microrobots, while the latter provides an unobstructed workspace between its emitter and detector, allowing for the incorporation of a wireless manipulation system [11]. So far, there has not been any demonstration of simultaneous wireless actuation and localization of torque-driven biohybrid microrobots using an imaging system scalable to the size of *in vivo* applications, for two key reasons. First, this limitation arises from the fact that magnetic-based localization methods, such as MRI, solely permit control over the magnetic field gradient. This constraint limits the use of this imaging system for actuating and localizing ferromagnetic torque-driven microrobots [12]. Hence, it is crucial to generate the actuating magnetic field without interfering with the imaging signal. Second, the amount of artificial components that can be incorporated into an organism is fundamentally limited, either by its size or its surface charge. This, in turn, restricts the acoustic impedance and the absorption of radiation by the radiolucent component of the biohybrid microrobot, as observed in pulse-echo and computer tomography techniques, respectively. The ratio of inorganic to organic matter within the biohybrid microrobot is likely to enhance its magnetic response and detectability while potentially compromising its cytocompatibility.

To ensure cytocompatibility and imaging capability, it is essential to synergistically fuse biological cells and artificial elements, yielding a distinct response unattainable through natural or synthetic means alone [13]. Consider, for example, a cluster of sperm cells that needs to be controlled inside the female reproductive tract during assisted fertilization or loaded with drugs for targeted therapy. *In vivo* localization of the cells can only be achieved by incorporating nanoparticles that provide a detectable signal. In Fig. 35, CBCT scans of a female reproductive tract phantom demonstrate an untethered cluster of nanoparticles-coated sperm cells, allowing for controllable movement and localization by attenuating radiation. If necessary, the cluster can navigate inside the reproductive tract and move toward either the right fallopian tube (Fig. 35B) or the distal end of the left fallopian tube (Fig. 35C). Leveraging the inherent flexibility of sperm cells and incorporating nanoparticle coatings enables magnetic manipulation and enhances acoustic impedance [14, 15, 16].

Here, we address three significant challenges faced by biohybrid microrobots that directly impact the localization and wireless actuation of sperm cells *in vivo*. First, for noninvasive localization using X-ray Fluoroscopy images or ultrasound images, the microrobots must attenuate radiation or reflect the ultrasound waves, respectively. We employ an electrostatic-based self-assembly process to coat sperm cells with different concentrations of nanoparticles. The role of the nanoparticles is twofold: to absorb radiation during X-ray-guided wireless manipulation (Fig. 36A) and to reflect mechanical waves during preliminary imaging using pulse-echo techniques. These two non-invasive imaging methods are implemented using clusters of biohybrid microrobots, as shown in Fig. 31A, because the spatial resolution of modern imaging systems does not allow for the localization of a single cell ($\sim$ 70-µm-long and $\sim$ 5 in width). Second, we investigate the effect of nanoparticle concentration on cytotoxicity of the coated sperm cells. Third, we demonstrate wireless X-ray-guided 3D motion control inside a fluid-filled human reproductive tract model controlled rotating magnetic fields. The advantage of this actuation method, in contrast to magnetic-based techniques such as MRI systems, lies in our ability to precisely project any desired magnetic torque. This enables the control of ferromagnetic torque-driven microrobots while effectively managing the magnetic force to assist in propulsion. In this case, a cluster of coated sperm cells is torque-driven. A rotating magnetic field applied about the long axis of the cluster enables the cluster to rotate, providing rolling locomotion.

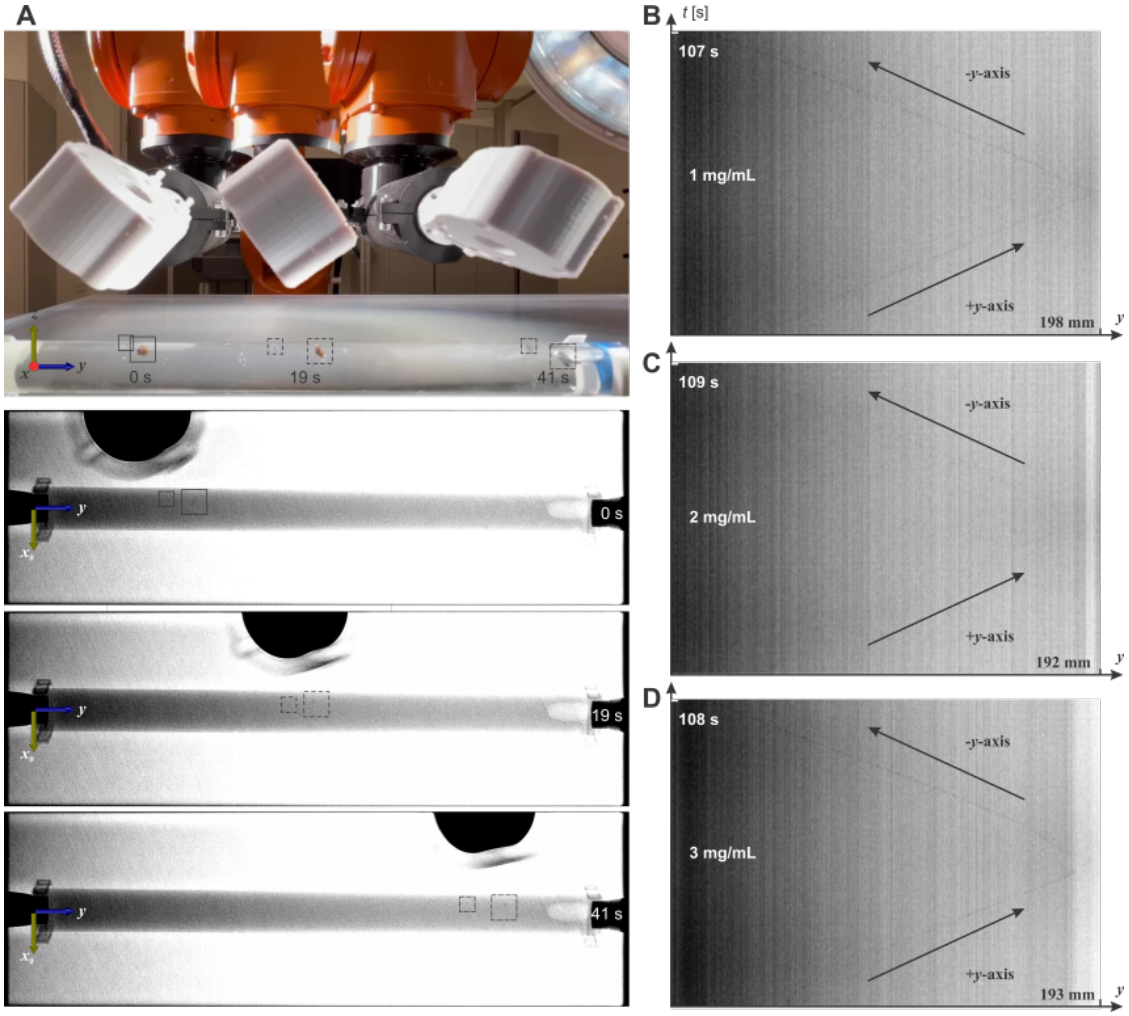

Fig. 36: *Biohybrid microrobots (nanoparticles-coated sperm cells) are actuated using a rotating magnetic fields and localized using X-ray Fluoroscopy images. Increasing the concentration of the nanoparticle coating improves the magnetic response, clustering effect and thereby detectability. (**A**) Two clusters are actuated and localized simultaneously using a rotating magnetic field about the **x**-axis, yielding rolling along the **y**-axis. (**B**)-(**D**) Clusters with nanoparticles concentrations ranging from 1 to 3 mg/mL are detectable using X-ray Fluoroscopy images.*

8.1 Localization of IRONSperm clusters

Each concentration of nanoparticles, from low (1 mg/mL) to medium (2 mg/mL) to high (3 mg/mL), of magnetically coated biohybrid microrobots was placed inside a transparent perspex tube, filled with 0.9% saline, having an inner diameter of 10 mm and an outer diameter of 15 mm. A rotating magnetic field was generated using a cylindrical magnet (NdFeB Grade-N45) with dimensions of 17.5 mm in radius and 20.0 mm in height, positioned 50 mm above each sample. This configuration resulted in a maximum field strength of 28 mT.

The generated magnetic field resulted in a rolling motion of the IRONSperm clusters, depending on a nearby solid boundary, as shown in Fig. 36A. A cluster of cells with magnetic particles is more practical for medical imaging. As the X-ray beam passes through the coated and entangled cells, its intensity diminishes. This attenuation occurs as the X-rays travel from the source to the detector array, enabling us to visualize the cluster, its surroundings, and its actuating permanent magnet. Fig. 36 shows the rolling motion of the cluster along the ***y***-axis and three representative X-ray Fluoroscopy images captured at Fluoroscopy dose rate of 30.8 $\text{mGy}\cdot\text{cm}^2\cdot\text{s}^{-1}$. In this experiment, the RPM is controlled robotically to translate above the fluid-filled lumen at a translational speed comparable to that of the rolling cluster. As the

Table 3: *The influence of the ratio of nanoparticles (NP) per biohybrid cluster on the localization of the entangled sperm cell clusters and cell cluster cytotoxicity. The localization has been quantified by determining the contrast to noise ratio (CNR)*

	CNR		**Cytotoxicity**	
NP	US	X-ray	XTT [%]	Viability [%]
1 [mg/mL]	3.41 ± 1.56	0.89 ± 0.29	95.1 ± 1.0	99 ± 0.1
2 [mg/mL]	2.50 ± 0.59	0.53 ± 0.37	89.9 ± 1.6	97 ± 3
3 [mg/mL]	4.22 ± 1.06	1.10 ± 0.46	89.4 ± 1.8	89 ± 14

permanent magnet translates and rotates to keep the cluster coupled with the rotating magnetic field, we measure the CNR of clusters with nanoparticle concentrations of 1-3 mg/mL. Each motion control trial involves the cluster rolling forward using clockwise rotation of the permanent magnet about the $\boldsymbol{x}$-axis and then rolling backward to the starting point using counter-clockwise rotation. Note that the source-detector-axis of the C-Arm is rotated by 20° with respect to the $\boldsymbol{z}$-axis in the frame of reference depicted in Fig. 36A. This rotation enables unobstructed motion of the actuator magnet above the fluid-filled lumen during X-ray-guided actuation of the sperm cell clusters. The forward and backward rolling motion of a cluster with a nanoparticle concentration of 1 mg/mL is illustrated in Fig. 36B. This trajectory forms an isosceles triangle when the contrast is measured over time. The contrast shifts with time as the cluster rolls along the $+\boldsymbol{y}$-axis. When the direction of rotation of the actuator magnet is reversed, the slope of the line becomes negative, indicating motion reversal along the $-\boldsymbol{y}$-axis. Similar response is observed for clusters with nanoparticle concentrations of 2 and 3 mg/mL, as shown in Figs. 36C and 36D, respectively. This result demonstrates that the cluster's structure is adequately dense to absorb sufficient radiation at any of the 3 tested concentrations, facilitating effective localization.

To quantify the visibility of each cluster, we determined the Contrast to Noise Ratio (CNR) of biohybrid microrobots, we identified Regions of Interest (ROI) in various frames of the fluoroscopy video, isolating specific areas within the rolling sample contained within a tube and distinguishing them from the background noise within the tube. The CNR was then calculated using the following equation:

$$\mathrm{CNR} = \frac{|S_S - S_B|}{\sigma_B}, \tag{15}$$

where S_S represents the mean X-ray absorbance value value of the sample's ROI, S_B represents the mean X-ray absorbance value value of the background's ROI, and σ_B stands for the standard deviation of the background's ROI. For the ultrasound CNR assessment, the rolling clusters were visualized using a Siemens Acuson 14L5 probe, and the CNR was calculated using the grayscale values from the resulting video footage for each ROI.
From the analysis described above, followed that the highest concentration of nanoparticles shared the highest CNR for both X-ray imaging and ultrasound visualization, Table 3. These results suggest that this concentration would be most suitable for localization during X-ray-guided 3D motion control experiment.

8.2 Cytotoxicity assessment of nanoparticle concentrations

To assess cell viability and metabolic activity of 3T3 fibroblast cells when in contact with sperm-based biohybrid microrobots, XTT assays (RandDsystems- Catalog Number: 4891-025-K) were preformed based on the following protocol. Three replicates were performed for each assay. For each experimental run, the volumes of medium, XTT reagent, and activation solution were calculated as 8.68 mL, 4.34 mL, and 86.8 µL respectively following the manufacturer's recommendations. The medium, XTT reagent, and activation solution were kept at 4°C until use. The 24-well plate of cultured fibroblast cells were labelled accordingly. All four samples

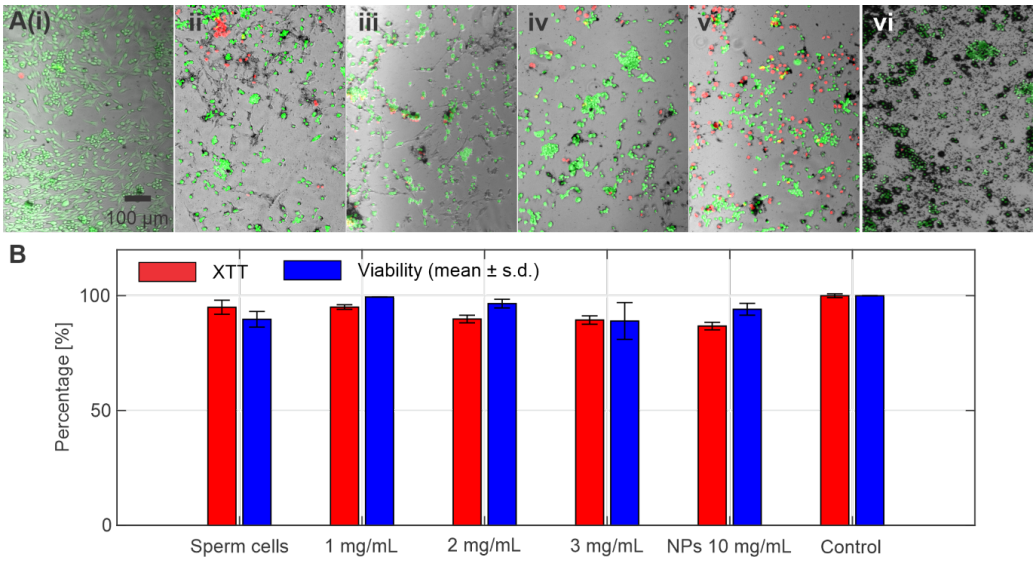

Fig. 37: *Toxicity studies show that the magnetic content has no significant impact on fibroblast viability across the various samples. (**A**) Live/dead staining of fibroblasts incubated for 24 hr with increasing concentrations of iron oxide nanoparticles on bull sperm (from left to right), performed by the use of Calcein (green stain, live cells) and Propidium Iodide (red, dead cells). (i) Control sample with only fibroblasts, (ii) Bull sperm (iii) Sperm-based biohybrid robots with 1 mg/mL of iron oxide nanoparticles. (iv) Sperm-based biohybrid microrobots with 2 mg/mL of iron oxide nanoparticles. (v) Sperm-based biohybrid microrobots with 3 mg/mL of iron oxide nanoparticles.(vi) 10 mg/mL of pure iron oxide nanoparticles. Scale bar: 100 µm. (**B**) Sperm-based biohybrid microrobots' cytotoxicity on Fibroblast Cells, measured by XTT assay with average relative corrected absorbance normalized to the control (red), and fibroblast live/dead viability staining (blue) evaluated after 24 h incubation with sperm-based biohybrid microrobots.*

contain 400 µL of sperm-based biohybrid microrobots solution. A volume of 100 µL of sample 1 was distributed across three individual wells each. This was replicated for the remaining 3 samples and their respective wells. A volume of 100 µL of nanoparticles solution was poured into 3 empty wells each. The remaining 4 wells were left as controls. After filling the well-plate, it was incubated at 37°C for 21.5 hr. After, a 15 mL tube was covered in aluminum foil. The medium, XTT reagent, and activation solution were thawed in a water bath, and aliquoted in 1.5 mL tubes. The required volumes of medium, reagent, and activation solution were mixed thoroughly in the 15 mL tube. The solution was then ready to add to the cells. The plate of cells was removed from the incubator to aspirate the media using a pipette and dispensing into a waste tube. Activated XTT solution (0.5 mL) was introduced into each tube well. The well plate was incubated for 2.5 hr. Subsequently, the absorbance was measured. In the biosafety cabinet (BSC), a 96-well plate was prepared with 2 wells/disc. From each disc, 150 µL of XTT-solution was transported into the respective well on the 96-well plate (running each disc in duplicates). This was done carefully to ensure no bubbles are present. The absorbance was measured using a microplate reader and the SoftMax software. This protocol measures the absorbance at 690 and 450 nm wavelengths. The absorbance data was analyzed by the use of the following formula: Relative Corrected Abs = *Sample Abs. 450 − Sample Abs. 690.* The duplicates average was calculated to create a reading. This data was presented in a bar chart (Fig. 37B). Following the XTT assay, a live/dead staining procedure was conducted on the fibroblast to further evaluate cell viability. The 24-well plate was incubated at 37°C until use. Calcein and propidium iodide (PI) dye were prepared from the solid dye powder. To create a 1 mg/mL solution for live staining, 1 mL of Dimethyl sulfoxide (DMSO) was added directly to 1 mg of calcein powder. To create a 2 mg/mL solution for dead staining, 1 mL of DMSO was added directly to 2 mg of PI. Into each well, 1 µL of PI and 1 µL of calcein stock solution was added. The tray was incubated in the dark at 37°C for 5 minutes. A brightfield microscope was used for imaging where green

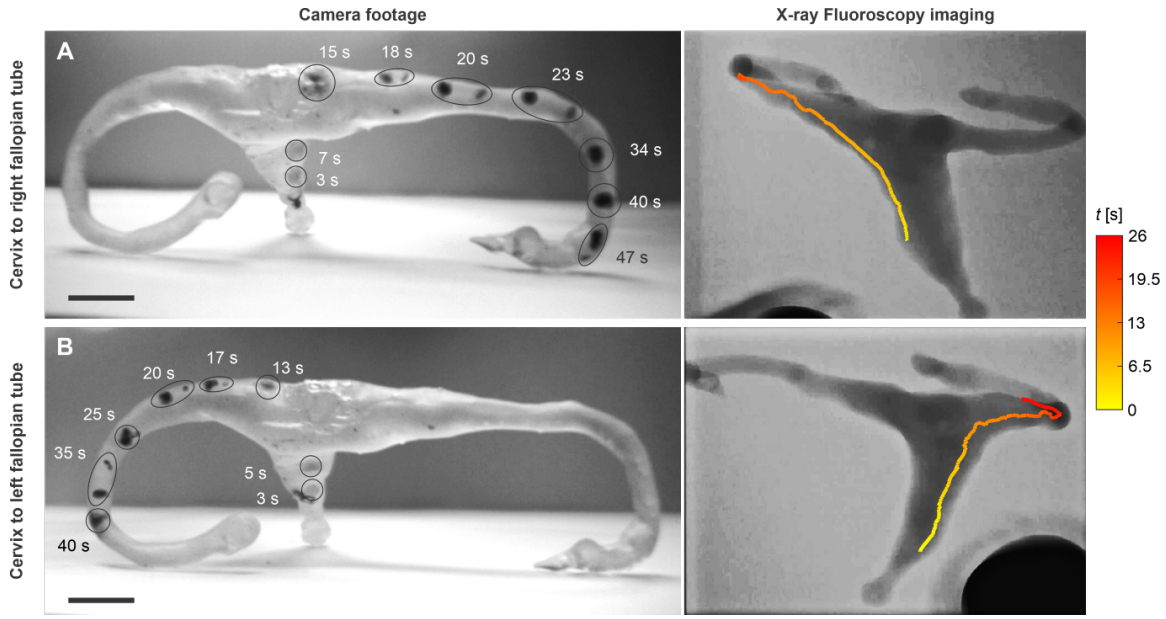

Fig. 38: *Trajectory evolution over time visualized through camera footage (left) and X-ray Fluoroscopy imaging (right). Ellipses illustrate the positions, within specific timeframes, of all components linked to the primary cluster when separated. (**A**) The top images depict trajectories within the right fallopian tube. (**B**) The bottom images represent the left fallopian tube.*

fluorescent protein microscopy was used for live staining and red fluorescent protein microscopy for dead staining at 10x magnification (Fig. 37A). The cell viability was calculated in percent by dividing the number of live cells by the sum of live and dead cells. The results were presented in a bar chart (Fig. 37B). Statistical analysis was performed in Originlab software with an ANOVA test with Bernoulli condition and delivered insignificant differences between the samples and control for the live/dead stains ($p > 0.11$ for all cases), and only small deviations for the XTT assay.

Both toxicity studies confirm that the magnetic content has no significant impact on fibroblast viability across the various particle concentrations, Table 3. Exposure to 1, 2, and 3 mg/mL sperm-based biohybrid microrobots reduced cell viability by 5%, 10%, and 11%, respectively, as confirmed by XTT assays. Live/dead staining of fibroblasts demonstrated no toxicity at 1 mg/mL, and only 3% and 10% at 2 and 3 mg/mL of magnetic nanoparticle concentration, but no statistically significant difference ($p = 0.11$ and $p = 0.12$, respectively). The sample involving 10 mg/mL pure magnetic nanoparticles exhibited increased toxicity by 13% and 6% compared to the control, respectively, as evidenced by the two cytotoxicity assays. Interestingly, pure sperm samples also resulted in a reduction in fibroblast viability, with a decrease of 5% (XTT) and 10% (live/dead). This phenomenon could be attributed to residues of cryopreservant or pathogens present in the semen, which may not be entirely removed during sperm preparation. It is also noteworthy that the cytotoxicity of the sperm-based magnetic microrobots is comparable to that of pure sperm samples, suggesting that significant toxicity does not originate from the magnetic nanoparticles.

8.3 Motion control inside female reproductive tract model

8.3.1 Female reproductive tract model fabrication and imaging

MRI data, obtained from The Cancer Imaging Archive, served as the reference dataset for model development. The outer muscular layer of the uterus, known as the perimetrium, was segmented using 3D Slicer. To accurately represent the uterine cavity, a 2D image was superimposed to capture its overall shape. Subsequently, mean measurements were researched, including

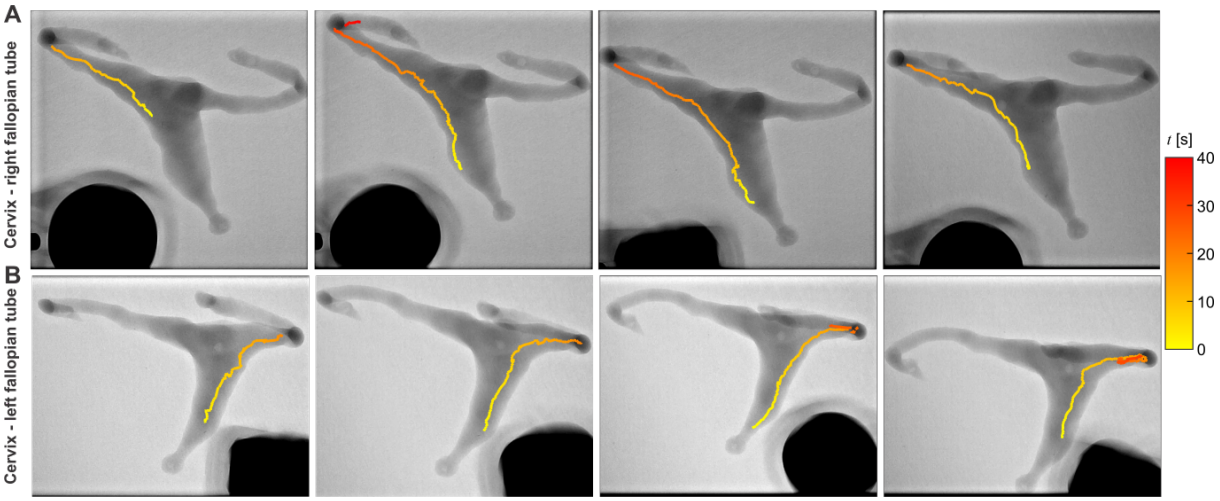

Fig. 39: *Biohybrid microrobots are precisely navigated within the female reproductive tract using X-ray-guided magnetic fields. (**A**) Motion control trials demonstrate nanoparticle-coated sperm cells starting from the cervix and rolling toward the right fallopian tube. (**B**) To move sperm cells from the cervix toward the left fallopian tube, modifications are made to the magnetic fields, enabling rolling motion along its path.*

parameters such as thickness, width, length, and circumference, to refine the digital phantom. The model's optimization and hollowing were achieved using Meshmixer, ensuring its suitability for 3D printing on the Form3 resin printer with Elastic 50A resin. Following the printing process, a series of post-processing steps were performed. These steps included a 20-minute ethanol wash, the application of a thin layer of Elastic 50A resin to enhance transparency, ethanol flushing to remove any residual resin, a 20-minute curing period, and the removal of support structures.

To visualise the female reproductive tract model with the biohybrid magnetic microrobot clusters a Siemens Healthineers Artis Pheno system was used. First the reproductive tract model was filled with 0.9% saline and a biohybrid microrobot cluster. Subsequently the microrobot cluster was manually guided towards its desired locations. Once in position, the model was imaged using a CBCT scan. Following the scanning process, the reproductive tract model was reconstructed with a specific window for the Hounsfield values, such that both the reproductive tract model and the biohybrid magnetic microrobot cluster are easily distinguishable (Figs. 35A and 35B).

8.3.2 Motion control performance evaluation

Biohybrid microrobots traverse the 3D printed female reproductive tract model using controlled rotating magnetic fields, initiated from the cervix and directed towards the right or left fallopian tube (Fig. 38). In this experiment, biohybrid microrobots, with a nanoparticle concentration of 3 mg/mL magnetize the sperm cells, while the reproductive tract is filled with a 0.9% saline solution. Fig. 38A illustrates the rolling behavior from the cervix towards the distal end of the right fallopian tube, using the centerline of the pathway to determine the magnetic field rotation axis as the cluster rolls inside the phantom. The motion of the cluster is simultaneously tracked using camera footage and X-ray Fluoroscopy images. At an actuation frequency of 1.5 Hz, the cluster rolls from the cervix toward the bifurcation points of the fallopian tubes under an inclination. At the bifurcation point ($t = 15$ s in Fig. 38A and $t = 13$ s in Fig. 38B), the rotating permanent magnet is robotically controlled to rotate the field rotation axis along the centerline of the right fallopian tube, guiding the microrobots along this path while rolling. As the biohybrid microrobots roll past the bifurcation point ($t > 15$ s), the configuration becomes more planar, and the average rolling speed increases from 3 mm/s to 6 mm/s. Finally, the field-gradient pulling is removed which allows for controlled vertical displacement along the negative

z-axis. The rotating magnetic field still exerts torque on the cluster during this manoeuvre, enabling the microrobots to reach the distal end of the right fallopian tube in 47 s. Similar to the motion control in the right fallopian tube, the biohybrid microrobots are precisely guided from the cervix toward the left fallopian tube, as depicted in Fig. 38B, completing the journey in 37 seconds at an average rolling speed of 3.5 mm/s up until the descending point of the fallopian tube. Notably, as the cluster rolls toward the left or right fallopian tubes, it breaks into smaller clusters. The ellipses in Fig. 38 indicate the clusters when separated. Nevertheless, the smaller clusters remain coupled with the actuating magnetic field and rotate in sync. Although this behavior can potentially impact the detectability of the cluster in the X-ray Fluoroscopy images, we were able to obtain enough contrast, enabling the automatic detection of the cluster throughout the entire path. Motion control inside the reproductive tract model was repeated for a total of successful 5 trials in each fallopian tube, Fig. 39, proving the high potential of the measure of controllability that these microrobots possess. Imaging using X-ray fluoroscopy showed difficulty in the distal end due to reduced CNR, mostly showing no trace of cluster locomotion in Fig. 39. Nonetheless, the clusters were able to reach the distal end in each trial in less than 50 seconds.

8.4 Discussion

This chapter represents a significant milestone in the development and assessment of biohybrid microrobots tailored for applications within the reproductive tract. Our innovative approach of coating sperm cells with magnetic nanoparticles has not only resulted in enhanced mobility, but it has also unveiled a transformative aspect - the potential for real-time visualization of sperm cells using X-ray Fluoroscopy images. While investigating the detectability of these microrobot clusters in medical imaging, we identified that the increased concentration of the nanoparticles yields a slight improvement in detection in both ultrasound and X-ray Fluoroscopy images. Furthermore, our cytotoxicity assessments indicate that the incorporation of magnetic nanoparticles does not introduce substantial harm to cells. This result, particularly in the context of X-ray imaging, underscores the promise of these biohybrid microrobots for precise medical interventions, including drug delivery and diagnostic applications in the female reproducive tract. With the ability to visualize and control sperm cells using X-ray-guided platform, this research paves the way for transformative medical procedures and therapies, ushering in a new era of reproductive medicine with profound implications for patient care and scientific progress.

References

[1] O. Felfoul, M. Mohammadi, S. Taherkhani, and Al., "Magneto-aerotactic bacteria deliver drugcontaining nanoliposomes to tumour hypoxic regions," *Nature Nanotech*, vol. 11, pp. 941-947, 2016.

[2] C. Schmidt, M. Medina-Sánchez, R. Edmondson, and O. Schmidt, "Engineering microrobots for targeted cancer therapies from a medical perspective," *Nature Communications*, vol. 11, pp. 1-18, 2020.

[3] M. Medina-Sanchez, L. Schwarz, A. Meyer, F. Hebenstreit†, and O. Schmidt, "Cellular Cargo Delivery: Toward Assisted Fertilization by Sperm-Carrying Micromotors," *Nano Lett.*, vol. 16, pp. 555-561, 2016.

[4] F. Servant, M. Mazza, K. Kostarelos, and B. Nelson, "Controlled in vivo swimming of a swarm of bacteria-like microrobotic flagella," *Adv. Mater.*, vol. 27, pp. 2981-2988, 2015.

[5] A. Bakenecker, A. Gladiss, H. Schwenke, and Al., "Navigation of a magnetic micro-robot through a cerebral aneurysm phantom with magnetic particle imaging," *Scientific Reports*, vol. 11, pp. 14082, 2021.

[6] F. Bianchi, A. Masaracchia, E. Barjuei, A. Menciassi, A. Arezzo, A. Koulaouzidis, D. Stoyanov, P. Dario, and G. Ciuti, "Localization strategies for robotic endoscopic capsules: a review," *Expert Review Of Medical Devices*, vol. 16, pp. 381-403, 2010.

[7] L. Wang and J. Yao, "A practical guide to photoacoustic tomography in the life sciences," *Nature Methods*, vol. 13, pp. 627, 2016.

[8] H. Daguerre, S. Demir, U. Culha, F. Marionnet, M. Gauthier, M. Sitti, and A. Bolopion, "A localization method for untethered small-scale robots using electrical impedance tomography," *IEEE/ASME Transactions On Mechatronics*, vol. 27, pp. 3506-3516, 2022.

[9] Q. Wang, L. Yang, J. Yu, P. Chiu, Y. Zheng, and L. Zhang, "Real-Time magnetic navigation of a rotating colloidal microswarm under ultrasound guidance," *IEEE Trans. Biomed. Eng.*, vol. 67, 2020.

[10] A. Aziz, V. Pane, N. Koukourakis, J. Czarske, A. Menciassi, M. Sánchez, and O. Schmidt, "Medical imaging of microrobots: Toward in vivo applications," *ACS Nano*, vol. 14, pp. 10865-10893, 2020.

[11] D. Jin, Q. Wang, K. Chan, N. Xia, H. Yang, Q. Wang, S. Yu, and L. Zhang, "Swarming self-adhesive microgels enabled aneurysm on-demand embolization in physiological blood flow," *Science Advances*, vol. 9, pp. eadf9278, 2023.

[12] L. Zhang, J. Abbott, L. Dong, B. Kratochvil, D. Bell, and B. Nelson, "Artificial bacterial flagella: Fabrication and magnetic control," *Appl. Phys. Lett.*, vol. 94, pp. 064107, 2009.

[13] X. Yan, M. Q. Zhou, Y. Deng, J. Yu, J. Xu, T. Xu, T. Tang, L. Bian, Y. Wang, K. Zhang, "Multifunctional biohybrid magnetite microrobots for imaging-guided therapy," *Science Robotics*, vol. 2, pp. eaaq1155, 2017.

[14] V. Magdanz, I. Khalil, J. Simmchen, G. Furtado, S. Mohanty, J. Gebauer, H. Xu, A. Klingner, A. Aziz, M. Medina-Sánchez, O. Schmidt, and S. Misra, "IRONSperm: sperm-templated soft magnetic microrobots," *Science Advances*, vol. 6, pp. eaba5855, 2020.

[15] V. Magdanz, J. Vivaldi, S. Mohanty, A. Klingner, M. Vendittelli, J. Simmchen, S. Misra, and I. Khalil, "Impact of segmented magnetization on the flagellar propulsion of sperm-templated microrobots," *Advanced Science*, 2021.

[16] K. Middelhoek, V. Magdanz, L. Abelmann, and I. Khalil, "Drug-Loaded IRONSperm clusters: modeling, wireless actuation, and ultrasound imaging," *Biomedical Materials*, vol. 17, 65001, 2022.

9 Conclusions

In the presented work, we show significant steps aimed at bridging the gap between untethered magnetic robots (UMRs) and *in vivo* applications. Specifically, we introduce an X-ray-guided teleoperation strategy suitable for 3D motion control of hemocompatible UMRs, whose capabilities are validated *ex vivo* by demonstrating successful navigation and mechanical thrombi size reduction. The localization used for the teleoperation has been achieved using X-ray imaging, with a clinically relevant fluoroscopy dose rate of 0.13 $\text{mGy.cm}^2\text{s}^{-1}$. While this dose rate is clinically acceptable, exposure for a long time can still result in high doses received by the patient. To mitigate this risk, the knowledge of the environment gained with a CBCT scan can be used to minimise the X-ray exposure time, minimizing the radiation absorption of the sample. This can be done by combining the magnetic coupling localisation, as demonstrated by D. Uğurlu [27], where the end-effector's position and vessel structure can be used to estimate the position of the UMR. This results in less frequent X-ray shots which should be sufficient to successfully track the UMR.

The same X-ray scanner was utilized to generate CBCT scans to reconstruct the vessel structure, from which the pose of the RPM can be calculated. Combining this RPM pose together with the actuation frequency of the RPM resulted in a teleoperation strategy. Validation of this teleoperation strategy showed a significant increase in success rate, particularly when steering against the natural drift direction of the UMR, an increase from 20% to 80%. In the future, we plan to give more authority to the teleoperator, such that also the position of the RPM along the vessel trajectory can be controlled. Currently, the RPM pose is controlled in open-loop based on the expected UMR velocity. Introducing this extra teleoperation input should provide the teleoperator with enough control to precisely control a UMR along any vessel 2D structure.

To move the teleoperation method closer to *in vivo* applications, a 3D motion control method using a single RPM has been. Here the magnetic field gradient is used to control the vertical velocity of the UMR. Testing conducted in a physiologically accurate carotid artery phantom demonstrated successful navigation from the common carotid artery into both the external and internal carotid arteries, achieving an average success rate of 89%. However, given the UMR's predominantly negative buoyancy, the UMR required relatively strong external magnetic fields (3 - 5 mT) to achieve gravity compensation. Such strong magnetic fields require smaller RPM-UMR gaps, which might not be achievable in an *in vivo* situation. To address this limitation, we plan to look into increasing the magnetic moment and bouyancy of the UMRs, thereby enhancing the feasibility and adaptability of our teleoperation approach for clinical applications.

Validation of the teleoperation was done by conducting *ex vivo* experiments in a porcine abdominal aorta vessel structure. Where successful navigation has been shown by transitioning between the abdominal aorta and renal arteries, both with and without blood flow. The achieved propulsive thrust of the evaluated UMR designs is sufficient to overcome a pulsatile blood flow of 67.8 mL per minute. In the case of an increasing UMR-to-vessel ratio, the UMR's speed increases while also being more influenced by the blood flow, agreeing with the plug flow model. While it is important to acknowledge that this flow rate deviates significantly from the physiological flow rate of 2.9 L per minute in the abdominal aorta, the results mark a pioneering attempt to controlling torque-driven UMRs against flow inside an *ex vivo* model. Furthermore, only the torque-driven UMR's propulsive thrust has been used to achieve UMR locomotion. In the future magnetic field gradient pulling will be used in combination with the torque driven locomotion to overcome greater flow rates. Increasing the magnetic moment of the UMRs can also result in a higher step-out frequency, which in turn will increase the propulsive thrust and magnetic attraction capabilities. Moreover, as indicated by the plug flow model, there exists a pitch for optimal UMR for a given vessel diameter, indicating that there exists an optimal combination of pitches for each possible UMR task. Exploration of all the above mentioned improvements will be of crucial importance for translation of UMRs towards *in vivo* experiments.

Another important step for UMRs that has been taken in this study is the biocompatibility presented, which demonstrates the feasibility of using coated UMRs for *in vivo* applications. Applying the presented lipid-based coating method, any UMR surface can be made hemocompatible. Importantly, no measurable impact on performance was observed following the application of the coating, facilitating seamless knowledge transfer from uncoated to coated UMRs and streamlining preliminary research. Moving forward, it will be important to investigate the effect of UMR's rubbing on the coating, as any significant decrease in coating effectiveness could necessitate exploration of alternative UMR fabrication methods. Addressing this aspect will be essential for ensuring the long-term viability and functionality of coated UMRs in clinical settings.

This effect could be increased by the thrombus engagement method. Here the UMR is navigated towards a thrombus in *ex vivo* tissue, once arrived at the thrombus the UMR was allowed to rub against a thrombus for 30 minutes, resulting in a degradation of 16%. This pioneering experiment illustrates the potential of using UMRs for treatment of ischemic stroke and other vessel diseases. In our next work, we plan to create more optimised UMRs for mechanical grinding. Additionally, we plan to explore a hybrid strategy that combines chemical lysis along with mechanical grinding. This hybrid approach holds promise for further enhancing the efficacy of UMRs in addressing vascular diseases.

The integration of the presented methods in this study, can result in a UMR teleoperation control method capable of steering UMRs through vessels that currently cannot be reached with a guidewire. Beyond enabling precise delivery of medical drugs throughout the human body, our research has demonstrated that UMRs can serve as effective mechanical tools for engaging with obstructions such as thrombus.

Microscale helical untethered magnetic robots

To further investigate UMR capabilities, we evaluated the control of helical microscale UMRs. We highlight the significant advantage of employing a single RPM to generate a rotating magnetic field as actuation of microscale UMRs. The single part UMR containing ferromagnetic material was actuated at varying RPM-UMR gaps to present the critical influence of this gap. The created model was highly sufficient at determining the RPM-UMR gap at which the UMR would swim with near-zero angle of attack, showing good agreement with the experimentally determined RPM-UMR gap. Swimming with such small angle of attack, not only facilitates entry of narrower confinements, but also directly increases the forward velocity of the UMR, as propulsion no longer needs to be used for gravity compensation [8].

For future work, we plan to translate from a straight line trajectory to full 3D motion control using the same method as with milliscale UMRs, presented in Chapter 3. Moreover, considering that multiple microscale UMRs may need to be actuated simultaneously to achieve a measurable effect [5], our evaluation of the presented control method will involve replicating experiments with simultaneous actuation of multiple microscale UMRs. Additionally, augmenting the number of microscale UMRs could improve their visualization, particularly with medical imaging methods such as X-ray, thereby enabling feedback control or teleoperation for enhanced maneuverability and effectiveness in various medical applications.

Biohybrid untethered magnetic robots

As demonstration of our designed X-ray-guided motion control system, we extended our setup to support rolling biohybrid UMRs. First, we explore X-ray-guided motion control of IRONSperm microrobot clusters, with the aim of identifying the optimal approach for achieving superior robot maneuverability and speed. The conducted experiments reveal that the inclination angle has a minimal impact on rolling velocity, indicating a slight regressive trend with increased actuation distance on sloped surfaces. Notably, ceiling rolling emerges as marginally faster than side

rolling, establishing it as the preferred method for positively angled inclinations, as confirmed in a trifurcation phantom. However, for descending or horizontal branches, side rolling exhibits greater maneuverability. Combining these methods successfully demonstrates 3D locomotion control in the enclosed trifurcation phantom, underscoring the potential for open-loop control in confined spaces.

Second, we introduce control methods of cytocompatible biohybrid UMRs, validated *in vitro* in a physiologically accurate reproductive tract model. Cytotoxicity assessment revealed that none of the tested concentrations were substantially harmful to their surrounding cells, ensuring good biocompatibility of the IRONSperm. Furthermore, an increase in actuation response and detectability was found when using higher nanoparticle concentrations. To demonstrate the possible control of IRONSperm, its performance was evaluated in a 3D human reproductive tract phantom. Here the control and detectability of the IRONSperm clusters allowed us to navigate and track the IRONSperm into both fallopian tubes, of a *in vitro* physiologically accurate reproductive tract model. These novel approaches show the vast potential of using drug-loaded IRONSperm cells for targeted therapy and reproductive medicine.

In future work, the focus should shift toward advancing the control mechanisms of IRONSperm clusters, especially in navigating through complex *ex vivo* tissue environments. The exploration of control strategies within biological tissues poses unique challenges, and research efforts should be directed toward optimizing the UMR's performance in such physiological scenarios (e.g., locomotion against fluid flow). Standardizing the fabrication process becomes even more critical to ensure consistency in performance, stability, detectability in X-ray fluoroscopy images, and maneuverability within varied tissue conditions. Integrating real-time imaging and automated feedback mechanisms into the control system would further enhance precision, paving the way for the clinical implementation of IRONSperm microrobots in medical procedures through direct teleoperation.

Acknowledgements

I extend my gratitude to the following individuals whose invaluable contributions have greatly enriched my research journey.
First and foremost, I want to thanks dr. Islam S. M. Khalil, for his invaluable supervision and helping hand in preparing our papers for publication. Second, I would like to give special thanks to prof. dr. Jutta Arens and dr. Giulio Dagnino for willing to be part of my graduation committee. Third, I thank all the my fellow colleagues, with whom I have had many valuable discussions, special thanks goes to H. Remco Liefers for his invaluable assistance in operating the CBCT scanner, facilitating the visualization of our experiments, Roger Lomme and dr. Michiel Warlé, for their support in realizing the *ex vivo* experiments, Nicole Rabou for her aid in conducting the *in vitro* blood experiments, dr. Dorothee Wasserberg for her assistance in selecting and applying the coatings onto the UMR, Sander Peters and Rob J. Struik for their efforts in conceptualizing and constructing the mobile KUKA station, dr. Constantinos Goulas and dr. Sumit Mohanty for their assistance in fabrication and characterization of the microscale UMR, dr. Anke Klinger for creating the Oldroyd-B model, Luuc de Jongh for his executing experiments with the microscale UMR, dr. Veronika Magdanz and her dedicated team in Waterloo, for the fabrication of the IRONSperm clusters, and Joep K. van der Mijle Meijer and Iris Mulder, for their help in conducting and analyzing the IRONSperm motion control experiments. Finally, I would like to give a warm thanks to my family who have supported me all throughout this journey.

References

[1] K. Kikuchi, et al., "Fabrication of a spiral type magnetic micromachine for trailing a wire," *IEEE Transactions on Magnetics*, vol. 41, no. 10, pp. 4012-4014, 2005.

[2] T. W. R. Fountain, P. V. Kailat, and J. J. Abbott, "Wireless control of magnetic helical microrobots using a rotating-permanent-magnet manipulator," in *Proc. IEEE Int. Conf. Robot. Autom.*, 2011, pp. 576–581.

[3] X. Yan, et al., "Multifunctional biohybrid magnetite microrobots for imaging-guided therapy," *Science Robotics*, vol. 2, no. 12, pp. eaaq1155, 2017.

[4] A. Aziz, et al., "Medical imaging of microrobots: Toward in vivo applications," *ACS Nano*, vol. 14, no. 9, pp. 10865-10893, 2020.

[5] M. Sitti, et al., "Biomedical applications of untethered mobile milli/microrobots," *Proceedings of the IEEE*, vol. 103, no. 2, pp. 205-224, 2015.

[6] T. Xu, et al., "Millimeter-scale flexible robots with programmable three-dimensional magnetization and motions," *Science Robotics*, vol. 4, no. 29, pp. eaav4494, 2019.

[7] A. W. Mahoney and J. J. Abbott, "Managing magnetic force applied to a magnetic device by a rotating dipole field," *Applied Physics Letters*, vol. 99, no. 13, 2011.

[8] J. J. Abbott, et al., "How should microrobots swim?," *The International Journal of Robotics Research*, vol. 28, no. 11-12, pp. 1434-1447, 2009.

[9] L. J. W. Ligtenberg and I. S. M. Khalil, "Input-Output Boundedness of a Magnetically-Actuated Helical Device," in *2023 IEEE International Conference on Robotics and Automation (ICRA 2023)*, 2023, pp. 5433-5438.

[10] L.-J. W. Ligtenberg, I. A. A. Ekkelkamp, F. R. Halfwerk, C. Goulas, J. Arens, M. Warlé and I. S. M. Khalil, "Helical Propulsion in Low-Re Numbers with Near-Zero Angle of Attack," in *Proc. IEEE Int. Conf. Intelligent Robots and Systems.*, 2023, pp. 2647-2652.

[11] E. E. Niedert, et al., "A tumbling magnetic microrobot system for biomedical applications," *Micromachines*, vol. 11, no. 9, pp. 861, 2020.

[12] M. Vonthron, et al., "A MRI-Based integrated platform for the navigation of microdevices and microrobots," in *Proc. IEEE J. Int. Conf. Intell. Robots Syst.*, pp. 1285-1290, 2011.

[13] M. E. Tiryaki, et al., "MRI-powered Magnetic Miniature Capsule Robot with HIFU-controlled On-demand Drug Delivery," in *2023 IEEE International Conference on Robotics and Automation (ICRA)*, IEEE, 2023.

[14] A. C. Bakenecker, et al., "Navigation of a magnetic micro-robot through a cerebral aneurysm phantom with magnetic particle imaging," *Scientific Reports*, vol. 11, no. 14082, 2021.

[15] J. J. Huaroto, et al., "Two-photon microscopy for microrobotics: Visualization of microagents below fixed tissue," *Plos One*, vol. 18, no. 8, pp. e0289725, 2023.

[16] T. Wang, et al., "Adaptive wireless millirobotic locomotion into distal vasculature," *Nature Communications*, vol. 13, pp. 4465, 2022.

[17] Y. Kim, E. Genevriere, P. Harker, J. Choe, M. Balicki, R. W. Regenhardt, J. E. Vranic, A. A. Dmytriw, A. B. Patel, X. Zhao, "Telerobotic neurovascular interventions with magnetic manipulation," *Science Robotics*, vol. 7, no. 65, April 2022, eabg9907.

[18] D. Son, M. C. Ugurlu, and M. Sitti, "Permanent magnet array–driven navigation of wireless millirobots inside soft tissues," *Science Advances*, vol. 7, no. 43, 2021, eabi8932.

[19] L. Yang et al., "Functionalized Spiral-Rolling Millirobot for Upstream Swimming in Blood Vessel," *Advanced Science*, vol. 9, no. 16, 2022, 2200342.

[20] T. Wang et al., "Adaptive wireless millirobotic locomotion into distal vasculature," *Nature Communications*, vol. 13, no. 1, 2022, 4465.

[21] V. M. Kadiri et al., "Biocompatible magnetic micro-and nanodevices: fabrication of FePt nanopropellers and cell transfection," *Advanced Materials*, vol. 32, no. 25, 2020, 2001114.

[22] H. Ceylan et al., "3D-printed biodegradable microswimmer for theranostic cargo delivery and release," *ACS Nano*, vol. 13, no. 3, 2019, pp. 3353-3362.

[23] S. Jeon et al., "Magnetically actuated microrobots as a platform for stem cell transplantation," *Science Robotics*, vol. 4, no. 30, 2019, eaav4317.

[24] L. Yang et al., "Optimal Parameter Design and Microrobotic Navigation Control of Parallel-Mobile-Coil Systems," *IEEE Transactions on Automation Science and Engineering*, 2022.

[25] K. Bente et al., "Biohybrid and bioinspired magnetic microswimmers," *Small*, vol. 14, no. 29, 2018, 1704374.

[26] V. Magdanz et al., "IRONSperm: Sperm-templated soft magnetic microrobots," *Science Advances*, vol. 6, no. 28, 2020, eaba5855.

[27] D. Uğurlu, "Enhancing Untethered Robot Localization: A Fusion Approach Integrating Magnetic Coupling Localization and Ultrasound Imaging," November 2023, http://essay.utwente.nl/97633/.